# SCIENTIFIC REPORTS

natureresearch

OPEN

# Encoding kirigami bi-materials to morph on target in response to temperature

Lu Liu, Chuan Qiao, Haichao An & Damiano Pasini*

**Shape morphing in response to an environmental stimulus, such as temperature, light, and chemical cues, is currently pursued in synthetic analogs for manifold applications in engineering, architecture, and beyond. Existing strategies mostly resort to active, namely smart or field responsive, materials, which undergo a change of their physical properties when subjected to an external stimulus. Their ability for shape morphing is intrinsic to the atomic/molecular structure as well as the mechanochemical interactions of their constituents. Programming shape changes with active materials require manipulation of their composition through chemical synthesis. Here, we demonstrate that a pair of off-the-shelf passive solids, such as wood and silicone rubber, can be topologically arranged in a kirigami bi-material to shape-morph on target in response to a temperature stimulus. A coherent framework is introduced to enable the optimal orchestration of bi-material units that can engage temperature to collectively deploy into a geometrically rich set of periodic and aperiodic shapes that can shape-match a predefined target. The results highlight reversible morphing by mechanics and geometry, thus contributing to relax the dependence of current strategies on material chemistry and fabrication.**

Natural systems often exhibit an effortless propensity to shape morph in response to light, humidity and other environmental stimuli. Conifer cones, for instance, respond to the moisture content of wet or dry environment through the closure or opening of their overlapping scales, thus displaying a capacity for hygroscopic actuation[1]. Heliotropism of sunflowers is another elegant example of response to sunlight, where solar tracking movements enhance the photosynthesis process and increase growth rates[2]. The array of strategies biological systems offer are currently pursued in synthetic analogs through alternative pathways of broad technological diversity[3–9]. Controlled formation of shape morphing has a number of distinct hallmarks, the most notable being spatial reconfigurability delivered post-fabrication, generation of prescribed motions, morphing induced functionalities (such as actuation, amplified extensibility, and folding), and time-dependent control[10–12]. These along with other benefits have so far contributed to brand shape morphing as a topical theme of research with widespread promise of application across the spectrum of technology, such as autonomous robotics[13,14], smart textiles[15], shape-shifting metamaterials[12], minimally invasive devices[16], drug delivery[17,18], and tissue engineering[16,19].

Shape morphing in artificial materials has been demonstrated with a range of external stimuli and field-responsive materials. Swelling, light, temperature, and other cues, are typical triggers in smart solids, i.e. active materials that undergo a change of their physical properties as a result of phase transformations, conformation shifts of their molecular structure and mechanochemical interactions of their constituents. Active materials appear either individually, e.g. shape memory alloys (SMAs)[20], or in composite formations, e.g. hydrogel composites[4,21], ferromagnetic materials with localized inclusions of electrically conductive microparticles[22–24], hybrids with gradation of particle concentrations in given directions[25], and patterning of anisotropic materials[26–30] among others. They require a priori synthesis of their composition and molecular architecture. For example, in SMAs shape changes are obtained by programming the transition temperature, and are the net result of an orderly shift (twinning) of a large group of atoms in their crystal lattice, from the austenite to the martensite phase[31]. Shape memory polymers are another example of smart materials. They consist of a polymer network comprising two segregated phases with either covalent cross-link bonds or physical interactions. The switch between them occurs at a temperature programmed through the synthesis process of their polymer network[32]. Hydrogels are also known for their phase-transition properties responsive to a temperature stimulus. Their polymer network consists of covalently cross-linked polymer chains that can aggregate with water to form an elastomeric hydrogel.

Department of Mechanical Engineering, McGill University, Macdonald Engineering Building, Room 372, 817 Sherbrooke Street West Montreal, Quebec, H3A 0C3, Canada. *email: damiano.pasini@mcgill.ca

1

Here volumetric shrinking, which is exploited for shape shifting, is caused by specific temperature-induced interactions between hydrophilic/hydrophobic segments of the polymer chains and the water molecules[33]. Programming shape shifting with active materials, therefore, involves a tight intertwine between the chemical recipes and the fabrication process used to dispense them. Their typical realizations mainly extend to materials that can be polymerized[5,34], cross-linked[35–38], and formulated as customized ink of composites[9,39]. For most of them, morphing is irreversible with some exceptions, such as hydrogel composites, which do exhibit reversibility but slow actuation response[40]. In addition, most active materials, especially shape memory polymers, respond with an on-off switch of deformation at a transition temperature set through chemical recipes, and their performance typically degrades steadily under thermomechanical cycles. This characteristic may pose limits of application in regimes operating with temperature-fluctuating stress, where actuation is sought through successive heating/cooling cycles.

In parallel, complementary routes that use passive solids, either standalone or in combination thereof, exist. Those that resort to a single passive solid have been explored to achieve reconfigurability, deployment[41,42], folding of planar sheets via origami[43–45], kirigami[46,47], and combinations thereof[48], as well as in 3D tessellations of prismatic unit cells[49,50]. Most of them are periodic with a paucity featuring spatial heterogeneity in flat thin sheets[45] and textured metamaterials[51], but they all cannot respond to an external stimulus since an external force is needed to induce morphing.

On the other hand, two or more passive materials have been combined in layouts to attain desired thermal expansion performance[52]. Concepts with distinct coefficient of thermal expansion (CTE) arranged in certain configurations, such as bilayer systems[53,54], and structural layouts in 2D and 3D, such as compliant[55–57] as well as stiff topologies[58–62], can generate responses for given magnitude and directionality of thermal expansion. These realizations, however, consist of individual repeated units with tailored CTE, typically yielding zero or negative values, and cannot generate large global deformation of an ensemble of units that can shape-morph on target. These are characteristics often sought in soft robotics, for example when locomotion is prescribed to trace a specific path, and deployable structures, when the deployed state should match non-classical, e.g. freeform, surfaces.

In this work, we demonstrate large temperature-driven morphing from a pair of passive solids, aperiodically arranged in a kirigami bi-material through a basic fabrication process. Temperature-responsive metaunits and aggregation rules are presented to generate a variety of single-piece metaensembles that can conform to a large number of planar shapes. Soft modes of deformation are individually encoded into the morphology of each unit, and a coherent framework is presented to deterministically predict and optimally program the global shape transformaton of the entire kirigami bi-material. Highlighting the notion of functionality induced by the interplay between geometry and mechanics, this work brings to light reversible shape-shifting from passive solids in response to temperature and contributes to relax the dependence on fabrication parameters and material composition. It also provides freedom to program the characteristics of the shape response, including both abrupt and smooth transitions that can gradually evolve even within a large range of temperature, as opposed to the on-off actuation of active solids that takes place at a given temperature value.

## Methodology

**General framework.** At the roots of our scheme (Fig. 1), there are three basic notions with two routes that enact shape-matching on demand and in a reversible fashion: (i) the definition of a *functional metaunit*, a building block (BB) comprising two passive solids, capable of expressing distinct modes of deformation upon a change in temperature (Fig. 1a, top); (ii) the assignment of a *deformation-property profile* to the BB, which systematically correlates the achievable amplitude of deformation a BB can deliver to its material and geometric attributes (Fig. 1a, bottom); (iii) the provision of *aggregation rules* to adjacent BBs, which enable monolithic tessellations of broad geometric diversity (Fig. 1b). With these notions, access to morphing is through two ports of entry. The first promotes and predicts morphing from a predefined metamaterial architecture (Fig. 1c). The second generates a morphed state that can match a prescribed target (Fig. 1d).

We first start with a descriptive outlook of the salient points underpinning our framework, demonstrating hereafter the details. The metaunit (Fig. 1a) consists of a rigid frame with low coefficient of thermal expansion (CTE) (grey) that encloses a soft core with high CTE (blue), each responding to temperature at a different rate. The former confines the propensity of the latter to volumetrically expand under temperature due to their CTE mismatch. At their vertical edges, the two are fully bonded, whereas a slit appears along the entire length of their horizontal interfaces. The core is partially riven along its horizontal axis of symmetry with a ligament, $d$, connecting the upper and lower parts. By harnessing the position of the core ligament, we can seal onto BB two distinct *deformation modes*. Enforced reflection symmetry across the vertical midplane (dash-line) imprints a unidirectional floppy mode (U), where U-BB resembles an accordion that axially expands by $\Delta h$. A loss of symmetry, on the other hand, combined with end core closure instills a rotational (R) mode, where R-BB responds as a clothespin that can open by an angle $\theta$.

While the mode of deformation is mainly conferred by topology (U versus R), temperature, as well as materials and geometry of each unit, govern the magnitude of the response. To capture this dependence, we gauge the attainable range of elastic deformation the metaunit can attain at a given temperature upon manipulation of its material and geometric attributes. This defines the *property-deformation profile*, which we cast here in two sets. The first maps the role of materials, $\Delta\alpha = \alpha_c - \alpha_f$ versus $E_f/E_c$ ($f$: frame, $c$: core), and the second that of geometry, $l/h$ versus $d/l$, the groups of parameters that most influence BB response. As an illustrative example, Fig. 1a (bottom) shows both the material and geometry spaces at $T = 120\,°C$ obtained for a representative U-BB with given materials ($\Delta\alpha = 210 \times 10^{-6}/K$; $E_f/E_c = 3200$, point A coordinates) and geometry ($l/h = 9$; $d/l = 0.05$, point B coordinates). The former correlates the amount of uniaxial deformation to a change in material properties, while the latter that to a change in its inner architecture. While specific to this example, the *property-deformation profile* provides a systematic route to assess the deformation a BB can render at a given temperature through control of
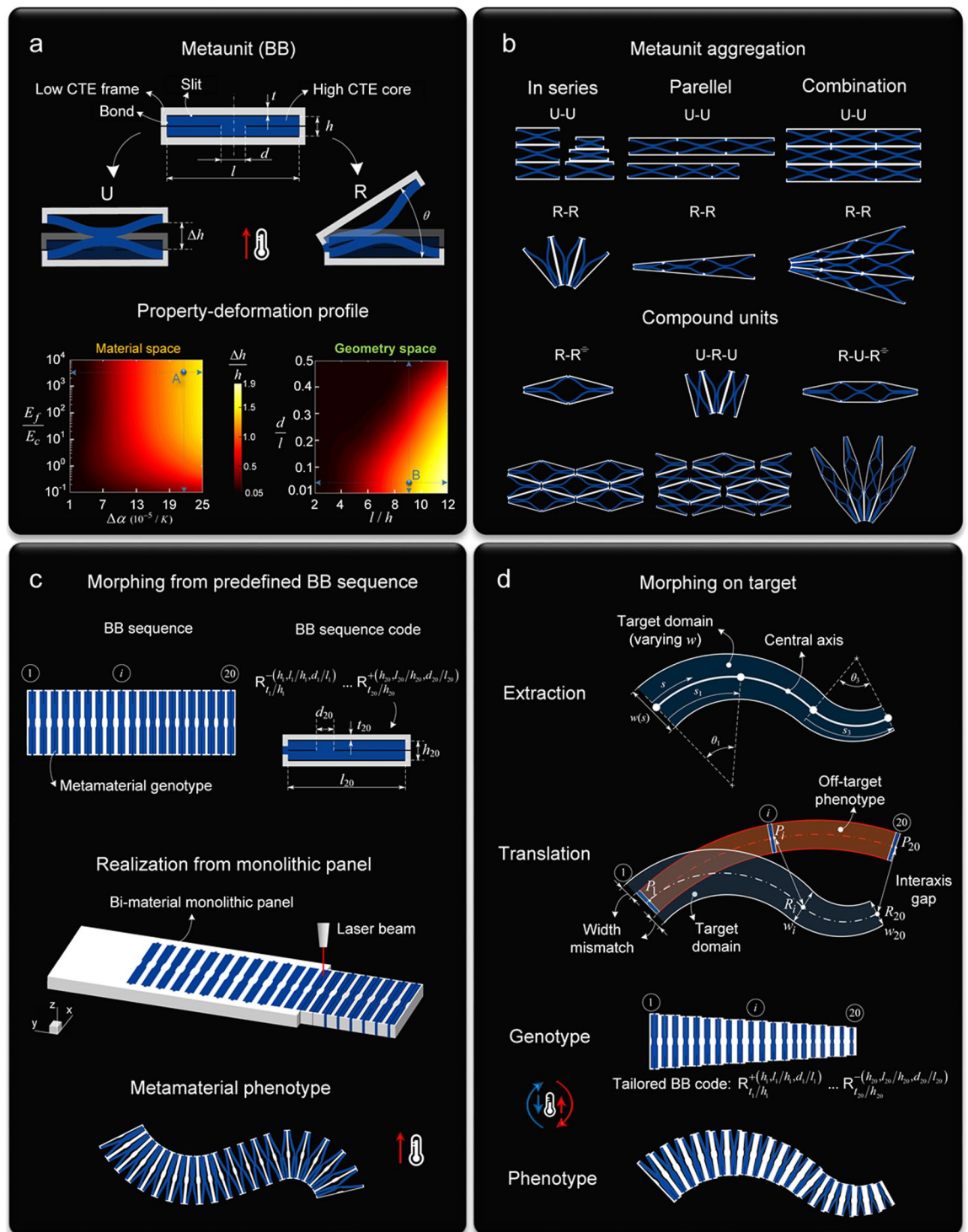
**Figure 1.** Framework overview for temperature-driven morphing. (**a**) **top**, *Building block (BB) with high and low CTE constituents*. Enforced mid-plane symmetry seals a unidirectional (U) soft mode ($\Delta h/h$), whereas broken symmetry combined with core-end closure releases a rotational (R) mode ($\theta$). (**a**) **bottom**, *Assignment of deformation-property profile*. Attainable range of elastic deformation for BB, measured in the material ($\Delta\alpha = \alpha_c - \alpha_f$ versus $E_f/E_c$ (f: frame, c: core)) and geometric space ($l/h$ versus $d/l$), at temperature 120 °C for $l/h = 9$ and $d/l = 0.05$ (point B), and $E_f/E_c = 3200$, $\alpha_c - \alpha_f = 210 \times 10^{-6}$/K (point A). (**b**), *Metaunit aggregation*. Pathways for BB periodic and aperiodic aggregates monolithically connected in parallel, series, and combination thereof, from repeated (top) and compound units (bottom) (R$^\equiv$ indicates the reflection of R). (**c**), *Forward problem*. Morphing prediction from predefined sequence of $m$ BBs in series (genotype) described through the string $B_{t/h}^{\pm(h,\ l/h, d/l)}$, where B stands for U or R, the superscript collects the geometric parameters of the high CTE material, and the subscript those of the low CTE material, $+/-$ indicates direction of rotation for R-BB ($+$clockwise). Below, laser cut of a single piece bi-material panel and morphed configuration (phenotype).

(**d**), *Inverse problem*. Extraction of shape descriptors from target domain, assumed here as arc spline axis, made of G[1] continuous arcs and straight-line segments, and symmetric boundaries. Translation of shape descriptors into a tailored BB sequence code that enables the central axis and varying width of an off-target phenotype (red) to conform to those of the target domain (blue). Qualitative sketches out of scale at given temperature.

its material and geometric attributes, hence being the key to predict and program deformation at the rank of the metaunit.

At the next level, there are BB aggregates (Fig. 1b), which we aim here to generate from a single piece, a monolithic dual material panel, as opposed to an assembly of individual parts connected together, as described in the following section. The intrinsic characteristics of BB are conducive to the generation of an array of BB aggregates with rich geometric diversity (See Supplementary Movie 1 for illustrative demonstrations). Figure 1b shows a collection of options, among others. Here BBs are shown to form spatially invariant periodic and aperiodic tessellations not only from primitive units, e.g. R-R or U-U (top), but also from hybrid cells, e.g. U-R-U (bottom), that provide access to a diverse set of morphologies. Interaction between adjacent BBs takes place through monolithic connections that impose the way BBs act collectively, e.g. parallel, series and combination thereof, via either the low CTE material (grey), or at a collection of high CTE locations (blue).

With the notions above, we now tackle the morphing problem of an ensemble of BBs along two pathways facing the questions: how to predict, and how to program global transformations. The forward route is depicted in Fig. 1c with a basic example. Shown here is a sequence of 20 BBs of a given pair of materials monolithically connected in series; the goal is to predict their deployment upon a cycle change of temperature. The undeformed state, the metamaterial *genotype*, realized through a purposely conceived simple process, as explained in the following section, is defined by a string of information, the *BB sequence code*. This carries the order and functional instructions that enable cooperative, frustration-free, shape changes with closely matched deformation at the BB interfaces; it fully connotes the collective deformed state of the metamaterial, physically expressed by the *phenotype*. The complimentary route is depicted in Fig. 1d with another illustrative example. The goal here is to program the genotype with a BB sequence code that elicits reconfiguration into a phenotype matching a given target. Two main steps are involved: *extraction* and *translation*. The former retrieves the shape descriptors of the target domain, described here with a central axis and two symmetric boundaries of varying width. The latter acts on the target descriptors to decode a tailored BB sequence for a phenotype that shape-transforms into the target. As detailed later, the underlying rationale is to make the morphed layout of an off-target phenotype, which is assigned with an arbitrary sequence of BBs, conform to the target domain; and we do so by minimizing the gaps between their central axes and their unmatched widths. The result is a tailored BB code that enacts morphing on target upon heating and directs a reversal upon cooling. Details on this and other parts underpinning the framework follow.

### Fabrication of kirigami bi-materials.
While typical kirigami materials are cut from a single solid, here we present a fabrication process for bi-material kirigami that is purposely conceived to be as simple as possible while making use of off-the-shelf passive solids. The aim is to emphasize the notion of shape-matching in response to other than mechanical input by mechanics and geometry, and thus to relax the dependence from manufacturing technology and material chemistry, which are key to programming the response of active materials.

Figure 2 shows the steps describing the realization of an illustrative kirigami specimen comprising 3 by 5 units made of a silicone elastomer (R-2374A silicone rubber compound, Silpak Inc., USA) and hardwood (Black walnut panel, Midwest Products Co., USA), the former representing the high CTE solid and the latter the low CTE. A periodic array of 15 voids aggregated in a hybrid arrangement (3 columns of units in parallel, each with 5 units connected in series), is laser cut (CM1290 laser cutter, SignCut Inc., CA) from a 1/8-inch-thick hardwood panel to create a void-patterned mould subsequently bonded (Instant Adhesive CA4, 3 M Inc., USA) onto a 1/8-inch-thick acrylic substrate. Each void is shaped to host the characteristic geometry of the unit core featuring a semielliptical groove on both its upper and lower edges (Fig. 2a). The silicone elastomer in liquid form is mixed with a platinum-based catalyst to create a cross-linking reaction and then injected to entirely fill the voids of the wooden array. The curing process performed at room temperature for 24 hours turns the silicone elastomer of the building block (BB) core from a liquid into solid (Fig. 2b). During the process, the silicone elastomer bonds to the wooden frame, thus offering the adequate strength for the formation of a monolithic kirigami bi-material. Finally, a laser cutter perforates a set of slits into the kirigami bi-material (Fig. 2c), a step that precedes the sample detachment from the substrate. In the physical specimens, the strait cuts of the BB geometry shown in Fig. 1 are amended with semielliptical slits to facilitate the onset of deformation during experiments. Figure 2d,e show respectively the bi-material kirigami specimen in its undeformed and deformed shape in response to a change of temperature. While this specimen becomes periodically porous with thermal response governed by a single unit, the fabrication process here presented enables the straightforward production of aperiodic kirigami bi-materials with global morphing controlled by the collective response of all the units.

## Results and Discussion
### Metaunit response.
In this section, we use solid mechanics theory to elucidate the deformation response of the kirigami bi-material unit subject to a uniform thermal field for both the unidirectional and rotational floppy modes shown in Fig. 1a. R-BB differs from U-BB for the end closure of the core and a mere symmetry breaking that shifts the position of the connection $d$ of the core at an offset $e$ from the left end of R-BB. While the underlying mechanism of thermal deformation of both R- and U-BB is caused by the CTE mismatch of the constituents, their topological difference is responsible for each floppy mode. Here we first focus on R-BB in Fig. 3a(i), from
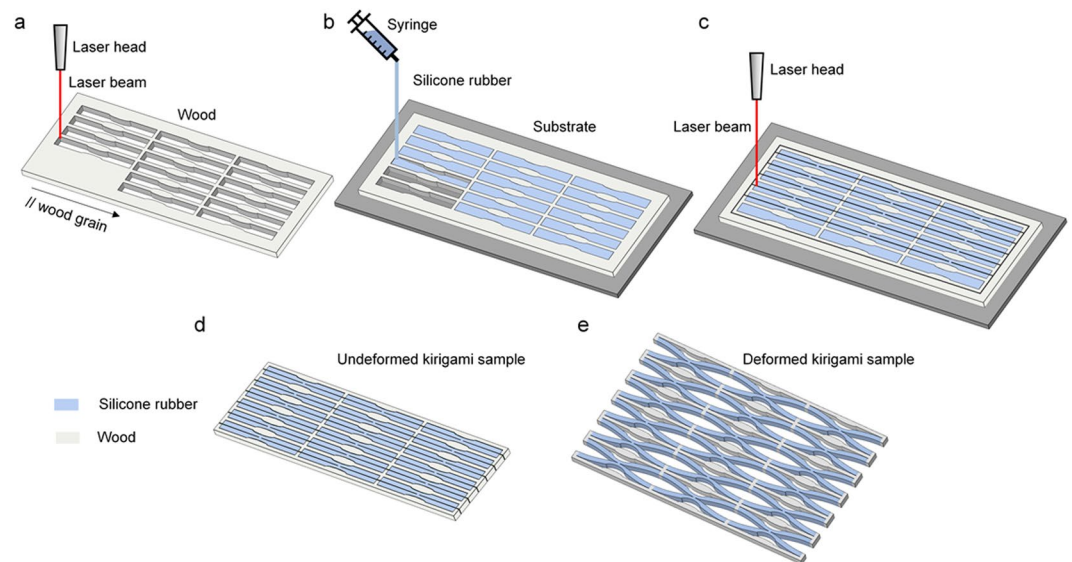
**Figure 2.** Fabrication process at room temperature. (**a**) Laser cut of a wooden panel forming a mould with an array of voids, each shaped with the geometry of the BB core. (**b**) Casting of silicone rubber filler into the array of voids. (**c**) Laser cut of the kirigami bi-material along the slits of each BB. (**d**) Sample removal from the substrate for the release of a monolithic kirigami bi-material in its undeformed state. (**e**) Deformed kirigami bi-material sample in response to temperature change.

which the U-BB response can be derived (see Supplementary S3-a). Due to the symmetry of deformation in R-BB under temperature, we examine the lower half of R-BB, and make the following assumptions: the low CTE frame is rigid with negligible thermal expansion, the length $d$ of the connection between the upper and lower portions of the high CTE core is significantly smaller than the BB length ($d \ll l$), and the semielliptical portion of the groove is simplified with two straight inclined beams attached to the horizontal parts (Fig. 3a(i) bottom). Due to the negligible thermal expansion of the low CTE solid, an effective boundary condition is enforced to replace the frame action onto the core which is clamped on both its ends. The reaction from the upper part of R-BB is equivalent to a bending moment ($M_S$) applied at A, i.e. the core connection. The clamped boundary at the left end is released by applying two effective forces ($F_A$, $F_V$) and a moment ($M_R$), all dependent on temperature. The analysis of the building block subjected to uniform temperature is now reduced to the solution of a statically indeterminate problem of a beam-column, which can be solved via Timoshenko's theory of elastic stability (see Supplementary S3-a). For the elastic properties and CTE (point A in Fig. 1a) of the constituent solids used in the analysis, we used experimentally obtained data (see Supplementary S1 for description of thermal and mechanical testing) with statistical values showing invariance to temperature within the investigated range (see Supplementary S2 for characterization of thermal and mechanical properties).

The results of the theoretical analysis shed light onto the relations of the internal forces (Fig. 3a(ii,iii) and as well as the elastic deflection (Fig. 3b(i)) of R-BB with temperature. The magnitude of $F_V$ and $M_S$ are respectively two and one order lower than $F_A$ and $M_R$ indicating that the transverse force and bending moment at the connection contribute only slightly to the R-BB deformation. Two sequential regimes of deformation can be observed, each controlled by temperature. For low values of temperature, the axial force $F_A$ dominates the bending moment $M_R$ and increases linearly with temperature; here, axial compression governs the R-BB response. With a further increase of temperature, the deformation mode switches through a transition zone above which the axial force flattens at a plateau. Here, BB responds with internal bending with a deformation that is rapid and sensitive to the temperature change at higher values.

The nonlinear response triggered by the core instability can be used to amplify deformation and release it in either a short or long temperature range. Geometric tuning enables temperature to act onto BB not simply as driver of deformation but also as regulator for type (stretch versus bend), magnitude (modest versus large), and gradient of deformation (shallow versus steep). BB can be designed to offer a distinct evolution of deformation that is regulated by temperature with two modes occurring sequentially through a transition zone (around $T = 60\,°C$), after which the deformation gradient and the span along which the deformation occurs can be programmed through geometry. In particular, the position of the transition zone can be programmed by manipulating the aspect ratio of the BB core, while the span of the transition zone by the size of the elliptical groove and other geometric parameters (see Supplementary S3-c). This provides a large design space to tune both the deformation gradient and the range of temperature upon which deformation continuously occurs. Deformation can thus be amplified by working near instability, hence generating abrupt changes in response in a short temperature range, or it can be calibrated to ensure a steady and gradual expansion rate over a sizeable temperature span. These characteristics are distinct from those offered by active materials, e.g. shape memory polymers, which through chemistry manipulation can typically shows an on-off switch of deformation at the glass transition temperature.
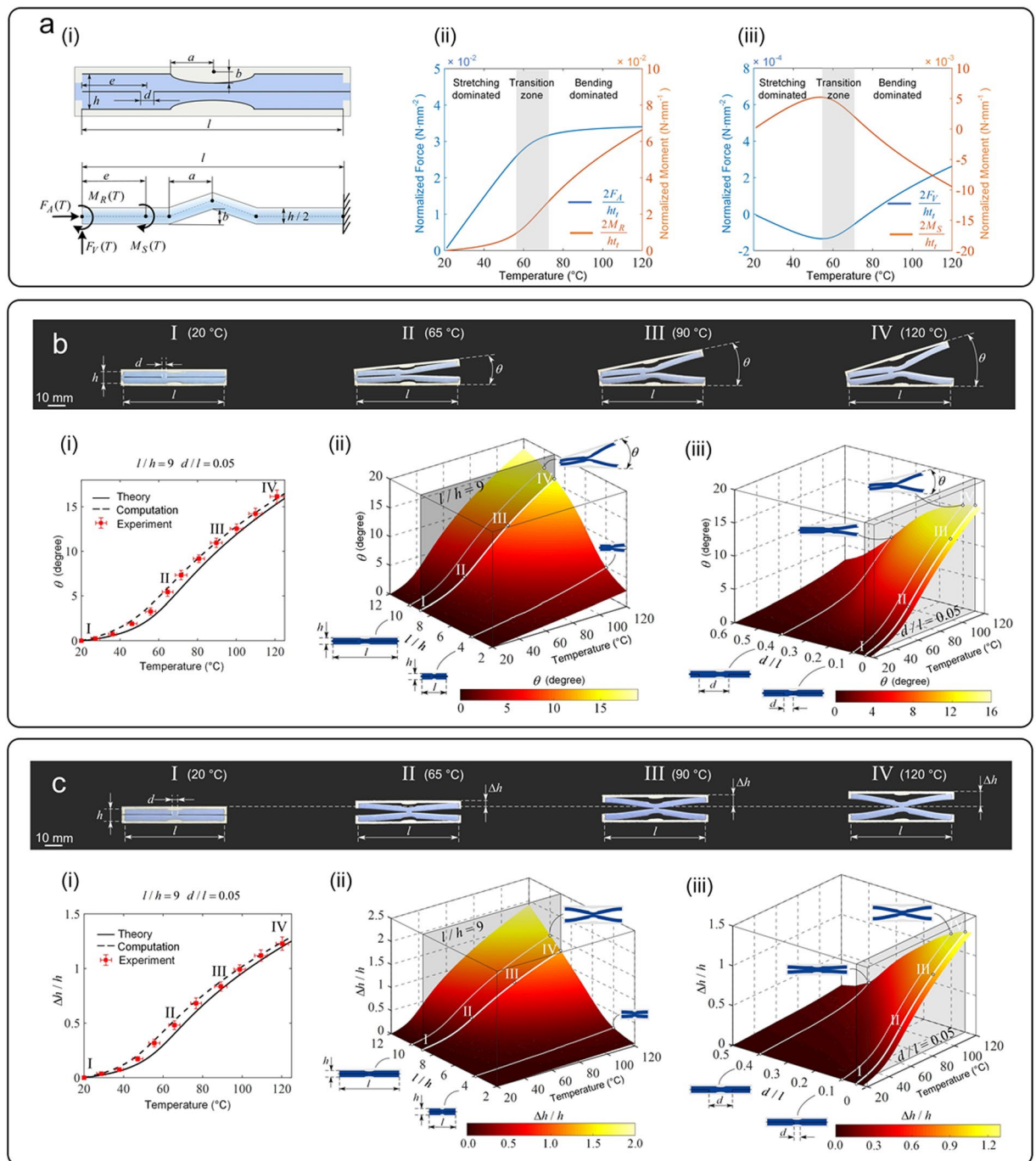
**Figure 3.** (**a**) Deformation mechanism of BB subject to a uniform thermal field. (i) Geometry of rotational building block in undeformed state with its reduced model, where the high CTE core is condensed to a statically determinate beam-column with reaction and internal force $F_A$, $F_V$ and moment $M_S$ $M_S$. (ii) Evolution of the normalized $FA$, $M_R$, and $F_V$, $M_S$ as a function of temperature solved by Timoshenko's elastic stability theory. Deformation assessment and evolution of R-BB (**b**) and U-BB (**c**) subject to increasing temperature from 20 to 120 °C. Four deformed states of a representative set of fabricated BBs ($h = 7$ mm, $d/l = 0.05$, $l/h = 9$) with experimental measures of deformation ($\theta$ and $\Delta h/h$) overlaid onto continuous curves obtained through (i) mechanics theory of simplified BB geometry and computation of BB geometry identical to the fabricated samples. (ii) and (iii): prediction maps for $\theta$ and $\Delta h/h$ depicting the role of the main geometric descriptors of BB, $l/h$ and $d/l$, as a function of temperature within defined ranges of $l/h$ and $d/l$ values. Horizontal and vertical bars indicate the standard deviation around the mean from a pool of measures taken for both temperature and deformation, the former measured at three distinct sites in the heating chamber, the latter obtained from three repeated measurements.

The experimental response validating the theoretical results are shown in Fig. 3b,c for both R-BB and U-BB. On the top four deformed states (I to IV) are shown each rendered at a given temperature. The corresponding experimental measures of deformation, $\theta$ and $\Delta h/h$, are illustrated in the plots below as a function of temperature. Superimposed are also the theoretical results and computational results, both in quantitative agreement. Additional sets of results obtained for units with other dimensions (see Supplementary S3-b) validate the theory with differences between the experimentally measured deformation and theoretical predictions in the high temperature regime below 15%, a value attributed to frictional dissipation accrued during testing as well as the adoption of a simplified structural analog for our theoretical model (see Supplementary S3-a).

Computational models provide further guidance in assessing the role of the geometric attributes that most and least influence BB response. Figure 3a(ii),(iii),b(ii),(iii) show the outcome of harnessing the prime attributes ($h/l$ and $d/l$) of U-BB and R-BB within defined ranges. The maps depict the deformation potential that evolves with temperature, thereby supplementing the maps (Fig. 1a and Supplementary Fig. S9) given for $T = 120\,°C$ (see Supplementary S3-c for the generation of the deformation-property profile). The longer the BB as well as the smaller the core ligament, the larger the response. Temperature and BB geometry tuning can thus generate a sizeable deformation for a given pair of materials. For example, at $T = 40\,°C$, a reduction of $d/l$ from 0.4 to 0.1 generates a 4.3x gain of $\Delta h/h$ for U-BB, and a 3.2x gain of $\theta$ for R-BB; these values boost to 4.8x and 1.9x at $T = 120\,°C$. Besides $h/l$ and $d/l$, other geometric parameters, such as the size of the BB groove and the offset of the flexural hinge, play a role in the BB response, but the tunability they can offer is quite narrow (see Supplementary S3-c for sensitivity to least influential parameters). Yet as described above, these parameters are effective in calibrating the type and rate of deformation with temperature.

BB integrity and time response are further descriptors of the structural and functional performance of the kirigami unit. The prospect of BB failure involves a balance between the CTE and strain energy of the two constituents, as well as the force of adhesion at their interfaces. Quantitative assessment of the distribution of the interfacial stress (see Supplementary S4 for assessment of bond strength) along with pull-out tests measuring the bonding strength shows a predominant compression state exerted by the BB core onto the enclosing frame with interfaces largely compressed at a magnitude dependent on $h/l$ and temperature. The analysis shows a sturdy bond at the interfaces with strength value preventing detachment during deformation.

For the temporal response to temperature, the BB deformation is caused by the CTE mismatch of the constituent solids, which do not undergo any atomic or molecular changes, as in the case of active materials. As soon as BB reaches the final temperature, the deformation induced by the internal forces is instantaneous and the mode, magnitude and rate of deformation can be designed through geometry without resorting to chemistry. For shape memory polymers and other active materials, on the other hand, there is a time span involved for the temperature to create configurational changes in the polymers crosslinking. For our kirigami-bimaterials, the time span that we measured to morph does not depend on the properties of the constituent materials, rather mainly on the heating strategy and the experimental setup: the medium surrounding the sample, and the thermal conductivity of the BB surfaces through which the heat transfer takes place. In our experiments, specimens were tested in two heated media, air and oil. Both results showed a deformation evolving over a relatively short period with values (about 5 mins with fan-propelled air and 2 mins in oil bath) in quantitative agreement with those from transient heat transfer analysis (see Supplementary S5).

**Morphing prediction of kirigami bimaterial from given BBs sequence.** Figure 1c shows a schematic of the forward problem for a monolithic ensemble of BBs stacked in series, each with a predefined set of geometric attributes casted in the BB sequence code. A scheme that uses affine transformations correlates the local deformation of each BB to the global deflection of the phenotype axis and predicts the collective behaviour of BBs at a given temperature (see Supplementary S6 for morphing response from preassigned BB sequence). Its implementation is shown in Fig. 4 on a set of representative genotypes with morphing traits experimentally validated through fabricated samples ($h = 4.5\,mm$, $l/h = 9$). On the top of Fig. 4a (left) is the simplest case, where a periodic sequence of identical U-BBs is assigned to the genotype, whereas on the bottom there is a stack of BBs with monotonically decreasing $d/l$. Similarly, Fig. 4b (left) shows two sequences of R-BB, one sharing prescribed geometric attributes (top), and the other featuring two sets of five R-BBs with opposite direction of rotation (bottom). In Fig. 4c (left), the genotype is dispensed with a BB sequence code defined by a logarithmic spiral. For all three cases, the central (undeflected) axis (red) intersecting the interface mid-points, $P_i$, between adjacent units (red dot) is overlaid on the genotype, and the predicted deflected axis of the phenotype lies on top of the morphed configuration obtained via computations (shaded colour). The counterpart experimental versions are shown on the right of Fig. 4a–c. Here the testing occurred in an oil bath to reduce frictional losses. The relative discrepancy between predictions and experimental measures is below 7% (3% and 2.8% for samples in Fig. 4a, and 5% and 7% for those in Fig. 4b). Overall, the values depicting dimensional differences between genotype and phenotype demonstrate sizable morphing predicted with high-level accuracy. In addition, the experimental results shown in the Supplementary Movies S2–S5 demonstrate fully reversible morphing under the conditions here investigated, i.e. temperature cycle between $T_{room}$ and $120\,°C$.

**Morphing on target via encoded BBs sequence.** The response to temperature of our morphable materials can be programmed such that adjacent units can act collectively to reconfigure into a desired form. Here the target to match is a domain (Fig. 1d) with a central axis, an arc spline consisting of $G^1$ continuous arcs and straight segments, and two boundaries that are symmetric and continuous with varying width. We match this target by first enforcing equality constraints to guarantee frustration-free motions between adjacent units and inequality constraints that restrict BB deformation within feasible ranges. We then frame these conditions into a constrained optimization problem (see Supplementary S7 for the morphing on target scheme) that mathematically restructures the string of information contained in the BB sequence code of an unprogrammed (off-target) phenotype,
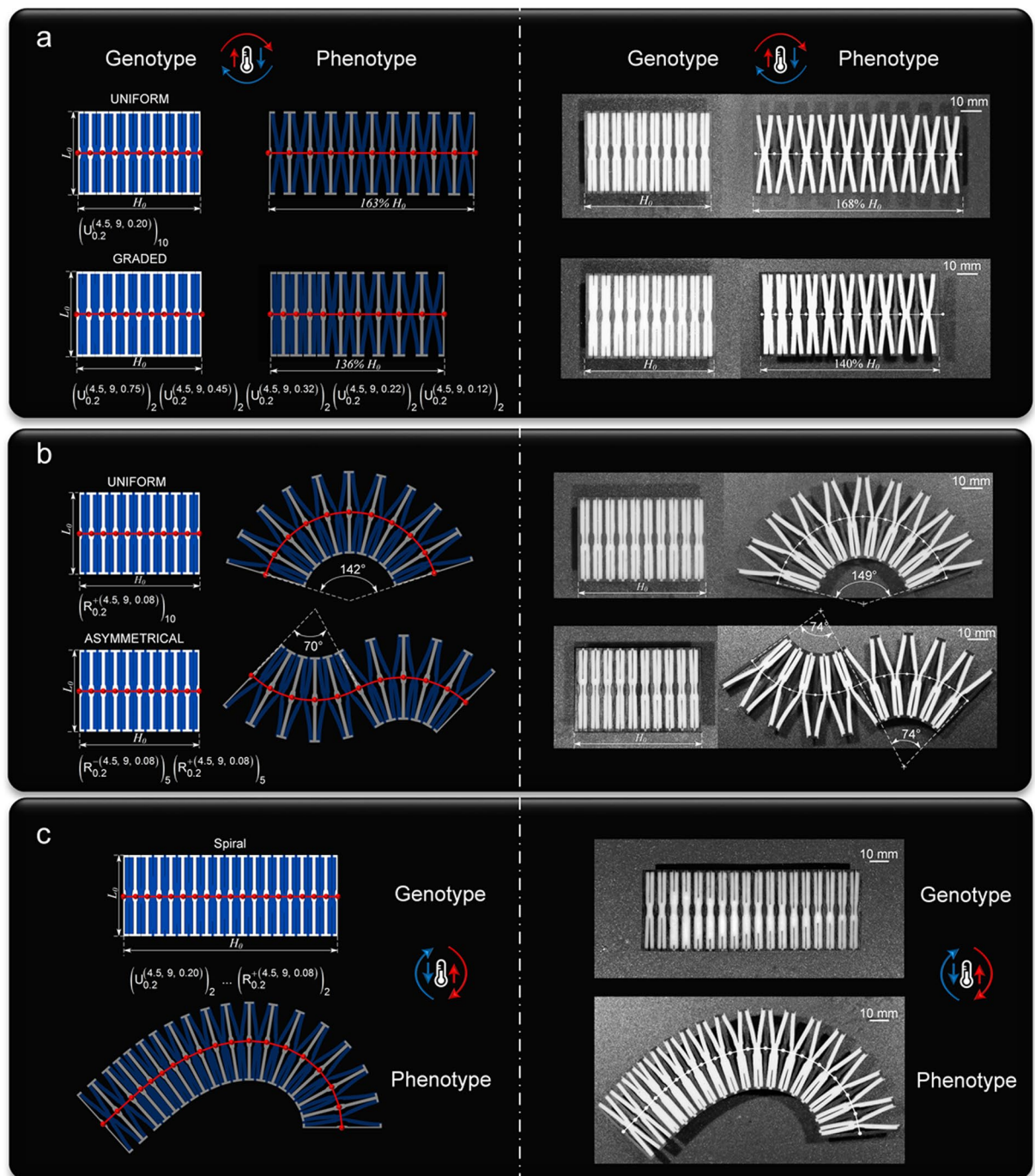
**Figure 4.** Prediction (left) and experimental (right) validation of a demonstrative array of morphing responses from a series of BBs with predefined sequence, geometry ($h = 4.5$ mm, $l/h = 9$, $t/h = 0.2$) and materials (wood and silicone rubber). Tested configurations at $T = 120\,°C$ morphed from their genotype state at room temperature. (**a**) Extensional morphing achieved from a stack of 10 U-BBs: uniform (above) and linear gradation (below) of geometric attributes defined by their BB sequence code. (**b**) Rotational morphing attained from 10 R-BBs in series: uniform distribution of geometric attributes with identical (above) and opposite (below) rotation. (**c**) Spiral morphing predicted and validated from a hybrid sequence of 2 U-BBs and 16 R-BBs. The contents of only two BBs is shown as representatives of the whole BB sequence code. $B_{t/h}^{\pm(h,l/h,d/l)}$ indicates BB geometric descriptors (B = U for U-BB, B = R for R-BB). Superscripts for high CTE material (+: clockwise rotation for R-BB), subscripts for low CTE material. $B_{t_1/h_1}^{\pm(h_1,\,l_1/h_1,\,d_1/l_1)}, \ldots\, B_{t_i/h_i}^{\pm(h_i,\,l_i/h_i,\,d_i/l_i)}$ connotes a sequence of $i$ BBs, and condenses to $(B_{t/h}^{\pm(h,l/h,d/l)})_m$ for a stack of $m$ repeating units.
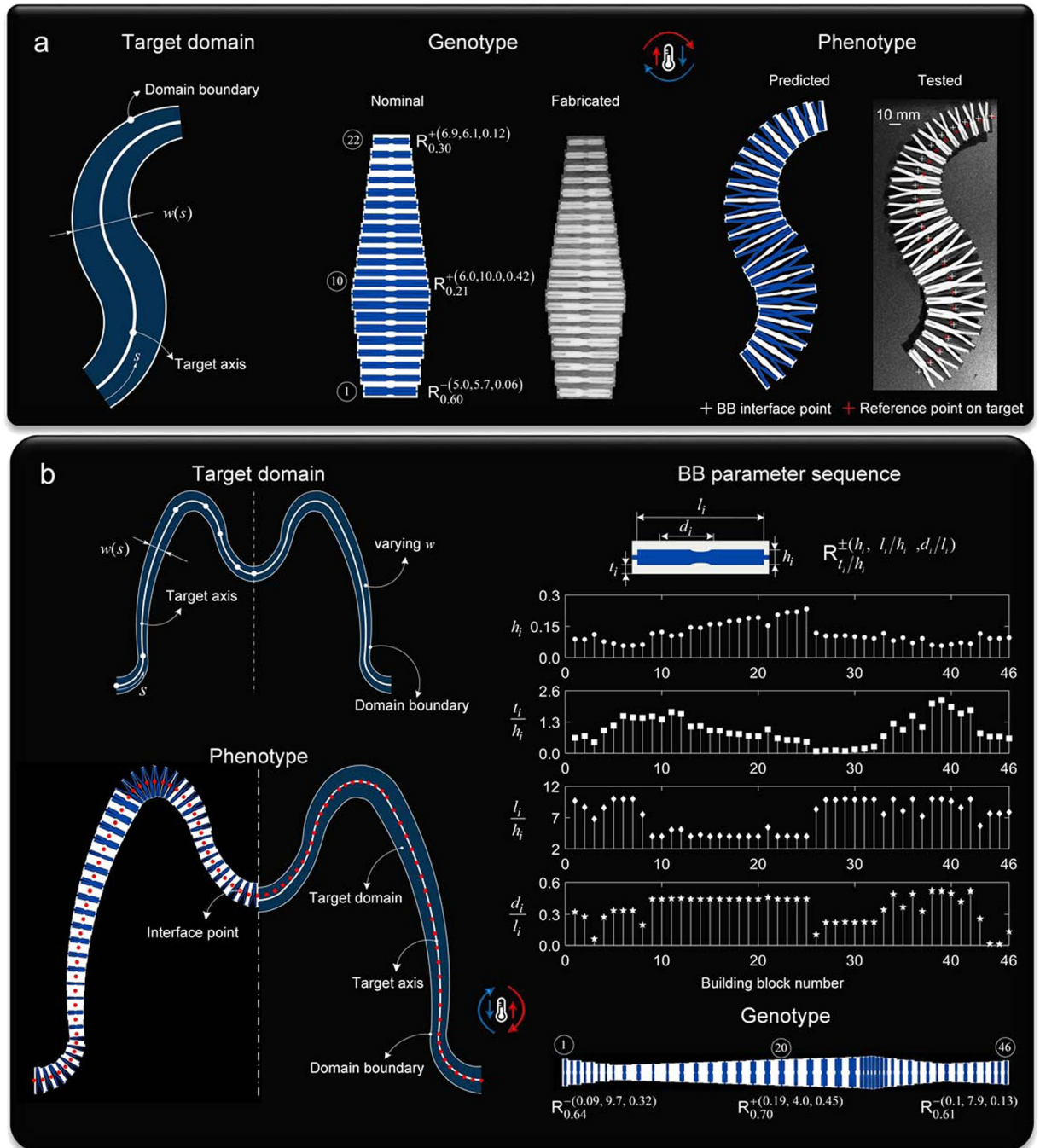
**Figure 5.** Demonstrations of morphing on target through tailored sequence of metaunits made of hardwood and silicone rubber. (**a**) Target domain of varying width (left) with nominal and fabricated realization of metamaterial genotype comprising 22 BBs (middle) along with predicted and tested configurations of morphed phenotype at $T = 120\,°C$ (right). (**b**) Domain target of the letter "M" with functions of the axis and varying width to match. 46 units make up the genotype (half is shown) transforming into a phenotype that shape-matches the target with $R^2 = 0.997$. The BB parameter sequence shows the stem plot of the optimized values of 4 dimensionless sets of design variables optimized to align the phenotype to the target domain. Below is the genotype (only of shown in the undeformed state) with the BB sequence code given only for representative units, i.e. $BB_1$, $BB_{20}$ and $BB_{46}$.

which is far from the target because it is randomly assigned with an arbitrary sequence of BBs. Because the central axis and boundaries of the off-target phenotype are incompatible with those of the target domain (Fig. 1d), we minimize the sum of the squares of the distance between their central axes and the mismatched widths of their boundaries.
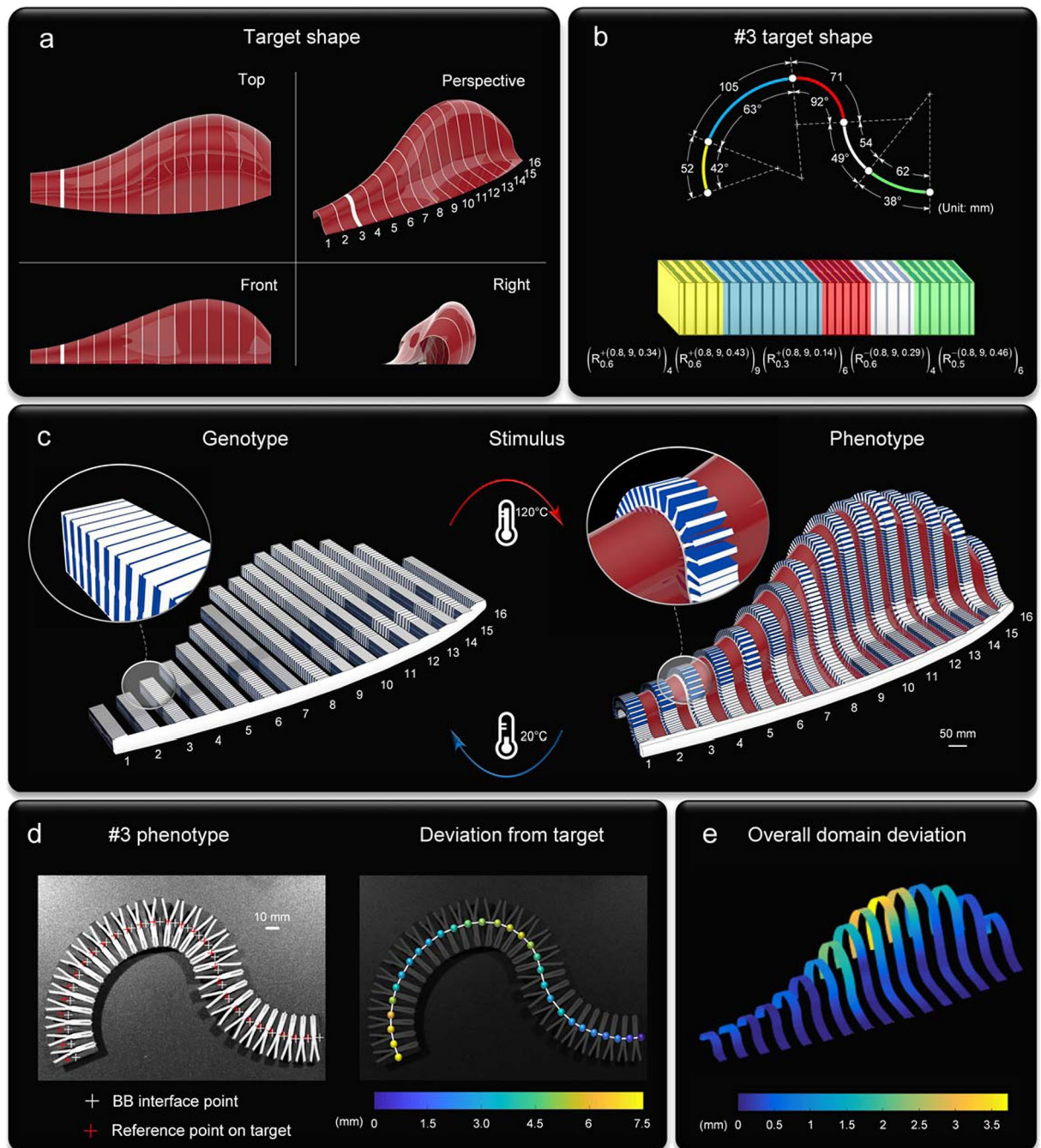
**Figure 6.** Illustrative example of conformal morphing to a spatial freeform surface. (**a**) Top, front, right and perspective of the target domain: a NURB surface generated from the control points of 16 arc splines used as primitives. (**b**) Extraction (above) of shape descriptors (arc length and opening angle) of #3 primitive, and translation (below) into a conforming genotype defined by its BB sequence code. (**c**) Ensemble of 16 genotypes anchored to a low CTE base (left) and morphed into its phenotype (right); reversible morphing for increasing temperature from 20 °C to 120 °C. (**d**) Morphed configuration ($T = 120$ °C) of #3 phenotype made out of hard wood and silicone rubber: superimposed crosses for points of BB interfaces and target axis (left), and their absolute distance (right). (**e**) Deviation between predicted phenotypes and arc spline targets.

With this scheme, conformal morphing can be realized from several pairs of passive materials. Two illustrative examples (Fig. 5) are demonstrated with two representative materials, wood and silicone rubber. The first (Fig. 5a) shows a simple shape target domain with varying width and an arc spline of two primitives that are G[1] continuous at their blending points. Here, the BB sequence code of an arbitrary genotype with 22 randomly assigned BBs is decoded to match the shape descriptors of the target. Our morphing scheme restructures the BB sequence code to yield a shape-matching phenotype that is experimentally validated through fabricated samples. A good agreement is observed between the predicted and experimental results. In the second example, the outline of an "M"

is chosen as the central axis of the target domain with varying width specified through a set of four continuous functions of varying size along the target axis. With the goal of conforming to the central axis and width of the target, our scheme yields an aperiodic tailored sequence of 46 BBs, which are aperiodic in both their internal and external sizing. This is shown by a stem plot reporting the optimized values of the design variables along with the relevant ratios of the metamaterial genotype at the initial temperature (Fig. 5b and Supplementary S8 and Movie 6). As per the testing results of the "M" shape in Fig. 5b, we note that the limited size of our heating tester prevented us from performing a full-size experiment of the 'M' shape sample. Yet, the tested sample in Fig. 5a is representative of the "M" shape because its geometry replicates the varying width domain with a reduced extent, i.e. only 22 building blocks, a requirement that could meet the dimensions of our heating chamber.

## Outlook and Conclusion

Underpinned by three distinctive notions (Fig. 1), our framework can deterministically predict and precisely impart morphing into a single-piece metamaterial made of passive solids upon a change in temperature. The shape matching of the phenotype to a target domain can be accurately controlled in space through a decoded BB sequence. The constitutive solids are passive, yet their topological arrangement into our metaunit can form aperiodic aggregates that can yield reconfigurations of broad geometric diversity. Figure 6 shows an outlook for our platform applied to drape a three-dimensional surface. Here the target is a spatial freeform surface described by a sweep of 16 arc splines (Fig. 6a), and the goal is to match the shape of the full array of arc splines. Figure 6b shows a representative with its shape descriptors first extracted, and then translated into the BB sequence code. The implementation to all 16 arc splines is depicted in Fig. 6c, where a low CTE cordon monolithically ties them all at the front base, the anterior boundary of the target. Overlaid onto the phenotype ensemble is the target surface (red) with an insert showing precise local conformity (see Supplementary Movie 7). A remarkably good agreement with the target domain and predictions is evinced in Fig. 6d, where experimental results are given for the third arc spline (see Supplementary Movie 8), while Fig. 6e extends the assessment to the global domain.

Despite their shape-shifting promise, there are limits to the approach here presented. First, the deformation of R-BB is an arc whose curvature is dominated by the opening angle and its length scale. If the latter is not constrained, R-BB can in principle capture an arc with any curvature, even one with tiny values resembling a sharp corner. In practice, however, the accuracy and resolution of the manufacturing process might pose restrictions in matching abrupt variations of curvature in the shape target. In addition, the proof-of-concepts tested in this work feature a trade-off between thermal and mechanical performance. In Fig. 6c, gravity was not considered in the morphing direction, since an additional body force could collapse the compliant kirigami material. The low stiffness is typically of kirigami concepts, where the open cuts naturally generate a severe penalty on the material resistance to deformation. Strategies to create stiff and durable kirigami have been proposed and could be implanted here[63]. Another approach is to change the base materials, here hardwood and silicone rubber, as well as the aspect ratio of BB, here quite large ($l/h = 9$). For example, a change of silicone rubber, the core material, with a solid of higher elastic modulus yet distinct CTE, such as polytetrafluoroethylene (PTFE)[64], and the selection of less slender BB can contribute to compensate the low stiffness observed in our proof-of-concepts. A third option to enhance stiffens in the deformed state is to envision an interlocking strategy that autonomously locks the material phenotype. While these seem promising paths to follow, further work is required to explore them.

The kirigami concepts here presented are complementary yet distinct to the morphing routes currently pursued with active materials. For shape memory polymers and other smart materials, the programming stage of the deformation response goes through a molecular design of their polymer network architectures which are either chemically or physically crosslinked. Through a synthesis process, the switching temperature is programmed, and in a small range of values nearby that temperature, the deformation is fully released with a switch-type response. In addition, the performance of shape memory polymers often worsens under thermomechanical cycles. The kirigami concepts here presented, on the other hand, do no require chemical, rather geometric, strategies applicable to several pairs of off-the-shelf solids including metals. If needed, the selection of the base materials can address the requirement of robustness to fluctuating thermal stress. In addition, the rational manipulation of their geometry, such as the size of the BB groove and the offset of the flexural hinge, allows to calibrate both the rate of deformation and the temperature range within which the response occurs. This geometric tuning offers significant freedom to generate desired types of response, including both sudden and smooth deformation, which could be gradually dispensed even over a large temperature span.

There are a number of potential applications for shape-matching materials across multiple sectors, especially where folding, packaging, and conformational changes are paramount requirements to meet[65], such as self-reconfigurable medical devices[7,66], drug delivery systems[18,33], autonomous soft robotics[67], and conformable stretchable electronics[68]. The advantages of the concepts here introduced can be capitalized in two primary applications. The first targets repeated and reversible reconfigurability in extreme climates on Earth and in space. Here the transportation of components is typically required in a flat configuration, the deployment is to occur *in-situ*, such as unfolding shelters in unsafe settings[69,70] or reconfigurable antennas in space[71,72], and reconfigurability can entail multiple loops of closure and opening, each controlled by temperature cycles. In these conditions, shape memory polymers and other active materials might not be the best fit, not only because their response is typically irreversible, but also because thermomechanical cycles can steadily decrease their performance. The second application is thermal management. Besides shape morphing, our concepts can be programmed to feature adaptive change in their out-of-plane porosity in response to temperature change. The transformation from a fully solid to a fully porous state through temperature change can bring about a large area of voids for heat exchange, conditions that can become an asset for cooling and thermal regulation.

Overall, our framework engages a fine interplay between geometry and mechanics of metaunits to enact morphing in response to temperature. It requires neither manipulation of constituent compositions nor chemical processes. It can predict local and global morphing, as well as reconfigure the morphology of aperiodic architectures

into predefined targets. Reversibility through temperature is one of its assets, along with the passive nature of the constituents, and the elimination of external power and control. A large design freedom to tune the thermal response (type, magnitude and rate of deformation) is at hand through manipulation of the internal architecture. Other pairs of passive solids including metals can in principle be used, as long as they offer a sizable distinction in CTE. Purposely implemented with simple yet efficient means of fabrication, our platform is well-suited to other technologies, e.g. multi-material 3D printing[8,73], offers routes for upscaling and downscaling, and can be also extended to active materials and other stimuli.

## Data availability

The data that support the findings of this work are available from the corresponding author upon request.

## References

1. Oliver, K., Seddon, A. & Trask, R. S. Morphing in nature and beyond: a review of natural and synthetic shape-changing materials and mechanisms. *Journal of Materials Science* **51**, 10663–10689, https://doi.org/10.1007/s10853-016-0295-8 (2016).
2. Yang, H. *et al.* 3D printed photoresponsive devices based on shape memory composites. *Advanced Materials* **29**, 1701627 (2017).
3. Ratna, D. & Karger-Kocsis, J. Recent advances in shape memory polymers and composites: a review. *Journal of Materials Science* **43**, 254–269 (2008).
4. Erb, R. M., Sander, J. S., Grisch, R. & Studart, A. R. Self-shaping composites with programmable bioinspired microstructures. *Nature communications* **4**, 1712 (2013).
5. Harke, B. *et al.* Polymerization inhibition by triplet state absorption for nanoscale lithography. *Advanced Materials* **25**, 904–909 (2013).
6. Ge, Q., Dunn, C. K., Qi, H. J. & Dunn, M. L. Active origami by 4D printing. *Smart Materials and Structures* **23**, 094007 (2014).
7. Xu, S. *et al.* Assembly of micro/nanomaterials into complex, three-dimensional architectures by compressive buckling. *Science* **347**, 154–159 (2015).
8. Ge, Q. *et al.* Multimaterial 4D printing with tailorable shape memory polymers. *Scientific reports* **6**, 31110 (2016).
9. Gladman, A. S., Matsumoto, E. A., Nuzzo, R. G., Mahadevan, L. & Lewis, J. A. Biomimetic 4D printing. *Nature materials* **15**, 413 (2016).
10. Haghpanah, B., Salari-Sharif, L., Pourrajab, P., Hopkins, J. & Valdevit, L. Multistable Shape-Reconfigurable Architected Materials. *Advanced Materials* **28**, 7915–7920 (2016).
11. Bertoldi, K., Vitelli, V., Christensen, J. & van Hecke, M. Flexible mechanical metamaterials. *Nature Reviews. Materials* **2**, 17066 (2017).
12. van Manen, T., Janbaz, S. & Zadpoor, A. A. Programming the shape-shifting of flat soft matter. *Materials Today* **21**, 144–163, https://doi.org/10.1016/j.mattod.2017.08.026 (2018).
13. Zykov, V., Mytilinaios, E., Adams, B. & Lipson, H. Robotics: Self-reproducing machines. *Nature* **435**, 163 (2005).
14. Felton, S., Tolley, M., Demaine, E., Rus, D. & Wood, R. A method for building self-folding machines. *Science* **345**, 644–646 (2014).
15. Hu, J., Meng, H., Li, G. & Ibekwe, S. I. A review of stimuli-responsive polymers for smart textile applications. *Smart Materials and Structures* **21**, 053001 (2012).
16. Randall, C. L., Gultepe, E. & Gracias, D. H. Self-folding devices and materials for biomedical applications. *Trends in biotechnology* **30**, 138–146 (2012).
17. Tomatsu, I., Peng, K. & Kros, A. Photoresponsive hydrogels for biomedical applications. *Advanced drug delivery reviews* **63**, 1257–1266 (2011).
18. Fernandes, R. & Gracias, D. H. Self-folding polymeric containers for encapsulation and delivery of drugs. *Advanced drug delivery reviews* **64**, 1579–1589 (2012).
19. Fedorovich, N. E. *et al.* Hydrogels as extracellular matrices for skeletal tissue engineering: state-of-the-art and novel application in organ printing. *Tissue engineering* **13**, 1905–1925 (2007).
20. Lagoudas, D. C. *Shape memory alloys: modeling and engineering applications*. (Springer, 2008).
21. Jeon, S.-J., Hauser, A. W. & Hayward, R. C. Shape-morphing materials from stimuli-responsive hydrogel hybrids. *Accounts of chemical research* **50**, 161–169 (2017).
22. Mishra, S. R., Dickey, M. D., Velev, O. D. & Tracy, J. B. Selective and directional actuation of elastomer films using chained magnetic nanoparticles. *Nanoscale* **8**, 1309–1313, https://doi.org/10.1039/C5NR07410J (2016).
23. Ramachandran, V., Bartlett, M. D., Wissman, J. & Majidi, C. Elastic instabilities of a ferroelastomer beam for soft reconfigurable electronics. *Extreme Mechanics Letters* **9**, 282–290, https://doi.org/10.1016/j.eml.2016.08.007 (2016).
24. Kim, Y., Yuk, H., Zhao, R., Chester, S. A. & Zhao, X. Printing ferromagnetic domains for untethered fast-transforming soft materials. *Nature* **558**, 274–279, https://doi.org/10.1038/s41586-018-0185-0 (2018).
25. Liu, Y. *et al.* Programmable responsive shaping behavior induced by visible multi-dimensional gradients of magnetic nanoparticles. *Soft Matter* **8**, 3295–3299 (2012).
26. Guan, J., He, H., Hansford, D. J. & Lee, L. J. Self-folding of three-dimensional hydrogel microstructures. *The Journal of Physical Chemistry B* **109**, 23134–23137 (2005).
27. Stoychev, G., Turcaud, S., Dunlop, J. W. & Ionov, L. Hierarchical multi-step folding of polymer bilayers. *Advanced Functional Materials* **23**, 2295–2300 (2013).
28. Tolley, M. T. *et al.* Self-folding origami: shape memory composites activated by uniform heating. *Smart Materials and Structures* **23**, 094006 (2014).
29. Egunov, A., Korvink, J. & Luchnikov, V. Polydimethylsiloxane bilayer films with an embedded spontaneous curvature. *Soft matter* **12**, 45–52 (2016).
30. Stoychev, G., Guiducci, L., Turcaud, S., Dunlop, J. W. & Ionov, L. Hole-Programmed Superfast Multistep Folding of Hydrogel Bilayers. *Advanced Functional Materials* **26**, 7733–7739 (2016).
31. Mohd Jani, J., Leary, M., Subic, A. & Gibson, M. A. A review of shape memory alloy research, applications and opportunities. *Materials & Design (1980-2015)* **56**, 1078–1113, https://doi.org/10.1016/j.matdes.2013.11.084 (2014).
32. Behl, M. & Lendlein, A. Shape-memory polymers. *Kirk-Othmer Encyclopedia of Chemical Technology*, 1–16 (2000).
33. Qiu, Y. & Park, K. Environment-sensitive hydrogels for drug delivery. *Advanced drug delivery reviews* **53**, 321–339 (2001).
34. Bauhofer, A. A. *et al.* Harnessing Photochemical Shrinkage in Direct Laser Writing for Shape Morphing of Polymer Sheets. *Advanced Materials* **29**, 1703024 (2017).
35. Jamal, M., Zarafshar, A. M. & Gracias, D. H. Differentially photo-crosslinked polymers enable self-assembling microfluidics. *Nature communications* **2**, 527 (2011).

36. Chen, C.-M., Reed, J. C. & Yang, S. Guided wrinkling in swollen, pre-patterned photoresist thin films with a crosslinking gradient. *Soft Matter* **9**, 11007–11013 (2013).
37. Jamal, M. *et al*. Bio-origami hydrogel scaffolds composed of photocrosslinked PEG bilayers. *Advanced healthcare materials* **2**, 1142–1150 (2013).
38. Na, J. H. *et al*. Programming reversibly self-folding origami with micropatterned photo-crosslinkable polymer trilayers. *Advanced Materials* **27**, 79–85 (2015).
39. Ge, Q., Qi, H. J. & Dunn, M. L. Active materials by four-dimension printing. *Applied Physics Letters* **103**, 131901 (2013).
40. Ionov, L. Polymeric actuators. *Langmuir* **31**, 5015–5024 (2014).
41. Filipov, E. T., Tachi, T. & Paulino, G. H. Origami tubes assembled into stiff, yet reconfigurable structures and metamaterials. *Proceedings of the National Academy of Sciences* **112**, 12321–12326 (2015).
42. Faber, J. A., Arrieta, A. F. & Studart, A. R. Bioinspired spring origami. *Science* **359**, 1386–1391 (2018).
43. Hawkes, E. *et al*. Programmable matter by folding. *Proceedings of the National Academy of Sciences* **107**, 12441–12445 (2010).
44. Silverberg, J. L. *et al*. Using origami design principles to fold reprogrammable mechanical metamaterials. *science* **345**, 647–650 (2014).
45. Dudte, L. H., Vouga, E., Tachi, T. & Mahadevan, L. Programming curvature using origami tessellations. *Nature materials* **15**, 583 (2016).
46. Blees, M. K. *et al*. Graphene kirigami. *Nature* **524**, 204 (2015).
47. Hwang, D.-G. & Bartlett, M. D. Tunable Mechanical Metamaterials through Hybrid Kirigami Structures. *Scientific Reports* **8**, 3378, https://doi.org/10.1038/s41598-018-21479-7 (2018).
48. Castle, T. *et al*. Making the cut: Lattice kirigami rules. *Physical review letters* **113**, 245502 (2014).
49. Overvelde, J. T. *et al*. A three-dimensional actuated origami-inspired transformable metamaterial with multiple degrees of freedom. *Nature communications* **7**, 10929 (2016).
50. Overvelde, J. T., Weaver, J. C., Hoberman, C. & Bertoldi, K. Rational design of reconfigurable prismatic architected materials. *Nature* **541**, 347 (2017).
51. Coulais, C., Teomy, E., de Reus, K., Shokef, Y. & van Hecke, M. Combinatorial design of textured mechanical metamaterials. *Nature* **535**, 529 (2016).
52. Sigmund, O. & Torquato, S. Design of materials with extreme thermal expansion using a three-phase topology optimization method. *Journal of the Mechanics and Physics of Solids* **45**, 1037–1067 (1997).
53. Lakes, R. Cellular solids with tunable positive or negative thermal expansion of unbounded magnitude. *Applied Physics Letters* **90**, 221905 (2007).
54. Ha, C. S., Hestekin, E., Li, J., Plesha, M. E. & Lakes, R. S. *Controllable thermal expansion of large magnitude in chiral negative Poisson's ratio lattices. physica status solidi (b)* **252**, 1431–1434 (2015).
55. Jefferson, G., Parthasarathy, T. A. & Kerans, R. J. Tailorable thermal expansion hybrid structures. *International Journal of Solids and Structures* **46**, 2372–2387 (2009).
56. Wang, Q. *et al*. Lightweight Mechanical Metamaterials with Tunable Negative Thermal Expansion. *Physical Review Letters* **117**, 175901 (2016).
57. Yamamoto, N. *et al*. Thin Films with Ultra-low Thermal Expansion. *Advanced Materials* **26**, 3076–3080 (2014).
58. Xu, H. & Pasini, D. Structurally Efficient Three-dimensional Metamaterials with Controllable Thermal Expansion. *Scientific Reports* **6**, 34924 (2016).
59. Xu, H., Farag, A. & Pasini, D. Routes to program thermal expansion in three-dimensional lattice metamaterials built from tetrahedral building blocks. *Journal of the Mechanics and Physics of Solids* **117**, 54–87 (2018).
60. Steeves, C. A. *et al*. Concepts for structurally robust materials that combine low thermal expansion with high stiffness. *Journal of the Mechanics and Physics of Solids* **55**, 1803–1822 (2007).
61. Wei, K., Chen, H., Pei, Y. & Fang, D. Planar lattices with tailorable coefficient of thermal expansion and high stiffness based on dual-material triangle unit. *Journal of the Mechanics and Physics of Solids* **86**, 173–191 (2016).
62. Lehman, J. & Lakes, R. S. Stiff, strong, zero thermal expansion lattices via material hierarchy. *Composite Structures* **107**, 654–663 (2014).
63. Shang, X., Liu, L., Rafsanjani, A. & Pasini, D. Durable bistable auxetics made of rigid solids. *Journal of Materials Research* **33**, 300–308, https://doi.org/10.1557/jmr.2017.417 (2017).
64. Xu, H., Farag, A. & Pasini, D. Multilevel hierarchy in bi-material lattices with high specific stiffness and unbounded thermal expansion. *Acta Materialia* **134**, 155–166 (2017).
65. Zhang, Y. *et al*. Printing, folding and assembly methods for forming 3D mesostructures in advanced materials. *Nature Reviews Materials* **2**, 17019 (2017).
66. Kuribayashi, K. *et al*. Self-deployable origami stent grafts as a biomedical application of Ni-rich TiNi shape memory alloy foil. *Materials Science and Engineering: A* **419**, 131–137 (2006).
67. Han, D. *et al*. Soft Robotic Manipulation and Locomotion with a 3D Printed Electroactive Hydrogel. *ACS applied materials & interfaces* (2018).
68. Rogers, J., Huang, Y., Schmidt, O. G. & Gracias, D. H. Origami MEMS and NEMS. *Mrs Bulletin* **41**, 123–129 (2016).
69. Verge, A. S. Rapidly deployable structures in collective protection systems. (Army Soldier and Biological Chemical Command Natick MA, 2006).
70. Mejia-Ariza, J., Murphey, T. & Pollard, E. In *47th AIAA/ASME/ASCE/AHS/ASC Structures, Structural Dynamics, and Materials Conference 14th AIAA/ASME/AHS Adaptive Structures Conference 7th* (1686).
71. Miura, K. Method of packaging and deployment of large membranes in space. *Title The Institute of Space and Astronautical Science Report* **618**, 1 (1985).
72. Moon, F. & Abel, J. Nonlinear dynamics of deployable and maneuverable space structures. (CORNELL UNIV ITHACA NY, 1993).
73. Sugavaneswaran, M. & Arumaikkannu, G. Modelling for randomly oriented multi material additive manufacturing component and its fabrication. *Materials & Design (1980-2015)* **54**, 779–785 (2014).

## Acknowledgements

## Author contributions

D.P. conceived the morphing framework and formulated the constituent problems. L.L. conducted all the theoretical and computational analyses with close direction from D.P. C.Q. assisted L.L. with sample fabrication and experiments, and H.A. with the optimization problems. D.P. wrote the manuscript.

## Competing interests

The authors declare no competing interests.

## Additional information

**Supplementary information** is available for this paper at https://doi.org/10.1038/s41598-019-56118-2.

**Correspondence** and requests for materials should be addressed to D.P.

**Reprints and permissions information** is available at www.nature.com/reprints.

**Publisher's note** Springer Nature remains neutral with regard to jurisdictional claims in published maps and institutional affiliations.

# Encoding kirigami bi-materials to morph on target in response to temperature

Lu Liu, Chuan Qiao, Haichao An, Damiano Pasini *

Department of Mechanical Engineering, McGill University, Macdonald Engineering Building, Room 372, 817 Sherbrooke Street West
Montreal, Quebec, H3A 0C3, Canada, Tel.  514 398 6295

* e-mail: Damiano.pasini@mcgill.ca

## S1. Testing apparatus

Supplementary Fig. S1 shows the schematic of the experimental set-up built to test the thermal deformation of the fabricated metamaterials. The heating chamber consisted of two 200-Watt strip heaters (McMaster-Carr, USA) placed underneath the testing plate, where the temperature was adjusted through a proportion-integration-differentiation (PID) controller (CN7800, OMEGA, USA & Canada). A data acquisition system (cDAQ-9174, National Instruments, USA) was used to collect the temperature values from the thermocouples placed at different locations in the heating chamber with the goal of assessing any instance of temperature heterogeneity throughout the heating chamber. A borosilicate glass cover was placed on the top of the testing system to provide a thermal insulation shield. Specimens were tested both in air and oil, the latter to provide a uniform source of heating and eliminate frictional dissipation between the specimen and the testing plate.

Digital Image Correlation was used to capture the full-field displacement and effective thermal strain of the specimen at increasing levels of temperature. Supplementary Fig. S2 illustrates a representative set of testing on a periodic metamaterial with compound units. Any rigid body movement of the specimen was prevented by anchoring one point (highlighted in red in Supplementary Fig. S2a) of the specimen to the testing plate. Two pairs of black speckles were applied on the rigid frame to trace their movement. Temperature gradually increased from 20 to 120 ℃. Sample deformation was first captured by a digital camera (EOS Rebel T6i, Canon USA), and then processed with a correlation algorithm (Vic-2D, Correlated Solutions Inc., USA) that provided the full-field displacement and strain data between pairs of black speckles in the deformed specimen. The effective thermal strains ($\varepsilon_{yy}^*$) was then obtained from the relative displacement normalized by the initial distance between pairs of black speckles. As an illustrative example, Supplementary Fig. S2 on the bottom of each of the six snapshots provides the $\varepsilon_{yy}^*$ values at two specimen locations for varying levels of temperature.
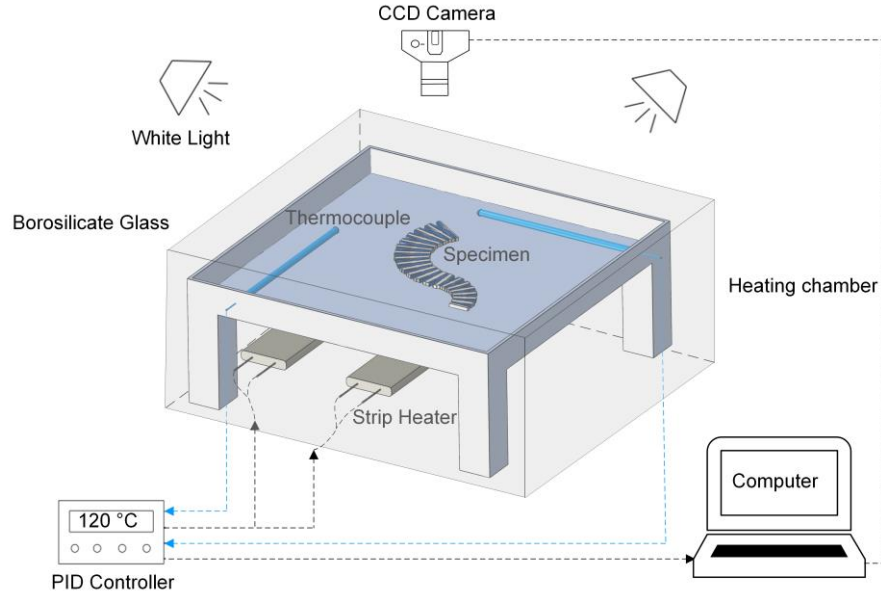
Supplementary Fig. S1: Schematic of the experimental set-up.
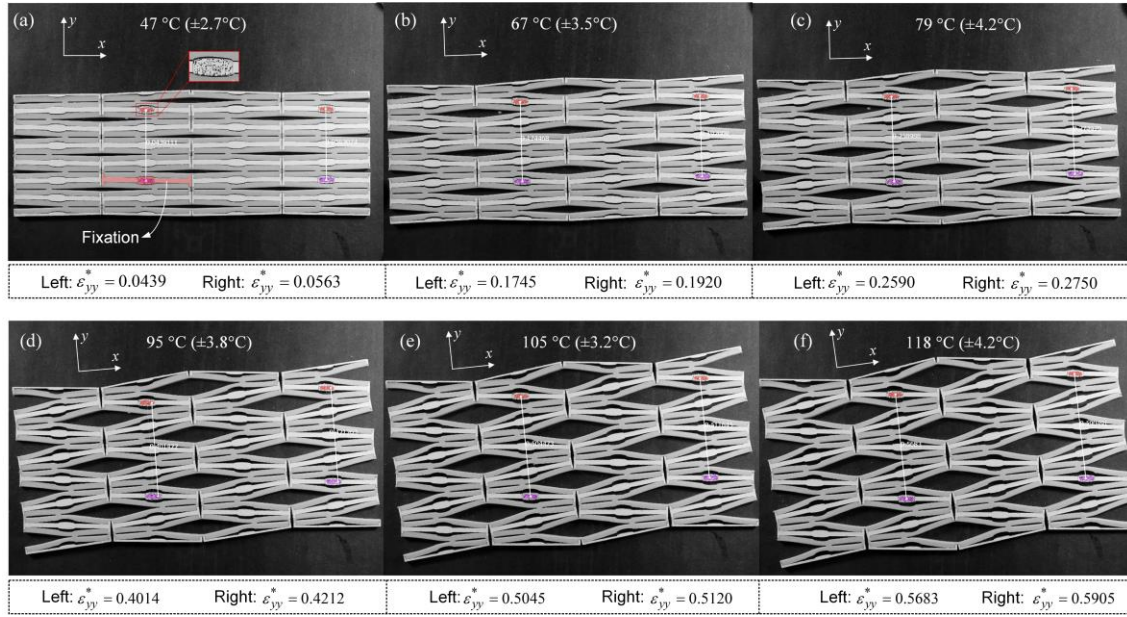


Supplementary Fig. S2: Illustrative snapshots of thermal deformation measures at given values of temperature. Effective values of thermal strain $\varepsilon_{yy}^*$ obtained from measurements between pairs of elliptical regions with speckles dispensed on the wooden frame (see insert on the top of (a)).

## S2. Characterization of constituent properties: thermal expansion coefficient and Young's modulus

A thermomechanical analyzer (TMA Q400, TA Instruments Inc., USA) was used to measure the coefficient of thermal expansion (CTE) of the constituent solids, silicone rubber and hardwood. For the latter, the CTE was measured in both directions, parallel and perpendicular to the wood grain. Supplementary Fig. S3a reports the CTE for both materials with measured values ( $\alpha_{rubber} = 215 \times 10^{-6} K^{-1}$, $\alpha_{//grain} = 5 \times 10^{-6} K^{-1}$, and $\alpha_{\perp grain} = 32 \times 10^{-6} K^{-1}$) almost constant throughout the temperature range under investigation (20 to 120 °C).

To assess the tensile elastic modulus of the constituents, we tested a set of laser-cut dumbbell-shaped specimens (Supplementary Fig. S3b) with an Instron tensile tester (5982 Series Universal Testing Systems, Instron Inc., USA). For silicone rubber, 3 uniaxial tensile tests were performed under displacement control, from which the most representative nominal stress-strain curve was obtained. To capture the experimental measures, a first order Ogden model was adopted (Supplementary Fig. S3c) with strain energy function given by:

$$W(\lambda_1, \lambda_2, \lambda_3) = \frac{\mu}{\alpha}(\lambda_1^\alpha + \lambda_2^\alpha + \lambda_3^\alpha - 3) \tag{1}$$

where $\mu$ and $\alpha$ are the material constants chosen to fit the experimental data (in this case $\mu = 1.03$ and $\alpha = 6.20$), and $\lambda_1, \lambda_2,$ and $\lambda_3$ denotes the principal stretches. In addition, the elastic modulus of silicone rubber was extracted from the curve at 25% strain ($E_{25\%} = 3.7$ MPa) and used in our analyses.

For the elastic response of wood, uniaxial tensile tests were performed on specimens with orientation either parallel or perpendicular to the wood grain direction (Supplementary Fig. S3b). Ten dumbbell-shaped specimens were laser cut from a 1/8-inch-thick sheet of hardwood. Supplementary Fig. S3d reports the representative stress-strain curves of the experiments, from which we extracted the following mean values for the Young's moduli: $E_{//grain} = 12.0 \pm 0.3$ GPa, and $E_{\perp grain} = 0.97 \pm 0.09$ GPa.
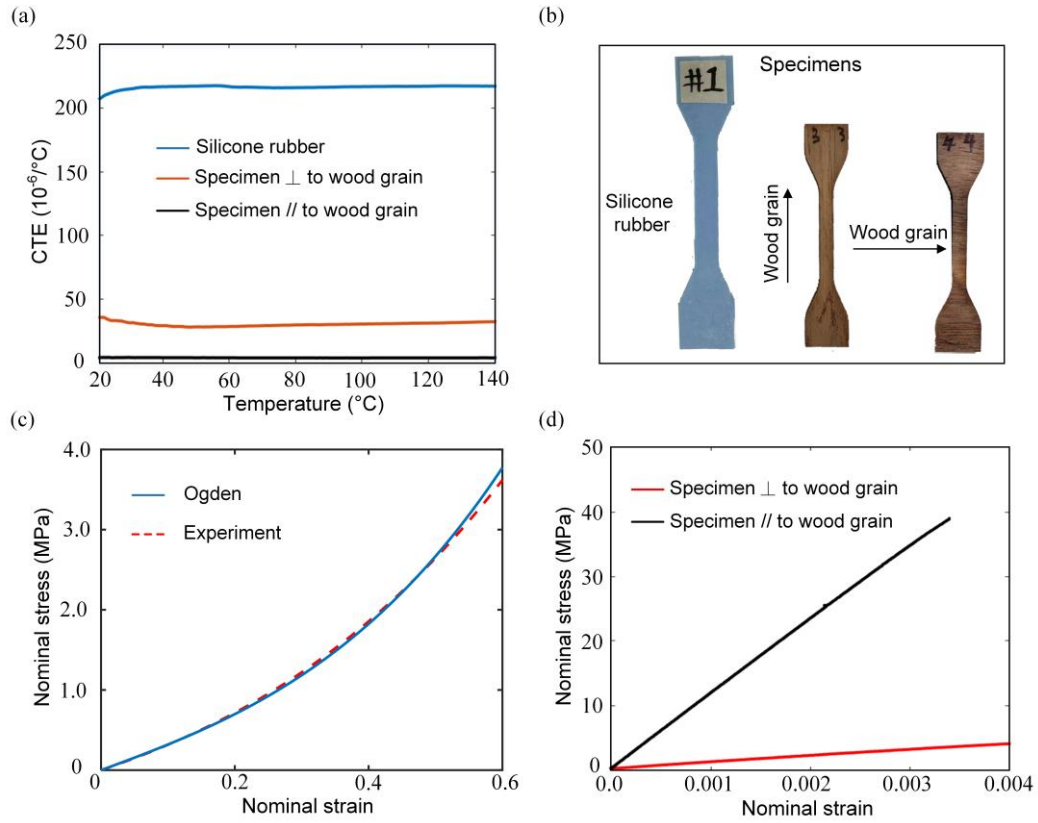
Supplementary Fig. S3: Characterization of material constituents. (a) Experimental measures of the coefficient of thermal expansion for silicone rubber and hardwood. (b) Dumbbell-shaped specimens for uniaxial tensile test. (c) Experimental nominal stress-strain curve of silicone rubber and Ogden fit response. (d) Stress-strain curves obtained from testing hardwood specimens oriented in the direction parallel and perpendicular to the wood grain.

**S3. Metaunit analysis: unidirectional and rotational response**

**S3-A. Theoretical model**

This section examines the mechanics of the functional building block shown in Fig.1a subject to a uniform thermal field. We theoretically study the temperature-driven deformation for both the unidirectional and rotational floppy modes. Theoretical expressions for the elastic deflection of both U-BB and R-BB are obtained as a function of temperature, $T$, under the following assumptions:

- Both constituent solids have constant CTE within the temperature range here investigated.
- Hooke's law of elasticity holds for the high CTE core.
- The low CTE frame is assumed rigid, therefore the deformation induced by the thermal mismatch of the two materials is neglected.
- The length $d$ of the connection between the upper and lower portions of the high CTE core is considered significantly smaller than the BB length ($d \ll l$).

**i. Unidirectional Building Block (U-BB)**

Supplementary Fig. S4a shows U-BB in its undeformed state: two distinct portions joined centrally via a connection of length $d$ along the horizontal axis of symmetry. Each is shaped with a low CTE (grey) and high CTE (blue) material, where $l$ and width $h$ describe the length and width of the core, which is cut along semi ellipses with major axis of length $2a$ and minor axis of length $2b$. The thermal mismatch between the low CTE confinement (grey) and the high CTE expansion (blue) (Supplementary Fig. S4b) governs the unidirectional response that is endowed by the BB topology. A temperature increase expands the core, which is constricted horizontally by the surrounding frame, and thus forced along its floppy direction to space the upper and lower portion of the BB by $\Delta h$, here assumed anchored at its center. Due to the negligible thermal expansion of the low CTE solid, an effective boundary condition is enforced to replace the frame action onto the core. For the sake of symmetry, a quarter of the core is examined with one end clamped and the other free to move transversely via a guided support (Supplementary Fig. S4c). In addition, we simplify the semielliptical quarter of the groove by straightening its profile so as to form an inclined beam, which is in turn attached to the preceding horizontal part. The analysis of the building block subjected to uniform temperature is now reduced to the solution of a statically indeterminate problem of a Timoshenko beam-column (Supplementary Fig. S4d) with an equivalent CTE, $\alpha_{\text{effective}} = \alpha_{\text{core}} - \alpha_{\text{frame}}$, compensating the neglect of the thermal expansion of the frame.
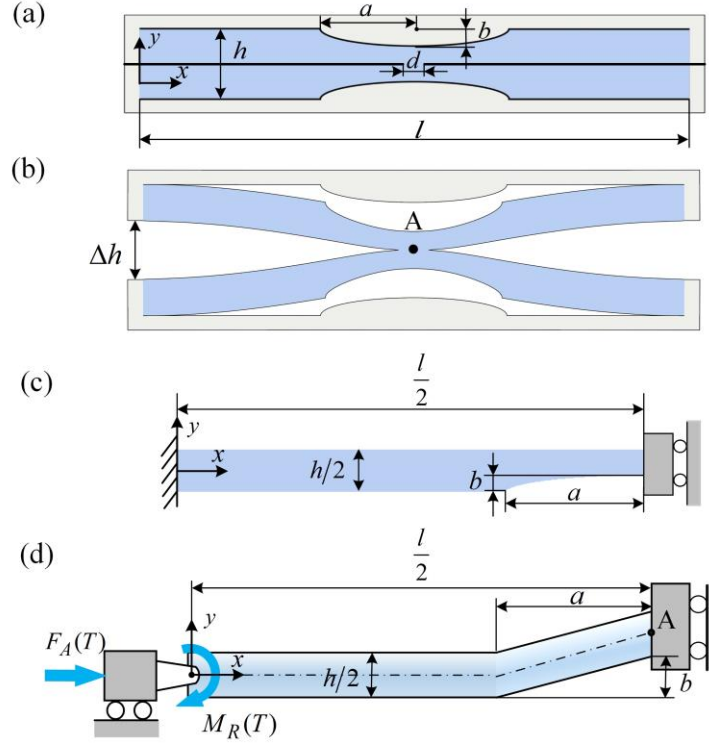
Supplementary Fig. S4: (a) Geometry of unidirectional building block, U-BB, with its dimensional parameters. (b) Deformed U-BB with expansion $\Delta h$ depicted at a given temperature, $T$. (c) Condensed model of U-BB, where the nominal geometry is reduced to that of an effective core with $\alpha_{\text{effective}} = \alpha_{\text{core}} - \alpha_{\text{frame}}$ subject to $\Delta T$ and pertinent boundary conditions. (d) Further model reduction to a statically determinate Timoshenko beam-column subjected to reaction forces, $F_A$ and $M_R$, both dependent on $T$.

By releasing redundant constraints on the clamped end of the beam-column, the model in Supplementary Fig. S4c becomes statically determinate (Supplementary Fig. S4d). Its corresponding axial force ($F_A(T)$) and bending moment ($M_R(T)$) that both depend upon the level of temperature, as well as its deflection can be obtained through the solution of the following set of second-order differential equations:

$$\begin{cases} \dfrac{d^2v}{dx^2} = -\dfrac{F_A(T)}{EI}v + \dfrac{M_R(T)}{EI}, & 0 \le x \le \left(\dfrac{l}{2} - a\right) \\ \dfrac{d^2v}{dx^2} = -\dfrac{F_A(T)}{EI}\left[v + \dfrac{b}{a}\left(x - \dfrac{l}{2} + a\right)\right] + \dfrac{M_R(T)}{EI}, & \left(\dfrac{l}{2} - a\right) < x \le \dfrac{l}{2} \end{cases} \quad (2)$$

where $v$ is the transverse deflection along the $y$ axis of the beam, and it represents the difference between the deformed and undeformed axis of the beam-column. $E$ and $I$ are the Young's modulus and the second moment of area of the beam cross-section. The following notation applies:

$$k^2 = \frac{F_A(T)}{EI}, \quad mk^2 = \frac{M_R(T)}{EI}, \quad l_1 = \frac{l}{2} - a \quad (3)$$

7

which is substituted into Eqns. (2) and yields:

$$\begin{cases} \dfrac{d^2v}{dx^2} = -k^2v + mk^2, & 0 \leq x \leq l_1 \\ \dfrac{d^2v}{dx^2} = -k^2\left[v + \dfrac{b}{a}(x - l_1)\right] + mk^2, & l_1 < x \leq \dfrac{l}{2} \end{cases} \tag{4}$$

The general solutions of Eqns. (4) have the form:

$$\begin{cases} v(x) = C_1 \sin(kx) + C_2 \cos(kx) + m, & 0 \leq x \leq l_1 \\ v(x) = C_3 \sin(kx) + C_4 \cos(kx) + \dfrac{b}{a}(l_1 - x) + m, & l_1 < x \leq \dfrac{l}{2} \end{cases} \tag{5}$$

The constants of integration $C_1$ and $C_2$ can be determined from the boundary conditions. Since the beam is clamped at the left end, we impose:

$$v|_{x=0} = 0, \quad \left.\frac{dv}{dx}\right|_{x=0} = 0 \tag{6}$$

To determine the constants of integration $C_3$ and $C_4$, continuity on deflection and slope is enforced at the junction between the two portions of the beam, thus yielding:

$$v|_{x=l_1^+} = v|_{x=l_1^-}, \quad \left.\frac{dv}{dx}\right|_{x=l_1^+} = \left.\frac{dv}{dx}\right|_{x=l_1^-} \tag{7}$$

Substituting into Eqns. (5) the values of the integration constants from Eqns. (6) and (7) allows the calculation of the deflection curve $v(x)$. By adding the initial ordinates of the undeformed axis to the transverse deflection of the beam, we obtain the final ordinates of the deflection curve for both portions of the beam:

$$\begin{cases} y(x) = -m\cos(kx) + m, & 0 \leq x \leq l_1 \\ y(x) = -\left[m + \dfrac{b}{ak}\sin(kl_1)\right]\cos(kx) + \dfrac{b}{ak}\cos(kl_1)\sin(kx) + m, & l_1 < x \leq \dfrac{l}{2} \end{cases} \tag{8}$$

With the above equations of the deflection curve, we can determine the force $F_A$ and moment $M_R$ by imposing pertinent compatibility conditions. The first specifies that at the right end support of the beam:

$$\left.\frac{dy}{dx}\right|_{x=\frac{l}{2}} = \frac{b}{a} \tag{9}$$

Substitution of Eqns. (8) into Eqn. (9) yields the first compatibility equation:

$$\left[mk + \frac{b}{a}\sin(kl_1)\right]\sin\left(\frac{kl}{2}\right) + \frac{b}{a}\cos(kl_1)\cos\left(\frac{kl}{2}\right) = \frac{b}{a} \tag{10}$$

The second comes from the observation that upon heating any change in the beam length is caused by the sum of two portions: (1) the elongation produced by the thermal expansion of the beam, and (2) the contraction caused by the axial force acting on the beam. This relation can be expressed as:

$$s(T) - s(T_0) = \Delta s_{\text{expansion}} + \Delta s_{\text{compression}} \tag{11}$$

where $s(T_0)$ and $s(T)$ are the length of the beam axis at room temperature $T_0$ and at a higher temperature $T$, respectively. $\Delta s_{\text{thermal}}$ and $\Delta s_{\text{compression}}$ represent the length change of the beam caused by thermal expansion and axial compression, respectively. The expressions are given by:

$$
\begin{aligned}
s(T) - s(T_0) &= \int_0^{l_1}(ds - dx) + \int_{l_1}^{\frac{l}{2}}\left(ds - dx\sqrt{1 + (b/a)^2}\right) \\
\Delta s_{\text{thermal}} &= \alpha_{\text{effective}}(T - T_0)\left(l_1 + a\sqrt{1 + (b/a)^2}\right) \\
\Delta s_{\text{compression}} &= -\frac{F_A l}{2EA}
\end{aligned} \tag{12}
$$

Substitution of Eqns. (12) into Eqn. (11) results in the second compatibility equation:

$$
\begin{aligned}
&\frac{1}{8}\left[k^2 m^2 l + \frac{2b^2}{a} + \frac{2mb}{a}\cos(kl_1) + 4mkb\sin(kl_1) - km^2\sin(kl) - \frac{2mb}{a}\cos(kl - kl_1)\right. \\
&\left. + \frac{b^2}{a^2 k}\sin(2ka)\right] + a\left(1 - \sqrt{1 + (b/a)^2}\right) + \frac{F_A l}{2EA} - \alpha_{\text{effective}}(T - T_0)\left(l_1 + a\sqrt{1 + (b/a)^2}\right) = 0
\end{aligned} \tag{13}
$$

Since a compact closed-form for $F_A(T)$ and $M_R(T)$ cannot be directly retrieved from the above equations, we numerically solve Eqns. (13) and (10) and use the Newton–Raphson method to find their roots. The deflection curve $y_T(x)$ of the beam at a given temperature $T$ can then be obtained by substituting the roots of $F_A(T)$ and $M_R(T)$ into Eqns. (8). The expansion of the building block $\Delta h$ at a given temperature $T$ is thus determined by calculating the transverse displacement of the beam at point A, expressed by:

$$
\Delta h(T) = 2\left[y_T\left(\frac{l}{2}\right) - b\right] \tag{14}
$$

### ii. Deformation mode of U-BB

The above theory can now be used to investigate the deformation mechanism of U-BB for an increasing level of temperature. To do so, we examine a representative beam-column with given parameters $l/h$ =9, $2a/l$ =0.1, and $2b/h$ =0.2 and plot the reaction and bending moment at the beam end. Supplementary Fig. S5a shows the results with the axial force $F_A$ and bending moment $M_R$ plotted as a function of the temperature range here investigated. To rule out size dependency in the plot, $F_A$ and $M_R$ are normalized with the cross-sectional dimensions $h/2$ and $t_t$, the latter representing the out-of-plane thickness of BB. Two sequential regimes of deformation can be observed, each controlled by temperature. For low values of temperature, the axial force dominates the bending moment and increases linearly with temperature; here axial compression governs the U-BB response. With a further increase of temperature, the deformation mode switches. Bending increases steeply and non-linearly, and the axial force flattens at a plateau with a resulting bending domination at high temperature. This is also apparent in Supplementary Fig. S5b, where a transition from a stretching to a bending mode appears in an intermediate zone (grey) around $T$=60 °C. Below this zone, i.e. in the low temperature regime, the change in slope of $\Delta h/h$ shows a moderate

expansion induced by extension. In contrast above the transition zone, U-BB expansion is controlled by internal bending of the core with a rate of $\Delta h/h$ that increase swiftly and non-linearly with temperature.
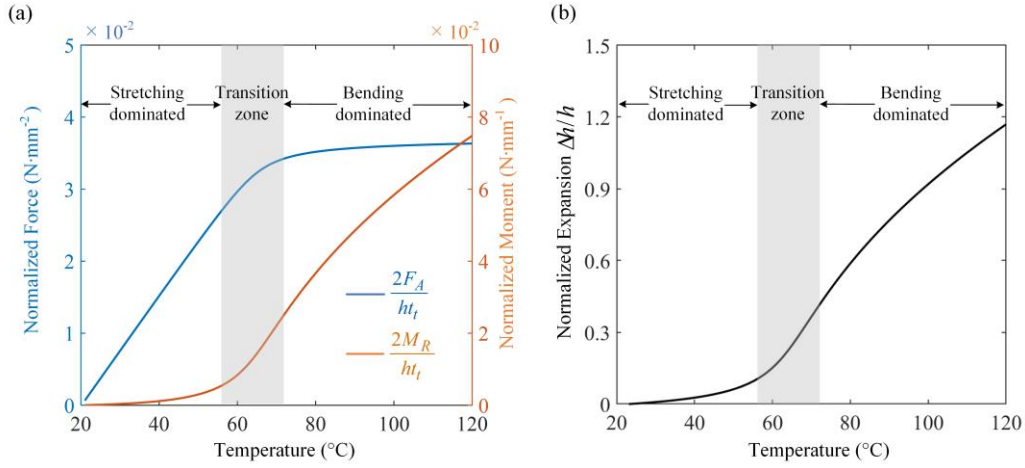


Supplementary Fig. S5: (a) Evolution of normalized $F_A$ and $M_R$ as a function of temperature in the temperature range 20 to 120 °C. (b) Normalized expansion $\Delta h/h$ as a function of temperature with slope showing BB sensitivity to temperature variation in the low and high temperature regime, respectively below and above the transition zone.

### iii. Rotational Building Block (R-BB)

R-BB differs from U-BB for a mere symmetry breaking as well as end closure of the core. They both seal R-BB with a rotational character. Supplementary Fig. S6a shows a shift in the position of the connection $d$ of the core at an offset $e$ from the left end of R-BB. The underlying mechanism of thermal deformation does not differ from that of U-BB, i.e. the trigger is the CTE mismatch of the constituents, but the topological difference between the two (U versus R) is responsible for each floppy mode (Supplementary Fig. S6b).

To study the theory governing R-BB mechanics, we amend the beam-column model previously examined for U-BB in Supplementary Fig. S4. Deformation symmetry in R-BB occurring along the dash-dot axis (Supplementary Fig. S6b) enables us to focus on the lower half of the high CTE core only, this time with both ends clamped. The reaction from the upper part is equivalent to a bending moment ($M_S(T)$) applied at A, i.e. the core connection (Supplementary Fig. S6c). By releasing redundant constraints on the clamped end (Supplementary Fig. S6d), we obtain three reaction forces $F_A(T)$, $F_V(T)$, and $M_R(T)$ with values dependent on temperature. As opposed to the U-BB analysis, this time a transverse force $F_V$ appears to balance $M_S$.
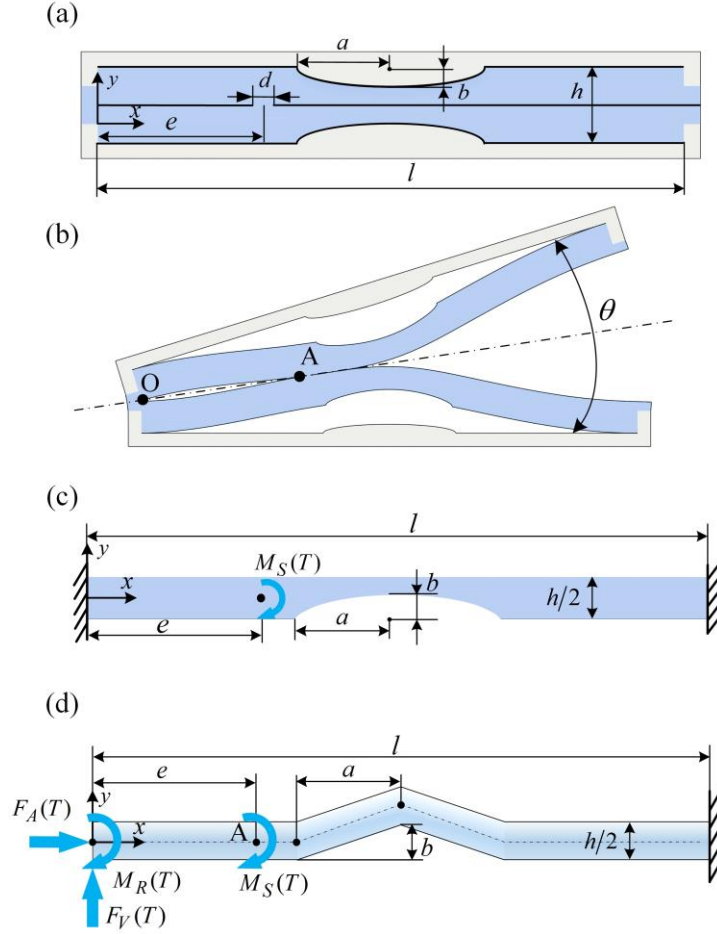
Supplementary Fig. S6: (a) Geometry of rotational building block, R-BB. (b) Deformed R-BB with opening angle $\theta$ shown at a given $T$. (c) Reduced model for BB analysis, where the R-BB is simplified to the high CTE core subject to $T$ and pertinent boundary conditions. (d) The high CTE core model is here condensed to a statically determinate Timoshenko beam-column with reaction and internal forces $F_A$, $F_V$, $M_R$ and $M_S$, all dependent on temperature.

Supplementary Fig. S6d shows the four portions of the Timoshenko beam-column representing R-BB. Similar to the U-BB analysis of the preceding section, also here we obtain the ordinates of the deflection curve for the five segments of the polygonal beam:

$$\begin{cases} y(x) = C_1 \sin(kx) + C_2 \cos(kx) + m + nx, & 0 \le x < e \\ y(x) = C_3 \sin(kx) + C_4 \cos(kx) + m + p + nx, & e \le x < l_1 \\ y(x) = C_5 \sin(kx) + C_6 \cos(kx) + m + p + nx, & l_1 \le x < l/2 \\ y(x) = C_7 \sin(kx) + C_8 \cos(kx) + m + p + nx, & l/2 \le x < l_2 \\ y(x) = C_9 \sin(kx) + C_{10} \cos(kx) + m + p + nx, & l_2 \le x \le l \end{cases} \quad (15)$$

where

$$k^2 = \frac{F_A}{EI}, \quad mk^2 = \frac{M_R}{EI}, \quad nk^2 = \frac{F_V}{EI}, \quad pk^2 = \frac{M_S}{EI}, \quad l_1 = \frac{l}{2} - a, \quad l_2 = \frac{l}{2} + a \quad (16)$$

11

The constants of integration $C_1, C_2, \ldots, C_{10}$ are determined from the boundary conditions and continuity at the junction between neighbouring portions of the beam:

$$
\begin{aligned}
C_1 &= -\frac{n}{k}, & C_2 &= -m, \\
C_3 &= C_1 - p\sin(ke), & C_4 &= C_2 - p\cos(ke), \\
C_5 &= C_3 + \frac{b}{ak}\cos(kl_1), & C_6 &= C_4 - \frac{b}{ak}\sin(kl_1), \\
C_7 &= C_5 - \frac{2b}{ak}\cos\left(\frac{kl}{2}\right), & C_8 &= C_6 + \frac{2b}{ak}\sin\left(\frac{kl}{2}\right), \\
C_9 &= C_7 + \frac{b}{ak}\cos(kl_2), & C_{10} &= C_8 - \frac{b}{ak}\sin(kl_2),
\end{aligned}
\tag{17}
$$

The reactions forces $(F_A, F_V, M_R, M_S)$ are now obtained by imposing four pertinent compatibility conditions. First, Eqn. (11), which for U-BB retains beam length compatibility upon heating, still holds for R-BB. Hence, substituting the expression of $s(T) - s(T_0)$, $\Delta s_{\text{thermal}}$, and $\Delta s_{\text{compression}}$ into Eqn. (11) results in:

$$
\int_0^{l_1} (ds - dx) + \int_{l_1}^{l_2} \left(ds - dx\sqrt{1 + r^2}\right) + \int_{l_2}^{l} (ds - dx) + \frac{F_A l}{EA}
$$
$$
- \alpha_{\text{effective}}(T - T_0)\left(l - 2a + 2a\sqrt{1 + (b/a)^2}\right) = 0
\tag{18}
$$

In addition, the following two apply to the right end support of the beam:

$$
y(l) = 0 \tag{19}
$$

$$
\left.\frac{dy}{dx}\right|_{x=l} = 0 \tag{20}
$$

The fourth condition stems from the deformation symmetry along the OA line that exists in the deformed R-BB (Supplementary Fig. S6b). This translates into an equivalent condition of slope between point A (offset of $e$ from O), and the symmetry axis (OA), here expressed as:

$$
\left.\frac{dy}{dx}\right|_{x=e} = \frac{y(e)}{e} \tag{21}
$$

Also in this case, we resort to the Newton–Raphson method to numerically solve the reaction force $F_A, F_V, M_R, M_S$ from the system of Eqns. (18)-(21). After the deflection curve $y_T$ of the beam at a given temperature $T$ is obtained by substituting their roots into Eqns. (15), we can express the opening angle, $\theta$, of R-BB at a given temperature $T$ through the slope of point A on the deflection curve as:

$$
\theta(T) = 2\arctan\left(\left.\frac{dy_T}{dx}\right|_{x=e}\right) \tag{22}
$$

### iv. Deformation mode of R-BB

Similar to the U-BB investigation on the mechanism of deformation, here we study the deformation behaviour of R-BB. As a representative model, a beam-column is examined with $l/h =9$, $2a/l =0.1$, $2b/h =0.2$, $2e/l =0.8$. Supplementary Fig. S7a and b plot its reaction and internal forces $F_A$, $F_V$, $M_R$, and $M_S$ as a function of increasing temperature. The trends (Supplementary Fig. S7a) are similar to those of U-BB:

two temperature dependent modes with deformation switch from stretching to bending occurring above the transition zone (grey). In Supplementary Fig. S7b the magnitude of $F_V$ and $M_S$ are respectively two and one order lower than $F_A$ and $M_R$ in Supplementary Fig. S7a. This result indicates that the transverse force and bending moment at the connection (point A in Supplementary Fig. S6d) contribute only slightly to the R-BB deformation. Furthermore, Supplementary Fig. S7c shows the temperature driven response of R-BB, where the slope of the opening angle ($\theta$) indicates a mild deformation dominated by extension in the low temperature regime, as opposed to above, where BB responds with internal bending with a deformation that is rapid and sensitive to the temperature change at higher values.
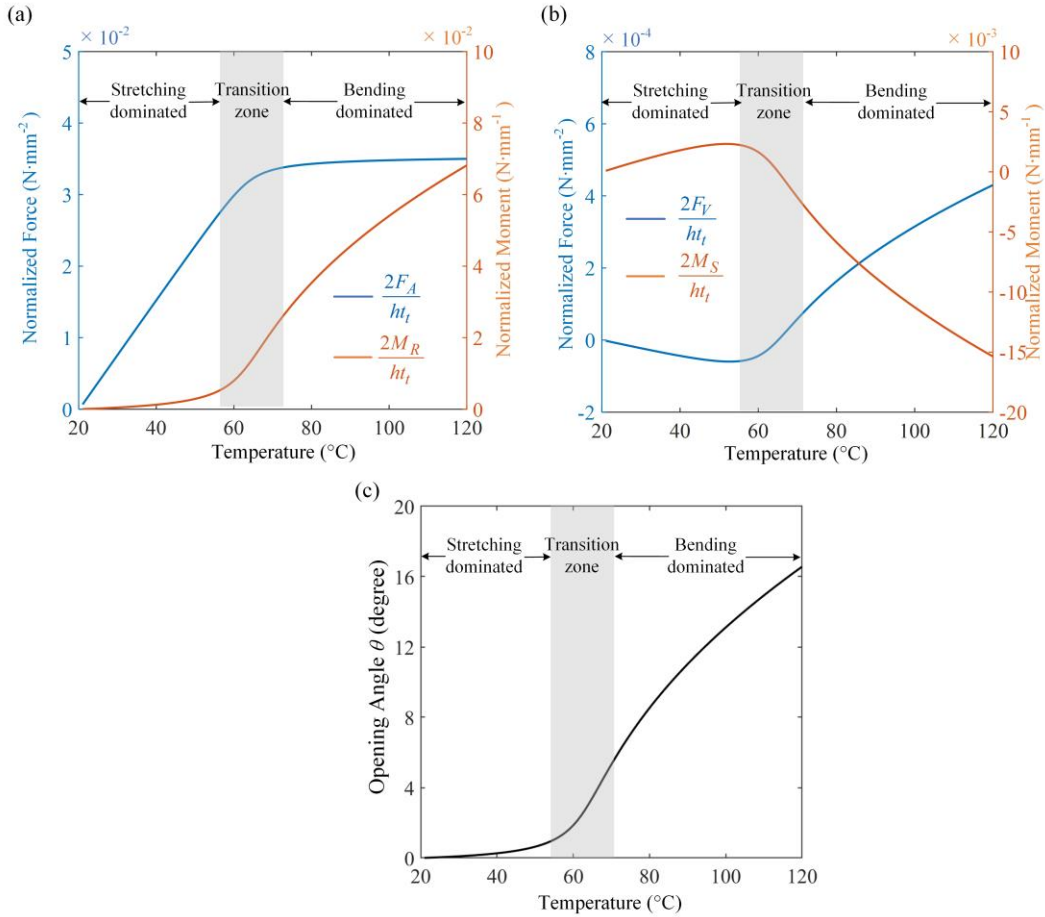


Supplementary Fig. S7: (a) and (b) Evolution of the normalized $F_A$, $M_R$, and $F_V$, $M_S$ as a function of temperature in the range 20 to 120 °C. (c) Opening angle $\theta$ as a function of temperature with slope showing R-BB sensitivity to a temperature change throughout the whole spectrum of temperature.

### S3-B. Experimental validation of BB theoretical models

To verify the validity of the solutions obtained from the previous theoretical analyses, we fabricated a number of building blocks with a specific set of geometric parameters and tested them in a heating chamber

(see S1 for details). A representative array of results from these experiments is shown in Supplementary Fig. S8 for both U-BB and R-BB. The experimentally measured values of $\Delta h/h$ and $\theta$ of actual BB geometry confirms the mechanism of deformations predicted through the mechanics theory on simplified column-beam analogs. In Supplementary Fig. S8, the experimental results show a good agreement with the theoretical prediction, especially in high temperature region (max error 15%). The discrepancy can be attributed to frictional dissipation and the simplified geometry assumed for the BB. In the low temperature regime, the former plays a major role, since the testing plate upon which the BB rests during the experiment is not perfectly smooth and hence the frictional force can significantly dominate the low magnitude of the internal forces generated in BB (Supplementary Fig. S7a and b). In the high temperature regime, on the other hand, the simplification of the semielliptical groove of BB core to a straight inclined beam is the main source of the deviation.
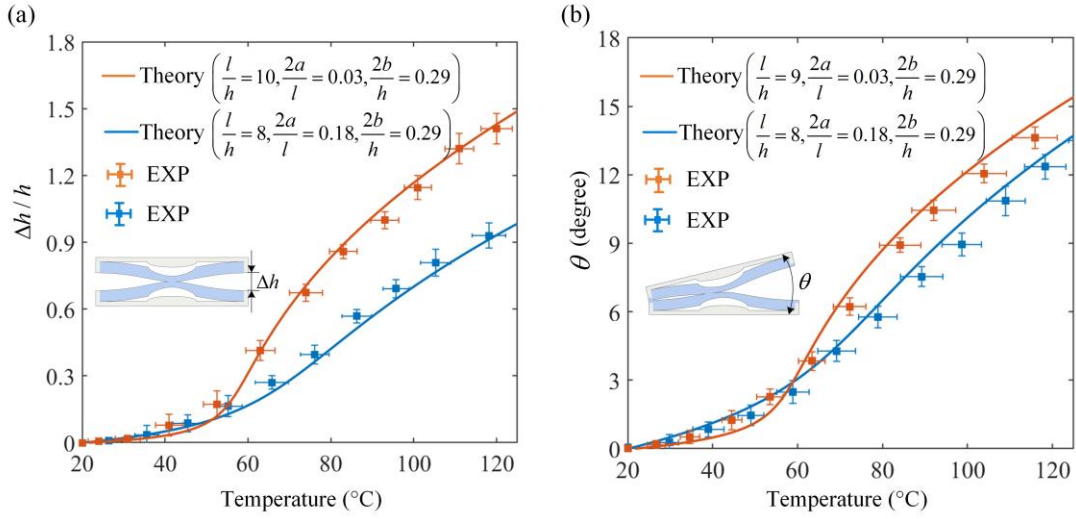


Supplementary Fig. S8: Experimental validation of theoretical predictions for both BBs: (a) normalized expansion $\Delta h/h$ versus temperature for U-BB tested with two representative sets of parameters (blue and red); (b) opening angle $\theta$ as a function of temperature for R-BB tested with two representative sets of parameters. Horizontal and vertical bars indicate the standard deviation around the mean from a pool of measures taken for both temperature and deformation, the former measured at three distinct sites in the heating camber, the latter obtained from three repeated measurements.

**S3-C. Computational analysis of BB response**

The theory presented in S3-A and experimentally validated in S3-B applies to a BB with core of small size ligament ($d<<l$) and groove geometry abridged with a straight axis. Here we relax these assumptions and examine a BB with actual (un-simplified) core geometry made of two distinct passive materials: silicone rubber and wood (see S2 for material properties). Section S3-C-i explains the method used to generate the deformation property capturing the role of the ligament size ($d/l$) besides the core size ($h/l$). Section S3-C-ii investigates the minor role of other geometric parameters defining U-BB and R-BB, in particular, the groove size, the core connection offset and the size of the end closure.

All the computational analyses here performed account for both material and geometric non-linearity of the constituents and are conducted by combining Python scripts and Abaqus (Dassault Systemes Simulia Corp, France). Eight-node, quadratic plane-stress elements (element type CPS8) are used to discretize the BB models and a mesh size equal to $b/4$ is adopted after performing a convergence analysis on the mesh size. The mechanical behavior of silicone rubber core is captured by a first order Ogden model. The effective properties of the wooden frame are assumed as transversely isotropic, and the values are obtained from experimental measures on dog-bone specimen of the solid material (see S2 for material properties). The cut motifs introduced into the computational models are represented with seam cracks along which duplicate element nodes overlap. A contact law with hard contact for the normal behavior, and frictionless for the tangential behavior, was assigned to the model.

**i. Deformation-property profile**

The deformation property profile in Fig.1a is generated through a response surface that fits a set of numerical predictions with model details given above. In general, the relationship between the response of a system ($y$) and a set of predictor variables ($x_1, x_2, \dots, x_k$) can be mathematically expressed as a multiple linear regression model which can be written as

$$y = \beta_0 + \beta_1 x_1 + \beta_2 x_2 + \cdots + \beta_k x_k + \varepsilon \tag{23}$$

where $y$ is the true response variable and the parameters $\beta_j$ ($j = 0, 1, \dots, k$), are the regression coefficients. This model spans a $k$-dimensional space defined by the regressor $\{x_j\}$. The parameter $\varepsilon$ is the error of the regression model.

To provide a continuous approximation of the true response, the material and geometry spaces of the deformation-property profile of BB are generated from two sets of simulations. These are conducted in the admissible domain of two sets of variables: ($E_f/E_c, \Delta\alpha$) and ($l/h, d/l$), and for each of them a response surface is obtained. In general, the response of an $N$-order model as a function of two variables, $x_1$ and $x_2$, is given by:

$$y = \sum_{I}^{N} \sum_{J=0}^{I} \beta_{I,J} x_1^J x_2^{I-J} + \varepsilon \qquad (24)$$

where $y$ is the true value of the response, in this case, $\Delta h/h$ for U-BB and $\theta$ for R-BB; $x_1$ and $x_2$ are $E_f/E_c$, $\Delta \alpha$ for the material space, and $l/h$, $d/l$ for the geometric space. If we let $\beta_{I,J} = \beta_{(I^2+3I-2J)/2}$, and $x_1^J x_2^{I-J} = x_{(I^2+3I-2J)/2}$, where indices $I$ and $J$ are integers satisfying $0 \le I + J \le N$ and $J \le I$, we can write Eqn. (24) in the general form of a multiple linear regression model as in Eqn. (23).

To estimate the regression coefficients $\beta_j$, we use the method of the least squares. Writing Eqn. (23) in matrix notation gives:

$$\boldsymbol{y} = \boldsymbol{X}\boldsymbol{\beta} + \boldsymbol{\varepsilon} \qquad (25)$$

where:

$$\boldsymbol{y} = \begin{bmatrix} y_1 \\ y_2 \\ \vdots \\ y_n \end{bmatrix}, \boldsymbol{X} = \begin{bmatrix} 1 & x_{11} & x_{12} & \cdots & x_{1k} \\ 1 & x_{21} & x_{22} & \cdots & x_{2k} \\ \vdots & \vdots & & & \vdots \\ 1 & x_{n1} & x_{n2} & \cdots & x_{nk} \end{bmatrix}, \boldsymbol{\beta} = \begin{bmatrix} \beta_1 \\ \beta_2 \\ \vdots \\ \beta_k \end{bmatrix}, and\ \boldsymbol{\varepsilon} = \begin{bmatrix} \varepsilon_1 \\ \varepsilon_2 \\ \vdots \\ \varepsilon_n \end{bmatrix} \qquad (26)$$

where the index $n$ represents the number of sampling points in the design of experiments.

Since the goal is to find the regression coefficient vector $\boldsymbol{\beta}$ that minimizes the error vector $\boldsymbol{\varepsilon}$, we can write the set of least squares function as:

$$L = \sum_{i=1}^{n} \varepsilon_i^2 = \boldsymbol{\varepsilon}^T \boldsymbol{\varepsilon} = (\boldsymbol{y} - \boldsymbol{X}\boldsymbol{\beta})^T (\boldsymbol{y} - \boldsymbol{X}\boldsymbol{\beta}) \qquad (27)$$

Eqn. (27) can be further developed into:

$$L = \boldsymbol{y}^T \boldsymbol{y} - 2\boldsymbol{\beta}^T \boldsymbol{X}^T \boldsymbol{y} + \boldsymbol{\beta}^T \boldsymbol{X}^T \boldsymbol{X} \boldsymbol{\beta} \qquad (28)$$

with the least-squares estimators $b_0, b_1, \dots, b_k$ satisfying the condition:

$$\left. \frac{\partial L}{\partial \boldsymbol{\beta}} \right|_{\boldsymbol{b}} = -2\boldsymbol{X}^T \boldsymbol{y} + 2\boldsymbol{X}^T \boldsymbol{X} \boldsymbol{b} = \boldsymbol{0} \qquad (29)$$

Eqn. (29) simplifies to the normal equations in matrix form:

$$\boldsymbol{X}^T \boldsymbol{X} \boldsymbol{b} = \boldsymbol{X}^T \boldsymbol{y} \qquad (30)$$

Solving the normal equations gives the least-squares estimator $\boldsymbol{b}$ of the regression coefficients $\boldsymbol{\beta}$:

$$\boldsymbol{b} = (\boldsymbol{X}^T \boldsymbol{X})^{-1} \boldsymbol{X}^T \boldsymbol{y} \qquad (31)$$

Hence, the fitted regression model is:

$$\hat{\boldsymbol{y}} = \boldsymbol{X}\boldsymbol{b} \qquad (32)$$

The residuals are:

$$\boldsymbol{e} = \boldsymbol{y} - \hat{\boldsymbol{y}} \qquad (33)$$

The coefficient of determination is:

$$R^2 = \frac{SS_R}{SS_T} = 1 - \frac{SS_E}{SS_T} \tag{34}$$

From the above we can respectively write the sum of squares of the regression $SS_R$, the sum of squares of the residual $SS_E$, and the total sum of squares as:

$$SS_R = \boldsymbol{b}^\mathrm{T}\boldsymbol{X}^\mathrm{T}\boldsymbol{y} - \frac{\left(\sum_{i=1}^n y_i\right)}{n} \tag{35}$$

$$SS_E = \boldsymbol{e}^\mathrm{T}\boldsymbol{e} = \boldsymbol{y}^\mathrm{T}\boldsymbol{y} - \boldsymbol{b}^\mathrm{T}\boldsymbol{X}^\mathrm{T}\boldsymbol{y} \tag{36}$$

$$SS_T = SS_R + SS_E \tag{37}$$

To reduce the error of the approximation, we aim at ensuring the coefficient of determination, $R^2$, above 0.99, a value that indicates here an acceptable level of accuracy. As per choice of the order of the response surface function (Eqn. (24)), we adopt $N = 4$ after performing a systematic analysis on the role of $N$.

While Fig.1a shows the response surface of $\Delta h/h$ for U-BB, i.e. the property-deformation profile, here we report, as example, the expression of the surface response of $\theta$ for R-BB in its geometric space:

$$\theta = \sum_{I}^{4} \sum_{J=0}^{I} c_{I,J} \left(\frac{l}{h}\right)^J \left(\frac{d}{l}\right)^{I-J} \tag{38}$$

where the regression coefficients $c_{I,J}$ is estimated through Eqn. (31). A similar approximation can be expressed in the complementary material space for R-BB as a function of the pair of material properties $(E_f/E_c, \Delta\alpha)$. Below are two plots constituting the property-deformation profile of R-BB response at $T = 120\,°\mathrm{C}$ (Supplementary Fig. S9a and b). Obtained through Eqn. (38), the spectra provide the range of rotational deformation that a BB can achieve through tuning the most influential geometric and material attributes that control R-BB response to temperature. The maps provide guidelines for attributes selection of BB, in particular, the geometric space on the right-hand side is the foundation of our morphing scheme.
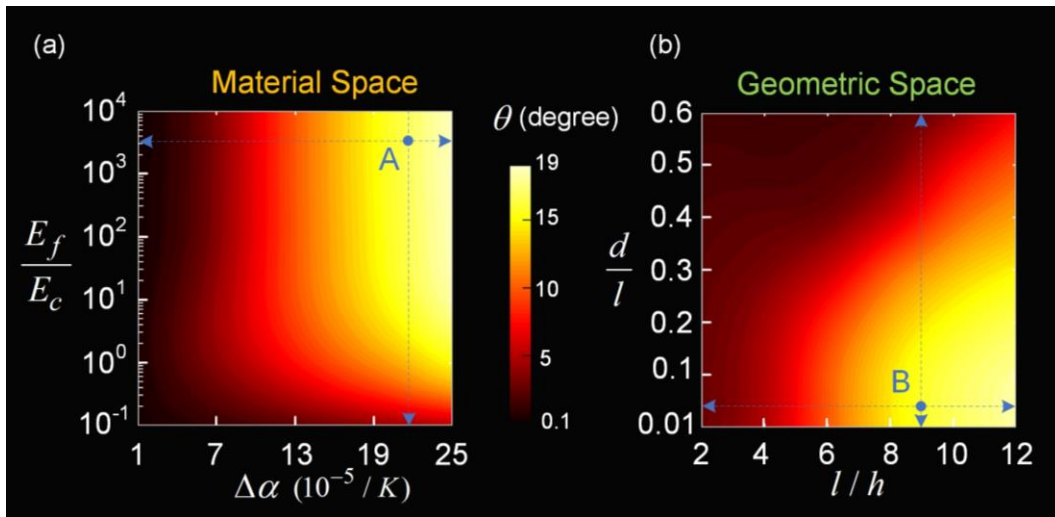


Supplementary Fig. S9: Property-deformation profile of R-BB

### ii.Sensitivity to least influential geometric parameters

#### a.Role of groove size ($a/l$ and $b/h$) in U-BB

While the surface response in Fig.1 shows the role of the most influential geometric parameters, $l/h$ and $d/l$, on $\Delta h/h$, Supplementary Fig. S10 reports complementary results capturing the influence of the semielliptical groove of the core: $(2a/l)$ and $(2b/h)$. For a BB with $l/h$ equal to 9, the curves show a minor role of $2a/l$ and $2b/h$ in the high temperature regime. On the other hand, in the transition zone, i.e. mid-range temperature, more notable differences appear in the shape of the response curve. In particular, for low values of $2a/l$ and $2b/h$, e.g. 0.02, the curves resemble those obtained through theory with the appearance of two regimes of deformation. On the other hand, for larger size of the groove, e.g. 2a/$l$=0.4 or $2b/h$=0.4, no transition zone can be observed; here U-BB steadily expands with temperature through a combination of bending and stretching generated in its members.
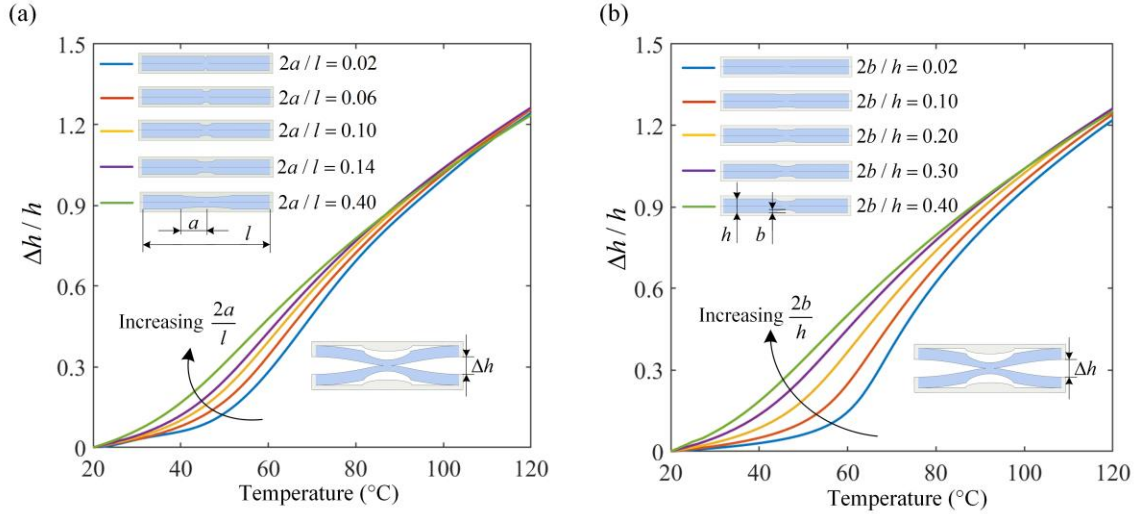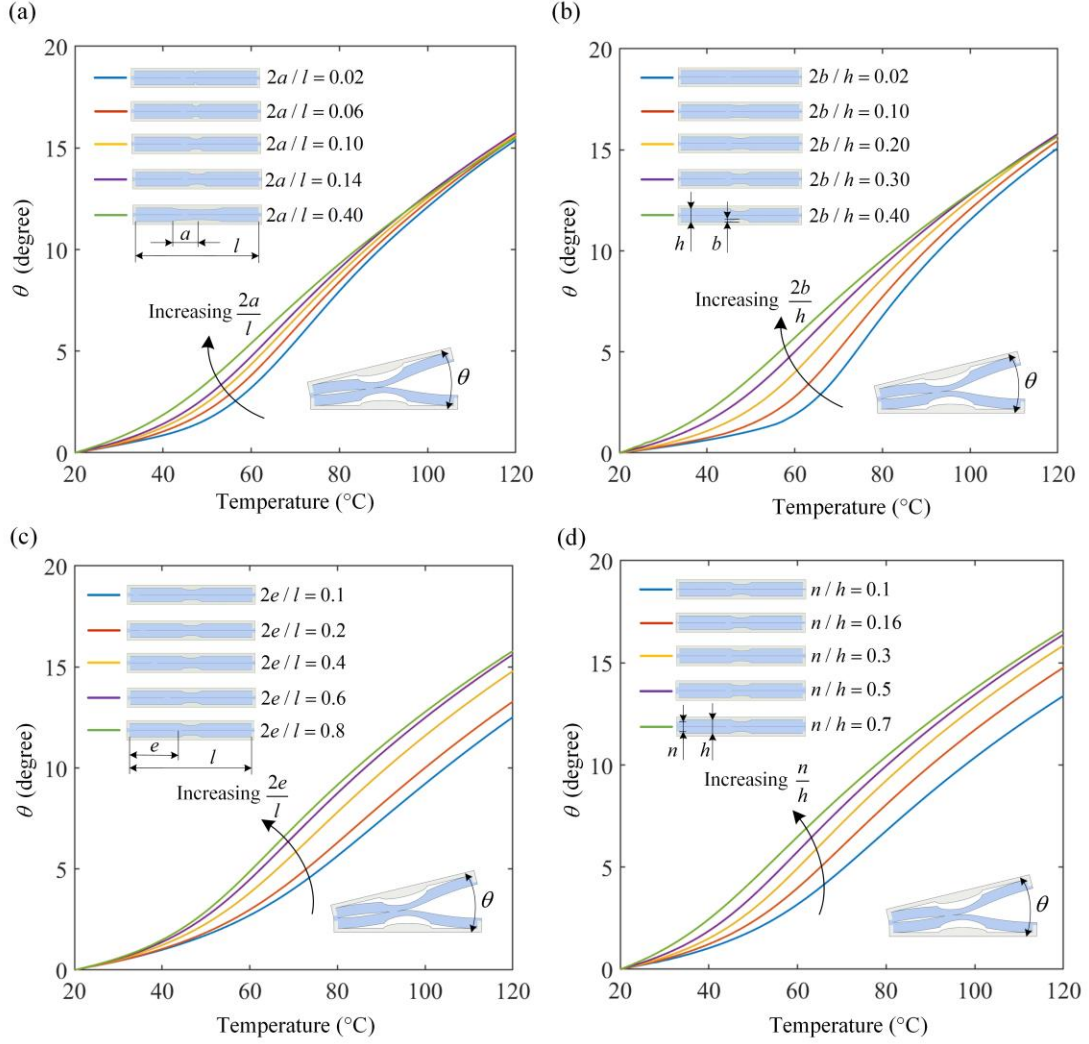


Supplementary Fig. S10: Normalized expansion of U-BB for a set of varying parameters of the semielliptical groove: (a) major axis: $2a/l$=0.02, 0.06, 0.1, 0.14, 0.4; (b) minor axis $2b/h$ =0.02, 0.1, 0.2, 0.3, 0.4.

#### b.Role of core connection offset, and end closure size in R-BB

Similarly, Supplementary Fig. S11a and b show $\theta$ for varying values of $(2a/l)$ and $(2b/h)$, for a BB with $l/h$ equal to 9. In addition, for R-BB, we investigate the role of the connection offset, $e$, and the size of the end closure $n$.

Supplementary Fig. S11c and d show that the opening angle increases with the $2e/l$ and $n/h$. Compared to $l/h$ or $d/l$, however, their effect is minor, and thus the tunability they would offer to tailor R-BB

response is narrow. To maximize BB response tunability, the values of the BB parameters chosen in this work are: $2a/l = 10/63, \; 2b/l = 2/7, \; 2e/l = 4/5, \; n/h = 2/7$.



Supplementary Fig. S11: Opening angle $\theta$ of R-BB for a set of varying parameters: (a) major axis: $2a/l$=0.02, 0.06, 0.1, 0.14, 0.4; (b) minor axis $2b/h$ =0.02, 0.1, 0.2, 0.3, 0.4; (c) $2e/l$=0.1, 0.2, 0.4, 0.6, 0.8; (d) $n/h$=0.1, 0.16, 0.3, 0.5, 0.7.

## S4. Investigation on stress state and bond strength of silicone-wood interface

Supplementary Fig. S12a shows that the constituent materials after the curing process bond at four sites, thus creating four silicone/wood interfaces. It is at these locations that the BB can potentially become weak during deformation. Here we analyze the stress state of their interfaces resulting from an increase of temperature and then measure the bonding strength through a set of pull-out tests.

Section S3-A provides a full analysis of both the temperature-driven deformation and the internal forces generated in a given BB. The results show the existence of an axial compressive force $F_R$ and a bending moment $M_R$ that act on the bonding interface (Supplementary Fig. S12a). At each of these edges, the distribution of the normal stresses can be simply described as:

$$\sigma(y, T) = -\frac{M_R(T)}{I}y - \frac{F_R(T)}{A} \tag{39}$$

where $\sigma$ is the normal stress exerted by the core to the surrounding low CTE frame, $y \in [-h/4, \ h/4]$, and $T$ is a given temperature. A positive value of $\sigma$ represents a tensile stress, whereas the negative counterpart indicates compression. $A$ and $I$ are the area and second moment of area of the cross-section. From Eqn. (39), we gather that the lower half of the cross-section ($y \in [-h/4, 0]$) is subject to either compressive or tensile stress, depending on the magnitude of $M_R$ and $F_R$, which is governed by temperature. Only the tensile portion can lead to interfacial debonding, which is controlled by the maximum tensile stress that occurs at the furthest edge ($y = -h/4$) of the cross-section. This critical value varies with the BB core size. Supplementary Fig. S12b-II shows how the normal stress at $y = -h/4$ evolves with temperature and the aspect ratio ($l/h$) of the BB core. The green area indicates a negative value of $\sigma(y = -h/4)$, meaning the transversal section of the interface is entirely compressed (Supplementary Fig. S12b-I). On the other hand, the orange points to a regime with positive values, which correspond to the distribution of $\sigma(y = -h/4)$ shown in Supplementary Fig. S12b-III. Only in this regime, debonding may occur, once the normal tensile stress at $y = -h/4$ reaches a critical value above the strength of the bonded interface.

To determine the strength of the bonding interface, we conducted a set of uniaxial tensile tests on six specimens fabricated with the process described in Fig.2. Specimens were extracted from a representative sample with geometry emphasizing the wood/silicone interface, i.e. a critical portion of one unit with two beams of rubber bonded to a layer of wood (Supplementary Fig. S12c-I). The bonding strength was assessed through a set of pull-out tests (Supplementary Fig. S12c-II). The tensile force was applied until the appearance of interfacial debonding, a point identified in red in the force-displacement curve of Supplementary Fig. S12c-IV. From the value of the ultimate force at this point, the bonding strength was calculated as $0.65 \pm 0.09$ MPa, a value that is an order of magnitude higher than the critical values that tensile stress can assume in the tensile regime (orange in Supplementary Fig. S12b-II). From this investigation, we can assert that the stress state at the silicone-wood interface is either compression or tension depending on temperature. While the former cannot but contribute to amplify the bonding of silicone rubber to wood, the latter can reach only values that are much lower than the bonding strength, hence providing almost no likelihood of detachment under the conditions and temperature reported in this investigation.
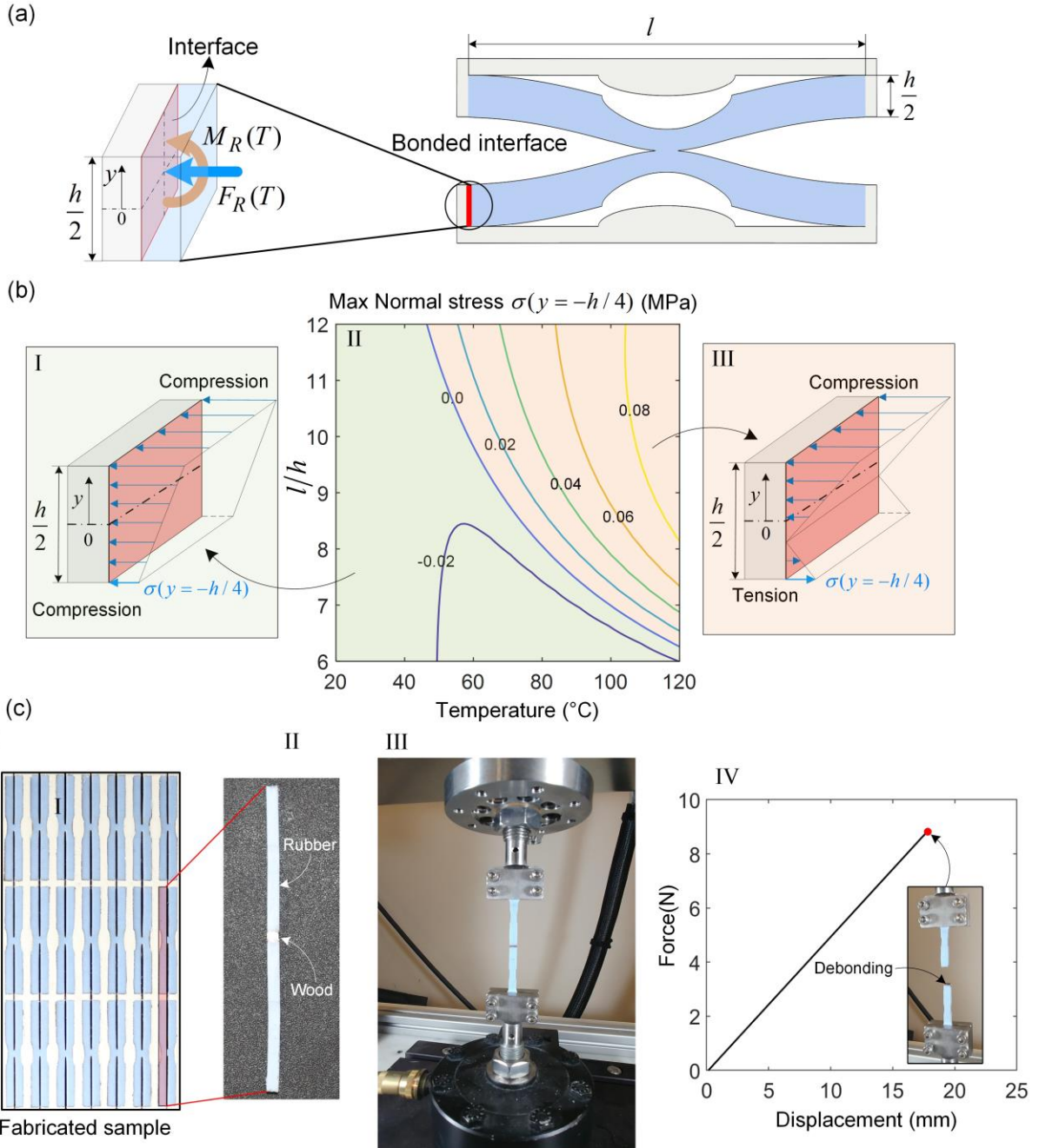
Supplementary Fig. S12: (a) Internal forces triggered by an increase of temperature at the bonding interface sites of BB. (b) Normal stress $\sigma$ at $y = -h/4$ as a function of temperature $T$ and length-to-width ratio of the BB core $l/h$. (c) Pull-out test and force-displacement response of a representative specimen.

## S5. Time response upon heating

As described in S3-A, the deformation of the BB is caused by a mere mismatch of thermal expansion of the constituent materials. The materials do not undergo any atomic or molecular changes, as in the case of smart materials, such as shape memory polymers. On the other hand, the deformation of our BB is determined by the topological layout and the internal forces that are generated in the BB members, with magnitude dependent on temperature. Once the BB has reached the target temperature, the deformation is instantaneous, as opposed to the time response observed in smart materials. With our metamaterials, the only time span involved is that required to heat the sample to the target temperature, which depends only on the heating strategy and the experimental setup.

Our analysis here, therefore, pertains to our experimental system (see S1), which consisted of a heating chamber with multiple thermocouples monitoring the maintenance of 120 °C, our target temperature. We conducted a series of tests on a BB placed in the middle of the chamber already heated at 120 °C and we recorded with a digital camera (EOS Rebel T6i, Canon USA) the time span required for the BB to deform. Two medium types were examined: fan-propelled air and oil bath, the former requiring 300±17 seconds to complete the deformation, and the latter 115±18 seconds.

To corroborate our experimental observations, a numerical analysis of the transient heat was performed with the following values assigned to the thermal conductivity, $K$, and specific heat, $c$, of the constituents: $K_{rubber} = 0.2\,W/(m \cdot K)$ , $c_{rubber} = 1100\,J/(kg \cdot K)$ , and $K_{wood} = 0.1\,W/(m \cdot K)$ , $c_{wood} = 1600\,J/(kg \cdot K)$. Due to symmetry, half BB was modelled in three dimensions (Supplementary Fig. S13a) with size identical to the fabricated BB and discretized with 20-node quadratic heat transfer bricks (DC3D20 element) in Abaqus (Dassault Systemes Simulia Corp, France). The following convective conditions were applied to the external surfaces of the model:

$$q = h_c(T_f - T) \tag{40}$$

where $q$ and $h_c$ are respectively the heat flux per second and the heat convection coefficient. $T$ denotes the surface temperature, with initial value set to 20 °C, and $T_f$ represents the temperature of the surrounding medium, assumed here as 120 °C. Because the heat convection coefficient $h_c$ cannot be accurately extracted from our in-house heating chamber, we appraised the upper and lower bound of the time span that would result from values of the heat convection $h_c$ falling within practical ranges. For natural convection in oil, the $h_c$ range was 50 - 200 W/$(m^2 K)$, and for the fan-propelled air heating (force convection with low speed air over surface), it was 10 - 40 W/$(m^2 K)$.

Supplementary Fig. S13b and c show the time variation of the interior temperature within the silicone rubber core for a BB immersed respectively in air and oil at 120 °C. A rapid increase can be observed until the thermal equilibrium is reached, a state indicated by the start of the plateau with corresponding time

representing the BB response. In air, the response is within the range 180 to 660 seconds, whereas in oil it is 56 to 160 seconds. These ranges are aligned with the values obtained from the experiments.
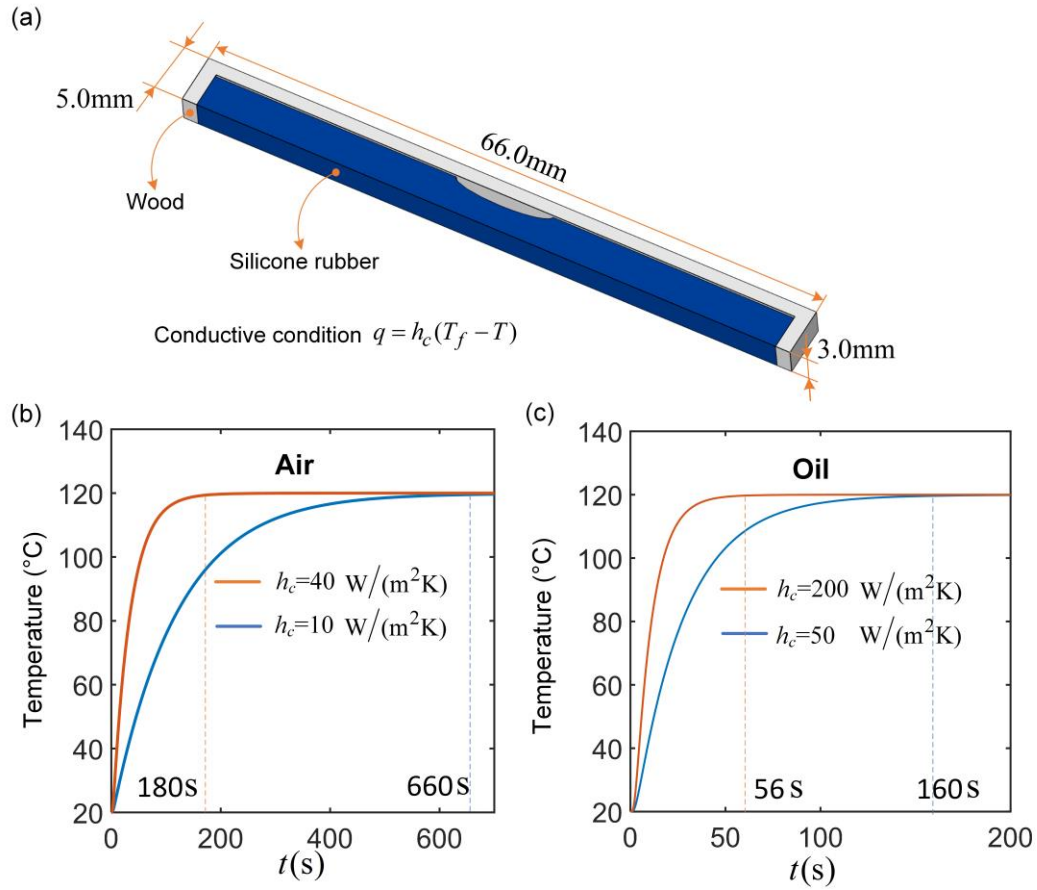


Supplementary Fig. S13: (a) Numeric results from transient heat transfer. (b) Interior temperature of BB as a function of time for BB in fan-propelled air conditions. (c) Interior temperature of BB as a function of time for BB immersed in oil bath.

## S6. Morphing from a pre-assigned sequence of building blocks

S3 has examined the response of an individual BB through theory and numerical analysis. Here we focus on a monolithic assembly of BBs, each with its own set of geometric attributes. The goal is to express the collective deformation of the metamaterial phenotype at a given $T$. As a paradigmatic example, we consider a series of $m$ rotational units sharing low CTE edges and all having equal width $l_i$. Supplementary Fig. S14 shows its deformed configuration, the phenotype at a given $T$. The central curve (dash type) is specified as representative of the deflected axis, and assumed as an arc spline consisting of a number of $G^1$ continuous arcs and straight segments, all passing through the interface mid-points, $P_i$, between adjacent units and normal to their contiguous edges.
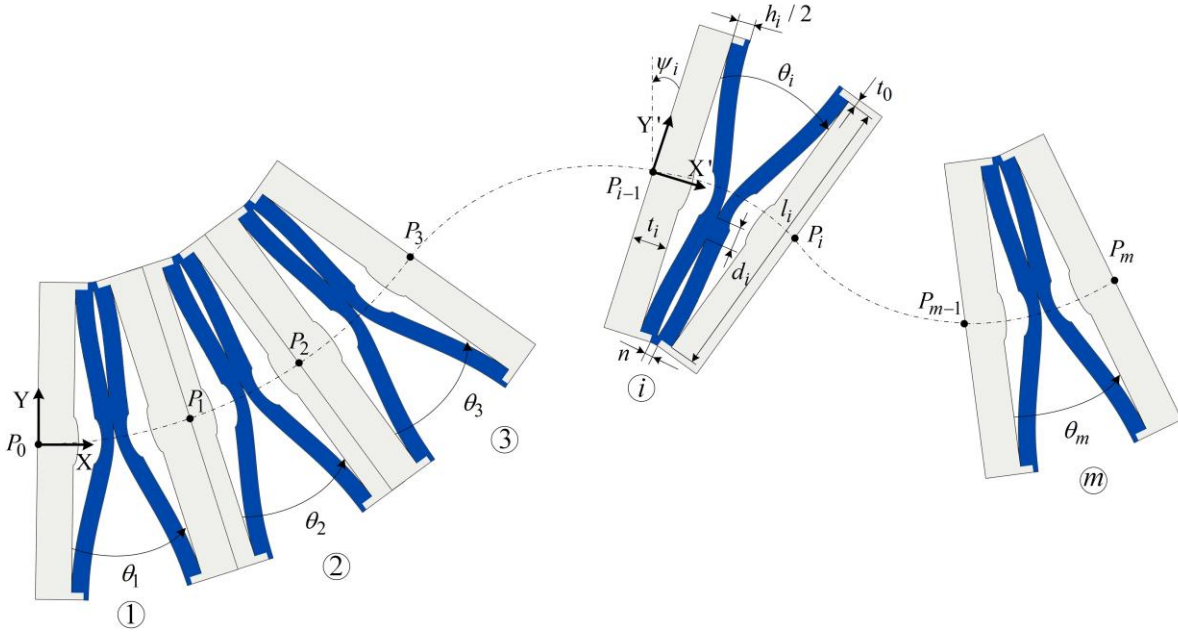


Supplementary Fig. S14: Schematic of a chain of $m$ building blocks in series, with an arc connecting a pair of consecutive mid-points $P_i$ at the BB interface. The local coordinate system (X′Y′) of a generic unit $i$ is referenced to the global system (XY) on the first outer frame of the first unit.

With reference to the generic building block $i$, we express the coordinates of its point $P_i$ in the local coordinate system, indicated as the X′Y′ plane, and in the global system residing at $P_0$ and visualized as the XY plane in the first unit. The two systems are rotated by $\psi_i$ and translated by a vector pointing from point $P_o$ to $P_{i-1}$. The coordinates of $P_i$ in the X′Y′ plane can be represented by the two-dimensional array:

$$\boldsymbol{p}'_i = \begin{bmatrix} x'_{p_i} \\ y'_{p_i} \end{bmatrix} = \begin{bmatrix} \cos(\theta_i/2)L_i \\ -\sin(\theta_i/2)L_i \end{bmatrix} \tag{41}$$

where the integer $i \in [1, m]$ and the expression of $L_i$, which is the distance between two consecutive mid-points of the low CTE edges, is given by:

$$L_i = (h_i - n + 2t_i)\cos(\theta_i/2) + (l_i + 2t_0)\sin(|\theta_i|/2) + n \tag{42}$$

where $h_i, l_i, t_i, d_i$ are the main geometric parameters controlling the R-BB response, and $n, t_0$ are minor parameters here assumed unchanging for all the units due to their minor influence (Supplementary Fig. S11). $\theta_i$ represents the opening angle of building block $i$, whose value is governed by $l_i/h_i$ and $d_i/l_i$, as illustrated in (Supplementary Fig. S9b). A positive value of $\theta_i$ represents a clockwise rotation, and negative means counter-clockwise.

The following affine transformation can be used to express $P_i$ in the global coordinate system (XY):

$$\boldsymbol{p}_i = \boldsymbol{M}_i \boldsymbol{p}'_i + \boldsymbol{v}_i \tag{43}$$

where the array $\boldsymbol{p}_i$ represents the coordinates of $P_i$ in the global coordinates system. $\boldsymbol{v}_i$ denotes the translation vector pointing from point $P_o$ to $P_{i-1}$; the matrix $\boldsymbol{M}_i$ defines the relative rotation of the coordinate systems by the angle $\psi_i$, and are given by:

$$\boldsymbol{M}_i = \begin{bmatrix} \cos\psi_i & -\sin\psi_i \\ \sin\psi_i & \cos\psi_i \end{bmatrix}, \qquad \boldsymbol{v}_i = \boldsymbol{p}_{i-1} - \boldsymbol{p}_0 \tag{44}$$

If the origin of the global coordinate system is $P_0$ with coordinates $x_{p_0} = y_{p_0} = 0$, the rotation of the unit $i$ with respect to the global system (XY) is the mere aggregation of the opening angle $\theta$ of the preceding units $(i - 1)$ (see Supplementary Fig. S14), thus expressed as

$$\psi_i = \sum_{j=0}^{i-1} \theta_j \tag{45}$$

where $\theta_0$ is null. As assumed above, the central axis of the deformed configuration of the BB assembly can be represented by a $G^1$ continuous arc spline passing through all the mid-points $P_i$. The expression of a generic arc $i$ in the arc spline can be expressed from point $P_{i-1}$ and to point $P_i$, as:

$$F_i(x, y) = (x - A_i)^2 + (y - B_i) - R_i^2 = 0, \qquad \begin{matrix} x_{p_{i-1}} \le x \le x_{p_i} \\ y_{p_{i-1}} \le y \le y_{p_i} \end{matrix} \tag{46}$$

with $R_i$ being the radius, and $(A_i, B_i)$ the coordinates of the arc center, whose expressions are:

$$R_i = \frac{L_i}{2\sin(|\theta_i|/2)}, \quad A_i = -\frac{L_i \sin\psi_i}{2\sin(\theta_i/2)} + x_{p_{i-1}}, \quad B_i = -\frac{L_i \cos\psi_i}{2\sin(\theta_i/2)} + y_{p_{i-1}} \tag{47}$$

## S7. Morphing on-target through encoded sequence of building blocks

Morphing on target poses the search of a BB sequence that allows the metamaterial phenotype to accurately conform to a target domain. We describe here the target as a domain with central axis representable with an arc spline and two symmetric boundaries that are continuous with varying distance along the central axis. Both are shown in blue on the upper part of Supplementary Fig. S15, the former in dash-dot and the latter with solid line. In red, at the lower part of the figure, is a metamaterial phenotype with randomly assigned BB sequence expressed at a given temperature.
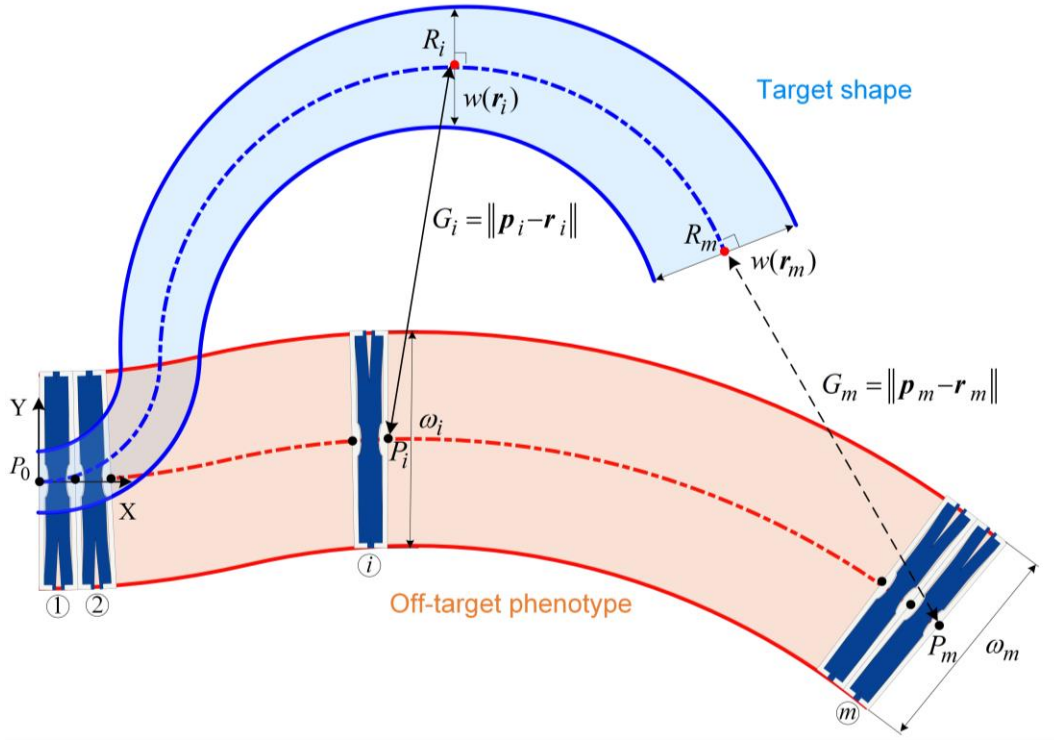


Supplementary Fig. S15: Target domain (blue - top) with varying width and off-target metamaterial phenotype (red - below), both sharing the initial location where the global coordinate system is anchored.

## S7-A. Description of target shape

The central axis of the target shape is here assumed to trace an arc spline mathematically expressed piece-wisely in an implicit form as:

$$f = f(x, y) = \begin{cases} f_1(x, y) = 0, & \text{if } 0 \leq x < x_1 & 0 \leq y < y_1 \\ f_2(x, y) = 0, & \text{if } x_1 \leq x < x_2 & y_1 \leq y < y_2 \\ \quad \dots \\ f_q(x, y) = 0, & \text{if } x_{q-1} \leq x \leq x_q & y_{q-1} \leq y \leq y_q \end{cases} \quad (48)$$

26

where $q$ denotes the number of arcs and straight lines, and the intervals are the coordinates of the blending points.

For the symmetric boundaries of the target shape, the function describing the width change along the central axis is expressed as:

$$w = w(x, y) \tag{49}$$

### S7-B. Problem formulation

The phenotype will match the target shape if two conditions are guaranteed. The first pertains to the central axis of the metamaterial phenotype. For a given temperature, a generic phenotype with randomly assigned BB sequence will most likely be off-target, i.e. its central axis would appear far from that of the target. This gap from the target (Supplementary Fig. S15) can be mathematically expressed for each building block as

$$G_i = \sqrt{\left[(x_{p_i} - x_{r_i})^2 + (y_{p_i} - y_{r_i})^2\right]} = \|\boldsymbol{p}_i - \boldsymbol{r}_i\| \tag{50}$$

where $(x_{p_i}, y_{p_i})$ are the coordinates of the interface mid-point $P_i$ of BB $i$ in the off-target phenotype, and $(x_{r_i}, y_{r_i})$ are those of the respective point $R_i$ on the target axis; $\boldsymbol{p}_i$ and $\boldsymbol{r}_i = \left[x_{r_i}, y_{r_i}\right]^{\mathrm{T}}$ denote the position vectors of $P_i$ and $R_i$ in the global coordinate system.

The second condition relates to the boundary of the target domain. Again here, an arbitrary string of BBs will likely lead to a phenotype with non-conforming boundaries, i.e. incompatible from those of the target (Supplementary Fig. S15). We thus express the gap between the width of each BB and the width of the boundary at a given position as:

$$W_i = \left|\omega_i - w(x_{r_i}, y_{r_i})\right| = |\omega_i - w(\boldsymbol{r}_i)| \tag{51}$$

where $\omega_i = l_i + 2t_0$ is the width for $BB_i$ in the off-target phenotype, and $w(x_{r_i}, y_{r_i})$ is the width of the target shape corresponding to point $R_i$.

In general, the characteristic distances of an off-target phenotype from the target domain, i.e. Eqns. (50) and (51), should be both minimized simultaneously. This can be expressed through a least-squares model that minimizes the sum of the squares of both residuals. In this case, the overall objective function can be formulated as:

$$F = \sum_{i=1}^{m}\left(G_i^2 + W_i^2\right) = \sum_{i=1}^{m}[\|\boldsymbol{p}_i - \boldsymbol{r}_i\|^2 + |\omega_i - w(\boldsymbol{r}_i)|^2] \tag{52}$$

### S7-C. Design variables

Supplementary Fig. S14 shows the internal parameters describing the BB architecture: $h_i, t_i, l_i, d_i, n, t_0$. The first four are treated as variables, whereas $n$ and $t_0$ are assumed constant because (as S3-C

demonstrates) the BB response is less sensitive to changes in their value. We can thus collect the most influential descriptors of the BB geometry in the following vector of variables:

$$\boldsymbol{X} = \{h_i, t_i, l_i, d_i\}^{\mathrm{T}} \quad (i = 1,2,..m) \tag{53}$$

### S7-D. Design constraints

To achieve the kinematic compatibility between neighbouring units, the edge of each building block $i$ should be normal to the tangent direction of the target axis, an arc spline, on point $R_i$. These constraints can be mathematically expressed by the system of equalities:

$$g_i = \boldsymbol{n}_i^{\mathrm{T}} \cdot \boldsymbol{u}_i = 0 \quad (i = 1,2, \dots, m) \tag{54}$$

where $\boldsymbol{n}_i$ denotes the normal vector of the target curve on point $R_i$, expressed as:

$$\boldsymbol{n}_i = \left[ \partial f(x_{r_i}, y_{r_i})/\partial x, \ \partial f(x_{r_i}, y_{r_i})/\partial y \right]^{\mathrm{T}} \tag{55}$$

with $\partial f/\partial x$ and $\partial f/\partial y$ representing partial derivatives of the target arc spline; $(x_{r_i}, y_{r_i})$ denote the coordinates of point $R_i$ in the global coordinate system. $\boldsymbol{u}_i$ is a vector in the $X$ axis direction of the localized coordinate system residing at point $P_{i-1}$, and it can be obtained from the following transformation:

$$\boldsymbol{u}_i = \boldsymbol{M}_i \boldsymbol{u}_i' \tag{56}$$

The unit vector $\boldsymbol{u}_i'$ is expressed as $[1,0]^{\mathrm{T}}$ in the local coordinate system and the matrix $\boldsymbol{M}_i$ (Eqn. (44)) defines the relative rotation.

The opening angle $\theta_i$ for each R-BB is governed by both $l_i/h_i$ and $d_i/l_i$, and Supplementary Fig. S9b presents the maximum range of $\theta_i$ that R-BB can generate in the geometric space. To produce admissible deformation, the following constraints should not be violated:

$$\underline{g}_i^{l/h} = R_{l/h}^L - l_i/h_i \leq 0 \tag{57}$$

$$\overline{g}_i^{l/h} = l_i/h_i - R_{l/h}^U \leq 0 \tag{58}$$

$$\underline{g}_i^{d/l} = R_{d/l}^L - d_i/l_i \leq 0 \tag{59}$$

$$\overline{g}_i^{d/l} = d_i/l_i - R_{d/l}^U \leq 0 \tag{60}$$

where $R_{l/h}^L$ and $R_{l/h}^U$ are the lower and upper bounds on the ratio of $l_i/h_i$, respectively, and $R_{d/l}^L$ and $R_{d/l}^U$ are lower and upper bounds on $d_i/l_i$.

For practical considerations, side constraints are also set for each design variable, i.e. $h_i^L \leq h_i \leq h_i^U, t_i^L \leq t_i \leq t_i^U, l_i^L \leq l_i \leq l_i^U, d_i^L \leq d_i \leq d_i^U$, where the superscripts $L$ and $U$ represent the lower and upper bounds on the design variables, respectively.

## S7-E. Optimization problem formulation

The problem of morphing on-target is thus expressed as the minimization of the sum of the squares of both gaps (Eqns. (50) and (51)) subject to the following set of equality and inequality constraints:

$$
\begin{cases}
\min_{h_i,t_i,l_i,d_i} \quad F = \sum_{i=1}^m [\|\boldsymbol{p_i} - \boldsymbol{r_i}\|^2 + |\omega_i - w(\boldsymbol{r_i})|^2] \\
\quad \text{s. t.} \qquad\qquad\qquad g_i = 0, \\
\qquad\qquad\qquad\qquad \underline{g}_i^{l/h} \le 0, \\
\qquad\qquad\qquad\qquad \overline{g}_i^{l/h} \le 0, \\
\qquad\qquad\qquad\qquad \underline{g}_i^{d/l} \le 0, \\
\qquad\qquad\qquad\qquad \overline{g}_i^{d/l} \le 0, \\
\qquad\qquad\qquad h_i^L \le h_i \le h_i^U, \\
\qquad\qquad\qquad t_i^L \le t_i \le t_i^U, \\
\qquad\qquad\qquad l_i^L \le l_i \le l_i^U, \\
\qquad\qquad\qquad d_i^L \le d_i \le d_i^U, \qquad\quad i = 1,2,\dots,m.
\end{cases}
\tag{61}
$$

## S7-F. Sensitivity analysis

The derivatives of the objective function with respect to the design variables $h_j$, $t_j$, $l_j$ and $d_j$ $(j = 1,2,\dots,m)$ can be obtained through

$$
\frac{\partial F}{\partial h_j} = \sum_{i=1}^m \left[ \left(\frac{\partial \boldsymbol{p_i}}{\partial h_j}\right)^{\mathrm{T}} (\boldsymbol{p_i} - \boldsymbol{r_i}) + (\boldsymbol{p_i} - \boldsymbol{r_i})^{\mathrm{T}} \left(\frac{\partial \boldsymbol{p_i}}{\partial h_j}\right) \right]
\tag{62.a}
$$

$$
\frac{\partial F}{\partial t_j} = \sum_{i=1}^m \left[ \left(\frac{\partial \boldsymbol{p_i}}{\partial t_j}\right)^{\mathrm{T}} (\boldsymbol{p_i} - \boldsymbol{r_i}) + (\boldsymbol{p_i} - \boldsymbol{r_i})^{\mathrm{T}} \left(\frac{\partial \boldsymbol{p_i}}{\partial t_j}\right) \right]
\tag{62.b}
$$

$$
\frac{\partial F}{\partial l_j} = \sum_{i=1}^m \left[ \left(\frac{\partial \boldsymbol{p_i}}{\partial l_j}\right)^{\mathrm{T}} (\boldsymbol{p_i} - \boldsymbol{r_i}) + (\boldsymbol{p_i} - \boldsymbol{r_i})^{\mathrm{T}} \left(\frac{\partial \boldsymbol{p_i}}{\partial l_j}\right) \right] + 2\left(\omega_j - w(\boldsymbol{r_j})\right)
\tag{62.c}
$$

$$
\frac{\partial F}{\partial d_j} = \sum_{i=1}^m \left[ \left(\frac{\partial \boldsymbol{p_i}}{\partial d_j}\right)^{\mathrm{T}} (\boldsymbol{p_i} - \boldsymbol{r_i}) + (\boldsymbol{p_i} - \boldsymbol{r_i})^{\mathrm{T}} \left(\frac{\partial \boldsymbol{p_i}}{\partial d_j}\right) \right]
\tag{62.d}
$$

The partial derivatives of Eqn. (62) are

$$
\frac{\partial \boldsymbol{p_i}}{\partial h_j} =
\begin{cases}
\sum_{k=j+1}^i \frac{\partial \theta_j}{\partial h_j} \begin{bmatrix} -sin(\psi_k + \theta_k/2)L_k \\ cos(\psi_k + \theta_k/2)L_k \end{bmatrix} + \boldsymbol{M_j}\frac{\partial \boldsymbol{p'_j}}{\partial h_j}, & i > j \\
\boldsymbol{M_j}\frac{\partial \boldsymbol{p'_j}}{\partial h_j}, & i = j \\
\boldsymbol{0}, & i < j
\end{cases}
\tag{63.a}
$$

$$
\frac{\partial \boldsymbol{p_i}}{\partial t_j} =
\begin{cases}
\boldsymbol{M_j}\frac{\partial \boldsymbol{p'_j}}{\partial t_j}, & i \ge j \\
\boldsymbol{0}, & i < j
\end{cases}
\tag{63.b}
$$

$$\frac{\partial \boldsymbol{p_i}}{\partial l_j} = \begin{cases} \sum_{k=j+1}^{i} \frac{\partial \theta_j}{\partial l_j}\begin{bmatrix} -sin(\psi_k + \theta_k/2)L_k \\ cos(\psi_k + \theta_k/2)L_k \end{bmatrix} + \boldsymbol{M}_j \frac{\partial \boldsymbol{p'_j}}{\partial l_j}, & i > j \\ \boldsymbol{M}_j \frac{\partial \boldsymbol{p'_j}}{\partial l_j}, & i = j \\ \boldsymbol{0}, & i < j \end{cases} \tag{63.c}$$

$$\frac{\partial \boldsymbol{p_i}}{\partial d_j} = \begin{cases} \sum_{k=j+1}^{i} \frac{\partial \theta_j}{\partial d_j}\begin{bmatrix} -sin(\psi_k + \theta_k/2)L_k \\ cos(\psi_k + \theta_k/2)L_k \end{bmatrix} + \boldsymbol{M}_j \frac{\partial \boldsymbol{p'_j}}{\partial d_j}, & i > j \\ \boldsymbol{M}_j \frac{\partial \boldsymbol{p'_j}}{\partial d_j}, & i = j \\ \boldsymbol{0}, & i < j \end{cases} \tag{63.d}$$

where

$$\boldsymbol{M}_j \frac{\partial \boldsymbol{p'_j}}{\partial h_j} = \frac{1}{2}\begin{bmatrix} cos\psi_{j+1} & cos\psi_j & -sin\psi_{j+1} & -sin(\psi_j + \theta_j/2) \\ sin\psi_{j+1} & sin\psi_j & cos\psi_{j+1} & cos(\psi_j + \theta_j/2) \end{bmatrix}\begin{bmatrix} 1 + sgn(\theta_j)\omega_j \frac{\partial \theta_j}{\partial h_j} \\ 1 \\ (h_j - n + 2t_j)\frac{\partial \theta_j}{\partial h_j} \\ n\frac{\partial \theta_j}{\partial h_j} \end{bmatrix} \tag{64.a}$$

$$\boldsymbol{M}_j \frac{\partial \boldsymbol{p'_j}}{\partial t_j} = \begin{bmatrix} cos\psi_j + cos\psi_{j+1} \\ sin\psi_j + sin\psi_{j+1} \end{bmatrix} \tag{64.b}$$

$$\boldsymbol{M}_j \frac{\partial \boldsymbol{p'_j}}{\partial l_j} = \frac{1}{2}\begin{bmatrix} cos\psi_{j+1} & -sin\psi_j & -sin\psi_{j+1} & -sin(\psi_j + \theta_j/2) \\ sin\psi_{j+1} & cos\psi_j & cos\psi_{j+1} & cos(\psi_j + \theta_j/2) \end{bmatrix}\begin{bmatrix} sgn(\theta_j)\omega_j \frac{\partial \theta_j}{\partial l_j} \\ sgn(\theta_j) \\ (h_j - n + 2t_j)\frac{\partial \theta_j}{\partial l_j} - sgn(\theta_j) \\ n\frac{\partial \theta_j}{\partial l_j} \end{bmatrix} \tag{64.c}$$

$$\boldsymbol{M}_j \frac{\partial \boldsymbol{p'_j}}{\partial d_j} = \frac{1}{2}\frac{\partial \theta_j}{\partial d_j}\begin{bmatrix} cos\psi_{j+1} & -sin\psi_j & -sin(\psi_j + \theta_j/2) \\ sin\psi_{j+1} & cos\psi_j & cos(\psi_j + \theta_j/2) \end{bmatrix}\begin{bmatrix} sgn(\theta_j)\omega_j \\ (h_j - n + 2t_j) \\ n \end{bmatrix} \tag{64.d}$$

$$\frac{\partial \theta_j}{\partial h_j} = \sum_I^N \sum_{J=0}^I -\frac{Jc_{I,J}}{h_j}\left(\frac{l_j}{h_j}\right)^J \left(\frac{d_j}{l_j}\right)^{I-J} \tag{64.e}$$

$$\frac{\partial \theta_j}{\partial l_j} = \sum_I^N \sum_{J=0}^I \frac{(2J-I)c_{I,J}}{l_j}\left(\frac{l_j}{h_j}\right)^J \left(\frac{d_j}{l_j}\right)^{I-J} \tag{64.f}$$

$$\frac{\partial \theta_j}{\partial d_j} = \sum_I^N \sum_{J=0}^I \frac{(I-J)c_{I,J}}{l_j}\left(\frac{l_j}{h_j}\right)^J \left(\frac{d_j}{l_j}\right)^{I-J-1} \tag{64.g}$$

The derivatives of the constraint in Eqn. (54) with respect to the design variables $h_j$, $t_j$, $l_j$ and $d_j$ ($j = 1,2, \ldots, m$) are given by

$$\frac{\partial g_i}{\partial h_j} = \begin{cases} \frac{\partial \theta_j}{\partial h_j}\left(-\frac{\partial f\left(x_{r_i}, y_{r_i}\right)}{\partial x}\sin\psi_i + \frac{\partial f\left(x_{r_i}, y_{r_i}\right)}{\partial y}\cos\psi_i\right), & i > j \\ 0, & i \leq j \end{cases} \tag{65.a}$$

$$\frac{\partial g_i}{\partial t_j} = 0 \tag{65.b}$$

$$\frac{\partial g_i}{\partial l_j} = \begin{cases} \frac{\partial \theta_j}{\partial l_j}\left(-\frac{\partial f\left(x_{r_i}, y_{r_i}\right)}{\partial x}\sin\psi_i + \frac{\partial f\left(x_{r_i}, y_{r_i}\right)}{\partial y}\cos\psi_i\right), & i > j \\ 0, & i \leq j \end{cases} \tag{65.c}$$

$$\frac{\partial g_i}{\partial d_j} = \begin{cases} \frac{\partial \theta_j}{\partial d_j}\left(-\frac{\partial f\left(x_{r_i}, y_{r_i}\right)}{\partial x}\sin\psi_i + \frac{\partial f\left(x_{r_i}, y_{r_i}\right)}{\partial y}\cos\psi_i\right), & i > j \\ 0, & i \leq j \end{cases} \tag{65.d}$$

where $\partial\theta_j/\partial h_j$, $\partial\theta_j/\partial l_j$ and $\partial\theta_j/\partial d_j$ are expressed in Eqns. (64.e), (64.f) and (64.g), respectively.

The derivatives of the constraints in Eqns. (57)-(60) are

$$\frac{\partial \underline{g}_i^{l/h}}{\partial h_j} = \begin{cases} l_j/h_j^2, & i = j \\ 0, & i \neq j \end{cases} \qquad \frac{\partial \underline{g}_i^{l/h}}{\partial l_j} = \begin{cases} -1/h_j, & i = j \\ 0, & i \neq j \end{cases} \qquad \frac{\partial \underline{g}_i^{l/h}}{\partial t_j} = \frac{\partial \underline{g}_i^{l/h}}{\partial d_j} = 0 \tag{66}$$

$$\frac{\partial \overline{g}_i^{l/h}}{\partial h_j} = \begin{cases} -l_j/h_j^2, & i = j \\ 0, & i \neq j \end{cases} \qquad \frac{\partial \overline{g}_i^{l/h}}{\partial l_j} = \begin{cases} 1/h_j, & i = j \\ 0, & i \neq j \end{cases} \qquad \frac{\partial \overline{g}_i^{l/h}}{\partial t_j} = \frac{\partial \overline{g}_i^{l/h}}{\partial d_j} = 0 \tag{67}$$

$$\frac{\partial \underline{g}_i^{d/l}}{\partial h_j} = \frac{\partial \underline{g}_i^{d/l}}{\partial t_j} = 0 \qquad \frac{\partial \underline{g}_i^{d/l}}{\partial l_j} = \begin{cases} d_j/l_j^2, & i = j \\ 0, & i \neq j \end{cases} \qquad \frac{\partial \underline{g}_i^{d/l}}{\partial d_j} = \begin{cases} -1/l_j, & i = j \\ 0, & i \neq j \end{cases} \tag{68}$$

$$\frac{\partial \overline{g}_i^{d/l}}{\partial h_j} = \frac{\partial \overline{g}_i^{d/l}}{\partial t_j} = 0 \qquad \frac{\partial \overline{g}_i^{d/l}}{\partial l_j} = \begin{cases} -d_j/l_j^2, & i = j \\ 0, & i \neq j \end{cases} \qquad \frac{\partial \overline{g}_i^{d/l}}{\partial d_j} = \begin{cases} 1/l_j, & i = j \\ 0, & i \neq j \end{cases} \tag{69}$$

After calculating the gradients above, Eqns. (62), and (65)-(69) are used to guide the search direction of the gradient-based optimization scheme described in the following section.

## S7-G. Optimization method

Eqn. (61) describes a nonlinear optimization problem with multiple equality and inequality constraints. To solve it, we opt for the Powell-Hestenes-Rockafellar (PHR) method[①], an Augmented Lagrangian algorithm well suited for minimization problems with equality and inequality constraints. The Lagrange function defined for the primal problem is reframed with the definition of a set of penalty functions, which

---

[①] Rockafellar, R. T. The multiplier method of Hestenes and Powell applied to convex programming. *Journal of Optimization Theory and applications* **12**, 555-562 (1973).

allow transforming the primal problem into a series of unconstrained sub-problems. The Augmented Lagrangian function corresponding to the primal problem in Eqns. (61) is constructed as:

$$\psi(\boldsymbol{X}, \boldsymbol{\mu}, \boldsymbol{\lambda}, \boldsymbol{\sigma}) = F - \sum_{i=1}^{m} \mu_i g_i + \frac{\sigma}{2} \sum_{i=1}^{m} g_i^2 + \frac{1}{2\sigma} \sum_{\iota=1}^{4m} ([\min\{0, -\sigma g_\iota^I - \lambda_\iota\}]^2 - \lambda_\iota^2) \qquad (70)$$

where $\boldsymbol{X}$ is a vector representing the design variables (Eqns. (53)), $\boldsymbol{\mu}$ and $\boldsymbol{\lambda}$ are the Lagrange multipliers, and $\boldsymbol{\sigma}$ the penalty multiplier; $g_\iota^I$ represents the $\iota$- $th$ inequality constraint, including $\underline{g}_i^{l/h}, \overline{g}_i^{l/h}, \underline{g}_i^{d/l}$, and $\overline{g}_i^{d/l}$. In the $k$- $th$ step of the iterative process for solving the primal problem, starting from the design point, $\boldsymbol{X}^k$, the design point for the $(k + 1)$-$th$ step is obtained by minimizing the following unconstrained sub-problem:

$$\min \ \psi(\boldsymbol{X}, \boldsymbol{\mu}^k, \boldsymbol{\lambda}^k, \sigma^k) \qquad (71)$$

To solve Eqn. (71), we resort to the Broyden-Fletcher-Goldfarb-Shanno (BFGS) method[1] that updates the design variables such that the updating scheme, in the $k_j$-$th$ step of the solution process of the sub-problem, is given by:

$$X_{m_j}^{k_j+1} = \begin{cases} X_{m_j}^L & \text{if } X_{m_j}^k - \beta^{k_j} d_{m_j}^k \leq X_{m_j}^L \\ X_{m_j}^k - \beta^{k_j} d_{m_j}^k & \text{if } X_{m_j}^L < X_{m_j}^k - \beta^{k_j} d_{m_j}^k \leq X_{m_j}^U \\ X_{m_j}^U & \text{if } X_{m_j}^U < X_{m_j}^k - \beta^{k_j} d_{m_j}^k \end{cases} \qquad (72)$$

where $X_{m_j}^{k_j}$ is the $m_j$-$th$ component in the design variable vector $\boldsymbol{X}^{k_j}$ $(m_j = 1,2, \dots, 4m)$, $\beta^{k_j}$ is the step size in the $k_j$-$th$ step, $X_{m_j}^L$ and $X_{m_j}^U$ are the lower and upper bounds on the design variable $X_{m_j}^{k_j}$, respectively, and $d_{m_j}^{k_j}$ is the $m_j$-$th$ component in the search direction $\boldsymbol{d}^{k_j}$, which is determined by

$$\boldsymbol{d}^{k_j} = \boldsymbol{V}^{k_j} \boldsymbol{\nabla}\psi^{k_j} \qquad (73)$$

where $\boldsymbol{V}$ is the "metric-correcting transformation", which is an approximation of the inverse of the Hessian matrix, and $\boldsymbol{\nabla}\psi$ is the gradient vector of the Augmented Lagrangian function in Eqn. (70). The components of $\boldsymbol{\nabla}\psi$ are then expressed as

---

[1] Gill, P. E., Murray, W. & Wright, M. H. *Practical optimization.* (Academic Press, 1981).

$$\nabla\psi = \begin{bmatrix} \dfrac{\partial F}{\partial h_j} + \sum_{i=1}^{m}(\sigma g_i - \mu_i)\dfrac{\partial g_i}{\partial h_j} + \sum_{\iota=1}^{4m}(\min\{0, -\sigma g_\iota^E - \lambda_\iota\})\dfrac{\partial g_\iota^I}{\partial h_j} \\[2mm] \dfrac{\partial F}{\partial t_j} + \sum_{i=1}^{m}(\sigma g_i - \mu_i)\dfrac{\partial g_i}{\partial t_j} + \sum_{\iota=1}^{4m}(\min\{0, -\sigma g_\iota^E - \lambda_\iota\})\dfrac{\partial g_\iota^I}{\partial t_j} \\[2mm] \dfrac{\partial F}{\partial l_j} + \sum_{i=1}^{m}(\sigma g_i - \mu_i)\dfrac{\partial g_i}{\partial l_j} + \sum_{\iota=1}^{4m}(\min\{0, -\sigma g_\iota^E - \lambda_\iota\})\dfrac{\partial g_\iota^I}{\partial l_j} \\[2mm] \dfrac{\partial F}{\partial d_j} + \sum_{i=1}^{m}(\sigma g_i - \mu_i)\dfrac{\partial g_i}{\partial d_j} + \sum_{\iota=1}^{4m}(\min\{0, -\sigma g_\iota^E - \lambda_\iota\})\dfrac{\partial g_\iota^I}{\partial d_j} \end{bmatrix} \qquad (j = 1,2,\dots,m) \quad (74)$$

Using the BFGS method, the updating formula for the approximation of the Hessian matrix is of the form

$$V^{k_j+1} = \left[\mathbf{I} - \frac{\Delta X^{k_j}\left(\Delta\delta^{k_j}\right)^{\mathrm{T}}}{\left(\Delta X^{k_j}\right)^{\mathrm{T}}\Delta\delta^{k_j}}\right] V^{k_j}\left[\mathbf{I} - \frac{\Delta X^{k_j}\left(\Delta\delta^{k_j}\right)^{\mathrm{T}}}{\left(\Delta X^{k_j}\right)^{\mathrm{T}}\Delta\delta^{k_j}}\right] + \frac{\Delta X^{k_j}\left(\Delta X^{k_j}\right)^{\mathrm{T}}}{\left(\Delta X^{k_j}\right)^{\mathrm{T}}\Delta\delta^{k_j}} \tag{75}$$

where $\Delta X^{k_j} = X^{k_j+1} - X^{k_j}$ and $\Delta\delta^{k_j} = \nabla\psi^{k_j+1} - \nabla\psi^{k_j}$. To determine the appropriate step size during the search for an improved point, whereby the design objective moves towards a feasible descent direction, we define and minimize the following descent function:

$$\phi^{k_j} = \psi\left(X^{k_j}, \mu^k, \lambda^k, \sigma^k\right) \tag{76}$$

A sequence of trial step size, $s_J$, is defined as

$$s_J = (0.5)^J \qquad J = 0,1,2,3,4,\dots \tag{77}$$

At the $k_j - th$ iteration, we determine an acceptable size as $\beta^{k_j} = s_J$, with $J$ as the smallest integer to satisfy the descent condition

$$\psi\left(X^{k_j} - s_J V^{k_j}\nabla\psi^{k_j}, \mu^k, \lambda^k, \sigma^k\right) \le \phi^{k_j} - s_J\gamma^{k_j} \tag{78}$$

The constant $\gamma^{k_j}$ is determined using the search direction $\gamma^{k_j} = \tau\left\|V^{k_j}\nabla\psi^{k_j}\right\|^2$, where $\tau$ is a specified constant between 0 and 1.

After solving the subproblem Eqn. (71), the design point $X^{k+1}$ is obtained for the $(k+1)$-$th$ step in the iterating process solving the primal problem, while the multipliers are updated through the following rule:

$$\left(\mu^{k+1}\right)_i = \left(\mu^k\right)_i - \sigma g_i(X^k), \qquad i = 1,2,\dots,m \tag{79}$$

$$\left(\lambda^{k+1}\right)_i = \max\left\{0, \left(\lambda^k\right)_\iota + g_\iota^I(X^k)\right\}, \qquad \iota = 1,2,\dots,4m \tag{80}$$

$$\sigma^{k+1} = \begin{cases} \eta\sigma^k, & \text{if } \rho^k \ge \vartheta\rho^{k-1} \\ \sigma^k, & \text{if } \rho^k < \vartheta\rho^{k-1} \end{cases} \tag{81}$$

where

33

$$\rho^k = \left( \sum_{i=1}^{m} g_i^2(\boldsymbol{X}^k) + \sum_{\iota}^{4m} \left[ \min\left\{ -g_\iota^I(\boldsymbol{X}^k), \frac{(\lambda^k)_i}{\sigma} \right\} \right]^2 \right)^{1/2} \tag{82}$$

$\vartheta$ is a specified constant between 0 and 1, and $\eta$ is larger than 1.

The design problem in Eqns. (61) is solved iteratively until the following set of convergence criteria is satisfied:

$$\begin{cases} \left| F^{k+1} - F^k \right| \leq \varepsilon_1 \text{ or } \left\| \boldsymbol{X}^{k+1} - \boldsymbol{X}^k \right\| \leq \varepsilon_2 \\ max\{ |g_1^{k+1}|, \dots, |g_m^{k+1}|, |g_1^{I,k+1}|, \dots, |g_{4m}^{I,k+1}| \} \leq \varepsilon_3 \end{cases} \tag{83}$$

where $\varepsilon_1$, $\varepsilon_2$ and $\varepsilon_3$ are convergence control parameters taking respectively the value of 0.001, 0.001, and 0.01.

## S8. Implementation of morphing on target scheme

This section shows the implementation of the inverse problem scheme explained in S7 to the solution of the last two illustrative demonstrations of morphing on target. While they both share a primary objective, the central axis of the target domain (i.e. an "M"), their boundaries are distinct. The first assumes a uniform, yet unspecified value of the width, which is to find, and the second case features a varying width to match. In both cases, the constituent solids are silicone rubber and wood with CTE and elastic properties reported in section S2.

### S8-A. Demonstration 1: uniform width

As a morphing target, we chose the profile of an "M", and use an arc spline composing smooth, $G^1$ continuous, arcs to prescribe its central axis (Supplementary Fig. S16). Because $x = 7.4$ is a vertical axis of symmetry, only half "M" is here examined. The width of the "M" boundary is uniform along the "M", meaning that $l_1 + 2t_0 = l_2 + 2t_0 = \cdots = l_m + 2t_0$ for all BBs. The central axis of the half domain is here mathematically expressed piece-wisely by the following set of primitives (Supplementary Fig. S16), each bounded by a pair of blending points:

$$f(x,y) = \begin{cases} f_1(x,y) = (y - 1.4)^2 + x^2 - 1.4^2 = 0 & \text{if } 0 \leq x < 1.4 \quad 0 \leq y < 1.6 \\ f_2(x,y) = (y - 2.8)^2 + (x - 14.2)^2 - 12.8^2 = 0 & \text{if } 1.4 \leq x < 3.2 \quad 1.6 \leq y < 9.4 \\ f_3(x,y) = (y - 8.9)^2 + (x - 4.1)^2 - 1.0^2 = 0 & \text{if } 3.2 \leq x < 4.8 \quad 9.4 \leq y < 9.6 \\ f_4(x,y) = (y - 7.7)^2 + (x - 2.9)^2 - 2.7^2 = 0 & \text{if } 4.8 \leq x < 5.6 \quad 8.1 < y \leq 9.6 \\ f_5(x,y) = (y - 8.6)^2 + (x - 8.6)^2 - 3.1^2 = 0 & \text{if } 5.6 \leq x < 6.5 \quad 6.3 < y \leq 8.1 \\ f_6(x,y) = (y - 7.3)^2 + (x - 7.4)^2 - 1.3^2 = 0 & \text{if } 6.5 \leq x \leq 7.4 \quad 6.0 \leq y \leq 6.3 \end{cases} \tag{84}$$

As per Eqn. (53), we look for the optimum values of the design variables $h_i, t_i, l_i, d_i$ ($i = 1,2,\dots,m$). Because the width of the building block, i.e. $\omega_i = l_i + 2t_0$, is prescribed as uniform along the central axis of the target domain and $t_0$ is constant, $l_1 = l_2 = \cdots = l_i = \cdots = l_m$ and the objective function reduces to

the sum of squares of Eqn. (50). For a given number of building blocks (here chosen as 50), the problem formulation (Eqns. (61)) is abridged to

$$
\begin{cases}
\min_{h_i, t_i, l_i, d_i} & F = \sum_{i=1}^{50} \|\boldsymbol{p}'_i - \boldsymbol{r}'_i\|^2 \\
\text{s.t.} & g_i = 0, \\
& 4 \le l_i/h_i \le 10, \\
& 0.01 \le d_i/l_i \le 0.6, \\
& 0.05 \le h_i \le 5, \\
& 0.05 \le t_i \le 5, \\
& 0.05 \le l_i \le 5, \\
& 0.005 \le d_i \le 5, \quad i = 1,2,\dots,50
\end{cases}
\tag{85}
$$
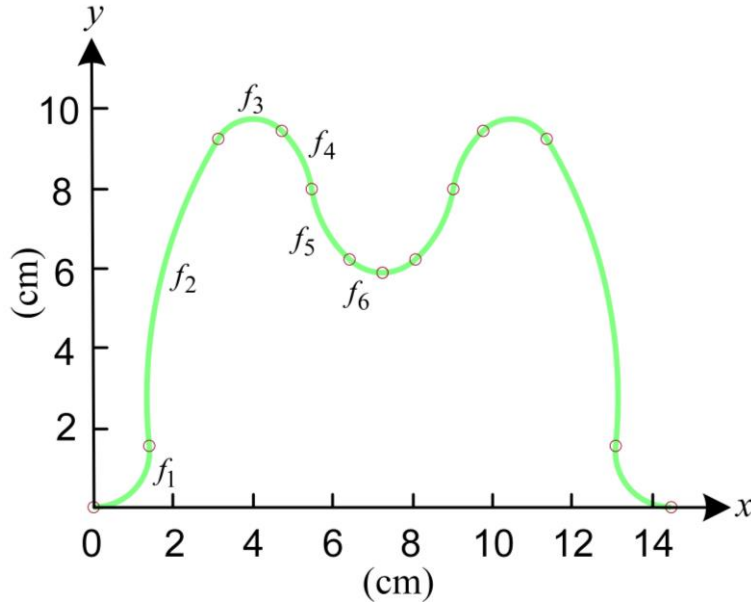


Supplementary Fig. S16: Central axis of the target domain with arc functions and blending points given by Eqn. (84).

Supplementary Fig. S17 shows the outcome of assigning the following initial values to the design variables: $h_i = 0.1, t_i = 0.1, l_i = 0.7, d_i = 0.35, i = 1,2,\dots,50$. The metamaterial phenotype at $T = 120\,°C$ is shown in the lower part with grey and blue representing the low CTE frame and the high CTE core of the BB sequence. On the upper part appears the target curve (green solid line) and the reference points $R_i$ (red).

Due to the randomly assigned values of the design variables, the central axis of the metamaterial phenotype is off from the target. After application of the tailoring scheme, though, the phenotype is realigned to the target after 80 iterations. Supplementary Fig. S18 shows the iteration history for the

35

process to gradually converge to an optimal solution. At convergence, the objective value decreases from the initial 776 to the final $2.81 \times 10^{-6}$, a tiny value indicating the attainment of the gap closure, where the phenotype axis conforms seamlessly to the central axis of the target.
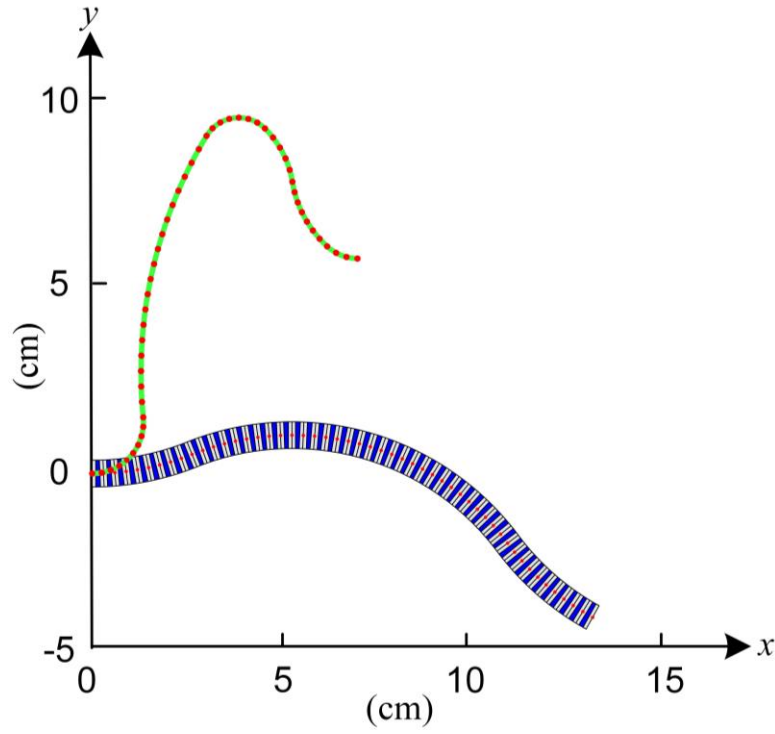


Supplementary Fig. S17: Metamaterial phenotype ($T = 120 \,°C$) with initial guesses for the design variables and reference points on the target curve.
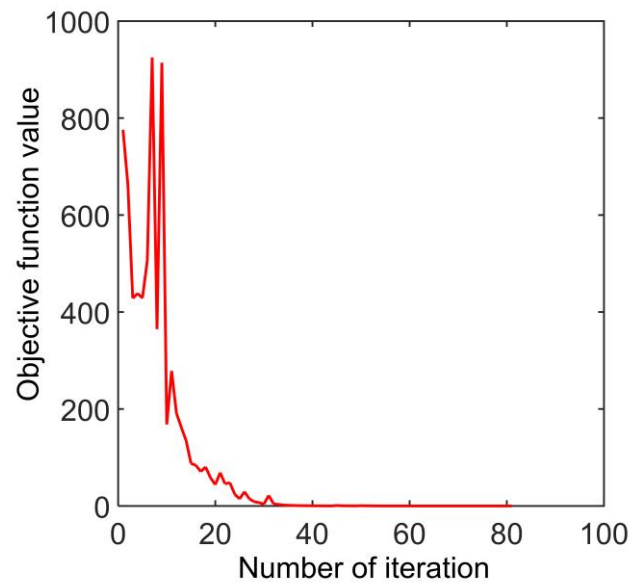


Supplementary Fig. S18: Convergence plot for the objective function.

Supplementary Fig. S19 shows, in a stem plot, the optimized values of the design variables along with their relevant ratios, which define the metamaterial genotype at the initial temperature ($T = 20\ °C$). The values shown in sequence for the 50 BBs are descriptive of each BB geometry as well as their sequence. As described in the caption of Fig.1, each building block is described with $B_{\frac{t}{h}}^{+/-\left(h,\frac{l}{h},\frac{d}{l}\right)}$, where $B = U$ for U-BB and $B = R$ for R-BB, the sign $+/-$ specifies the direction of rotation for R-BB (clockwise: $+$; counter-clockwise: $-$) and is omitted for U-BB. With this notation, we can describe the string of information for a sequence of $m$ BBs as $B_{\frac{t_1}{h_1}}^{+/-\left(h_1,\frac{l_1}{h_1},\frac{d_1}{l_1}\right)} B_{\frac{t_2}{h_2}}^{+/-\left(h_2,\frac{l_2}{h_2},\frac{d_2}{l_2}\right)} \dots B_{\frac{t_m}{h_m}}^{+/-\left(h_m,\frac{l_m}{h_m},\frac{d_m}{l_m}\right)}$, which can be further condense to $\left(B_{\frac{t}{h}}^{+/-\left(h,\frac{l}{h},\frac{d}{l}\right)}\right)_\eta$ for $\eta$ consecutive units with identical BB parameters. This sequence is shown on the bottom of Supplementary Fig. S19 for the "M" problem and constitutes the tailored code that enables the phenotype to morph on target.

Supplementary Fig. S20 shows the resulting configuration at $T = 120\ °C$ along with the phenotype axis and the target axis. The similarity between the phenotype axis and the target axis is evaluated by calculating the coefficient of determination $R^2$, which is mathematically defined as

$$R^2 = 1 - \frac{\sum_{i=1}^{m}\left[\left(x_{pi} - x_{ri}\right)^2 + \left(y_{pi} - y_{ri}\right)^2\right]}{\sum_{i=1}^{m}\left[\left(x_{pi} - \bar{x}_p\right)^2 + \left(y_{pi} - \bar{y}_p\right)^2\right]} \tag{86}$$

where $(x_{pi}, y_{pi})$ and $(x_{ri}, y_{ri})$ represent the coordinates of the BB interface point $i$ of the phenotype on target and the corresponding reference point on the target axis respectively. $\bar{x}_p$ and $\bar{y}_p$ denote the mean value of the relevant coordinates for BB interface points. The coefficient of determination indicates the precision of the fit for both $x$- and $y$-values and ranges from 0 to 1. The better the match between phenotype and target, the closer the value of $R^2$ to 1. In our example, the value of $R^2$ is 0.994, meaning a remarkably good agreement between target and predicted phenotype axis. A minor discrepancy appears (Supplementary Fig. S20) with the reason attributed to the adoption of a surface response for approximating the opening angle of each R-BB (see S3-C-i).
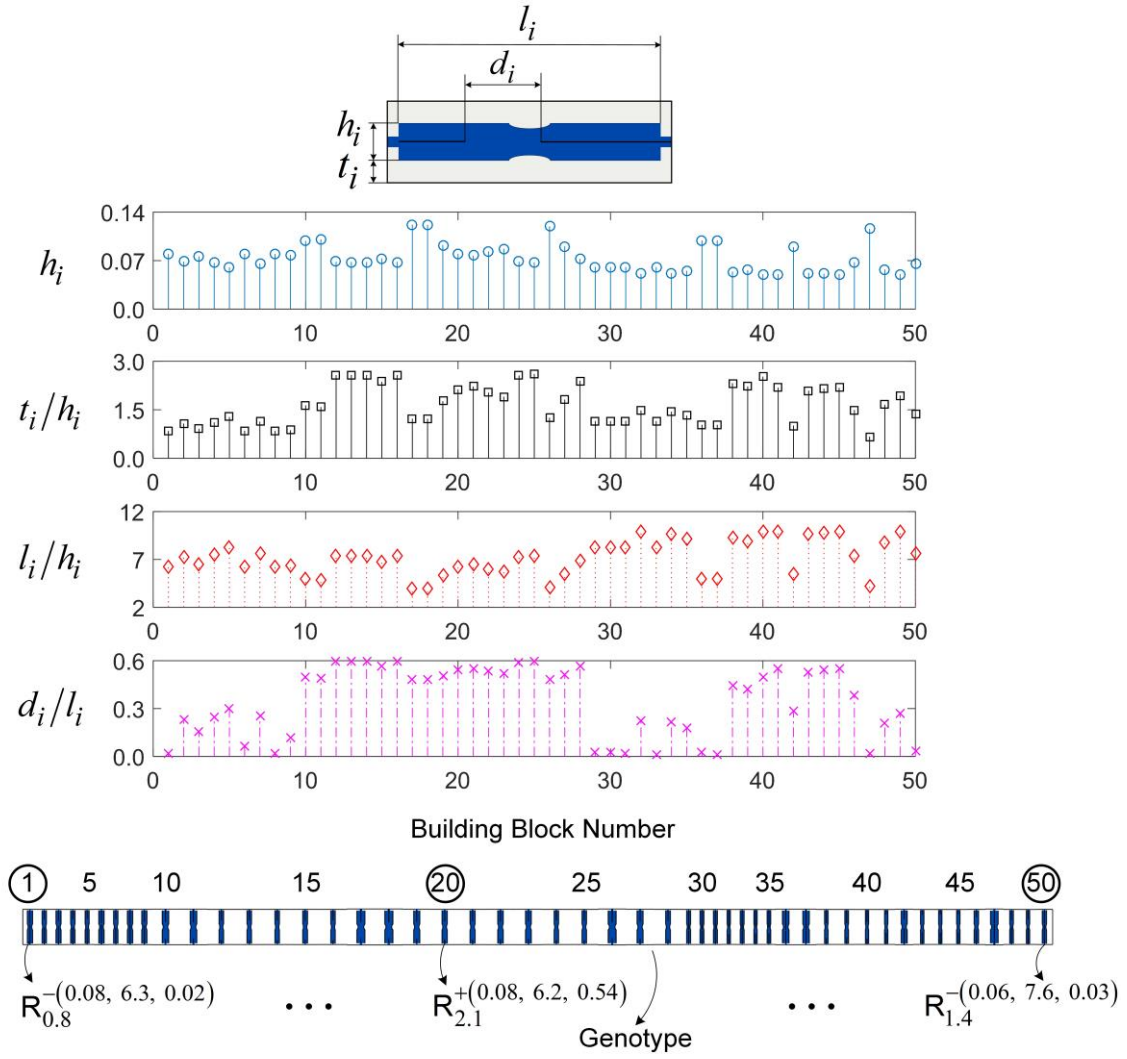
Supplementary Fig. S19: BB geometry with 4 sets of values for the design variables optimized to match the target central axis. The values provide the full geometric description to each of the 50 units making up the metamaterial genotype, which is shown below in its initial undeformed state. Below the genotype is the reported BB sequence code given only for $BB_1$, $BB_{20}$ and $BB_{50}$, chosen as representative BBs.
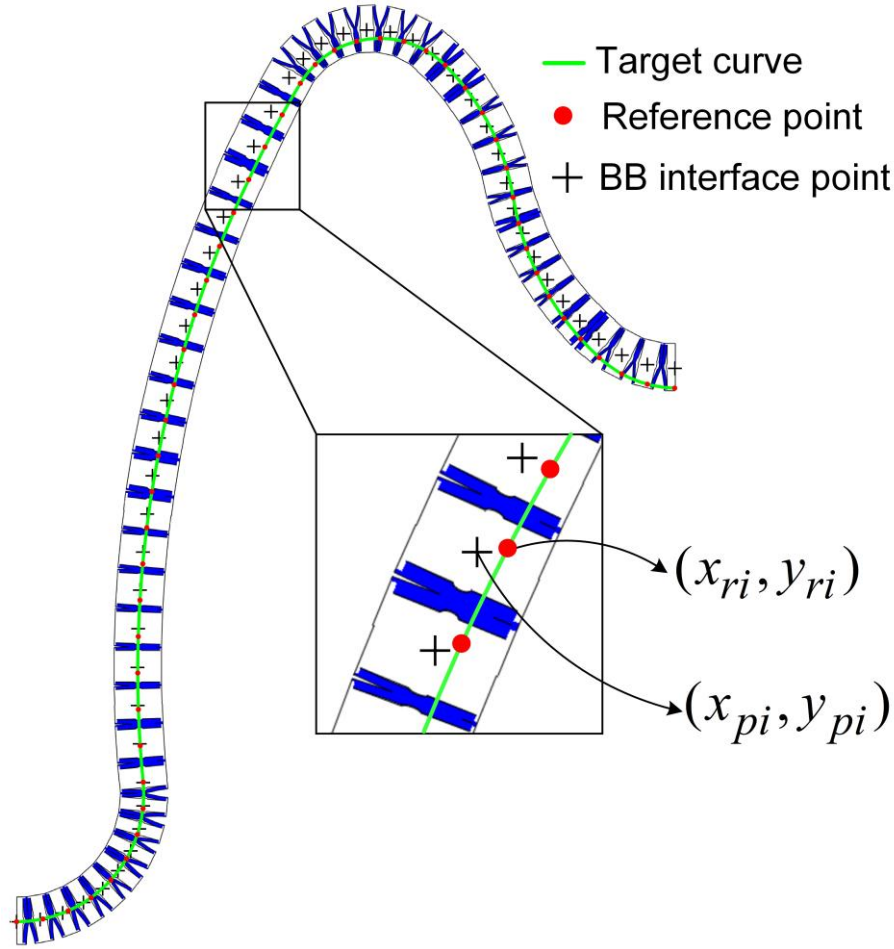
Supplementary Fig. S20: Predicted phenotype at $T = 120\ ℃$ along with BB interface point (black cross), the target axis (green), and reference point (red). The assessment of the match is given by the coefficient of determination, $R^2 = 0.994$ in this case, with unity indicating a perfect match between the two.

**S8-B. Demonstration 2: varying width**

In this example, the central axis of the target domain has the "M" shape of that in Case study 1, hence expressed by Eqn. (84). But the width of the domain boundary is not uniform and specified to vary along the target axis (Fig.5b and Supplementary Fig. S21). Due to symmetry about $x = 7.4$, half of the domain is examined with the target width piece-wisely expressed in the arc-length coordinate system by:

$$w(s) = \begin{cases} w_1(s) = -2.86 \times s + 0.90 & 0.00 \leq s < 0.14 \\ w_2(s) = 1.13 \times s + 0.34 & 0.14 \leq s < 0.67 \\ w_3(s) = -2.78 \times s + 2.96 & 0.67 \leq s < 0.85 \\ w_4(s) = 1.33 \times s - 0.53 & 0.85 \leq s \leq 1.00 \end{cases} \qquad (87)$$

where $s$ denotes the normalized arc length and is defined as:

$$s(x,y) = \int_0^x \sqrt{1 + \left(\frac{\partial f/\partial x}{\partial f/\partial y}\right)^2} \, dx \Bigg/ \int_0^{x_{end}} \sqrt{1 + \left(\frac{\partial f/\partial x}{\partial f/\partial y}\right)^2} \, dx \tag{88}$$

where $f(x,y)$ is the mathematical expression of the central axis of the target, i.e. Eqn. (84), and $x_{end}$ represents the $x$−coordinate of the end point of half domain. Supplementary Fig. S21 shows both the central axis (green) and varying width (shaded areas of dissimilar colors) of the target domain.
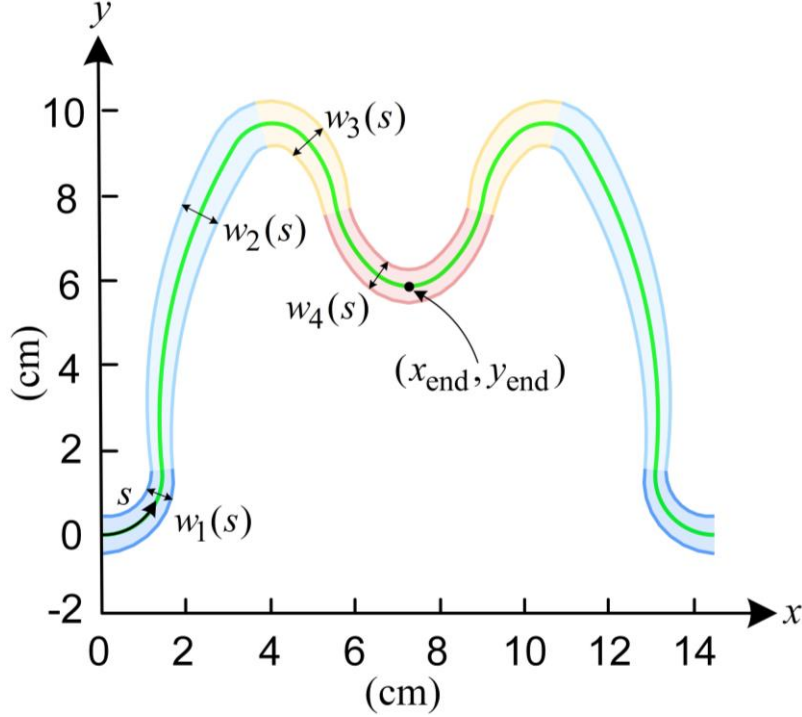


Supplementary Fig. S21: Central axis of the target domain along with its varying widths (4 arc primitives for half domain) defined by Eqn. (87).

As per Eqn. (53), we look for the optimum values of the design variables $h_i, t_i, l_i, d_i$ ($i = 1,2,\ldots,m$). Since both the axis and width functions of the target are specified, the problem is formulated for a given number of building blocks (here chosen to be 46) as:

$$\begin{cases} \min_{h_i,t_i,l_i,d_i} \quad F = \sum_{i=1}^{46} [\|\boldsymbol{p}_i - \boldsymbol{r}_i\|^2 + |\omega_i - w(\boldsymbol{r}_i)|^2] \\ \text{s.t.} \qquad\qquad\qquad g_i = 0, \\ \qquad\qquad\quad 4 \le l_i/h_i \le 10, \\ \qquad\qquad\quad 0.01 \le d_i/l_i \le 0.6, \\ \qquad\qquad\quad 0.05 \le h_i \le 5, \\ \qquad\qquad\quad 0.01 \le t_i \le 5, \\ \qquad\qquad\quad 0.05 \le l_i \le 5, \\ \qquad\qquad\quad 0.005 \le d_i \le 5, \qquad\quad i = 1,2,\ldots,46 \end{cases} \tag{89}$$

The optimization is implemented under the following initial values of the design variables: $h_i = 0.1, t_i = 0.1, l_i = 0.7, d_i = 0.35, i = 1,2, ...,46$. The tailoring process gradually converges to an optimal solution after 128 iterations, and Supplementary Fig. S22 shows the iteration history for the objective function. At convergence, the objective value decreases from the initial 2024 to the final $1.82 \times 10^{-5}$, an extremely small value indicating the achievement of the gap closure, where the phenotype axis and its width conform seamlessly to the axis and boundary of the target.
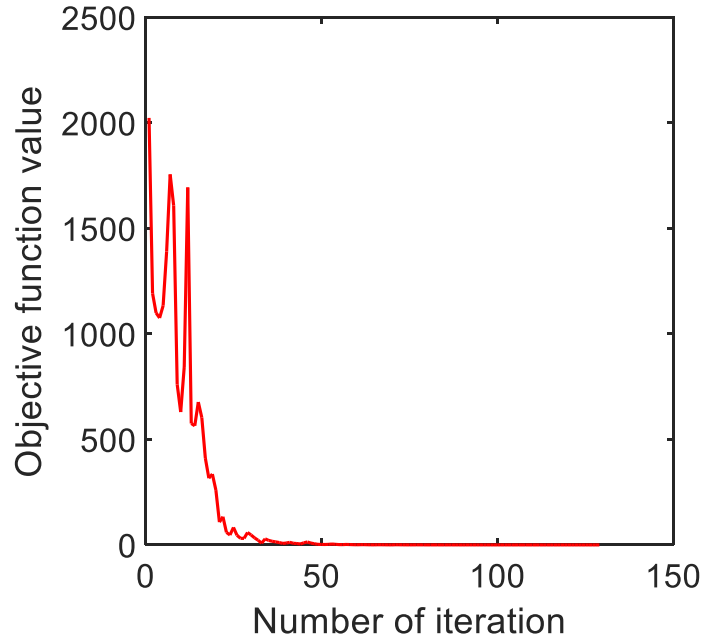


Supplementary Fig. S22: Convergence plot for the objective function.

Fig.5b shows in a stem plot the optimized values of the design variables along with the relevant ratios, which define the metamaterial genotype at the initial temperature ($T = 20$ ℃). The values shown in sequence for the 46 BBs are descriptive of each BB geometry. Their use in the construction of the genotype is shown below along with a representative set of the BB sequence code, used in turn to computationally predict the on-target phenotype shown in Supplementary Fig. S23. Here shown is the resulting configuration at $T = 120$ ℃ along with the phenotype axis and the target axis. The coefficient of determination $R^2$, as defined in Eqn. (86), is used to assess the deviation of the phenotype axis from the target axis with a value of 0.997, indicating a remarkably good match. The reason for the difference between central axis target and predictions can be attributed to the use of a surface response for the opening angle. As for the matching of the varying width of the target domain, i.e. ($\omega_i = l_i + 2t_0$), which is explicit to the design variables, there exists no deviation.
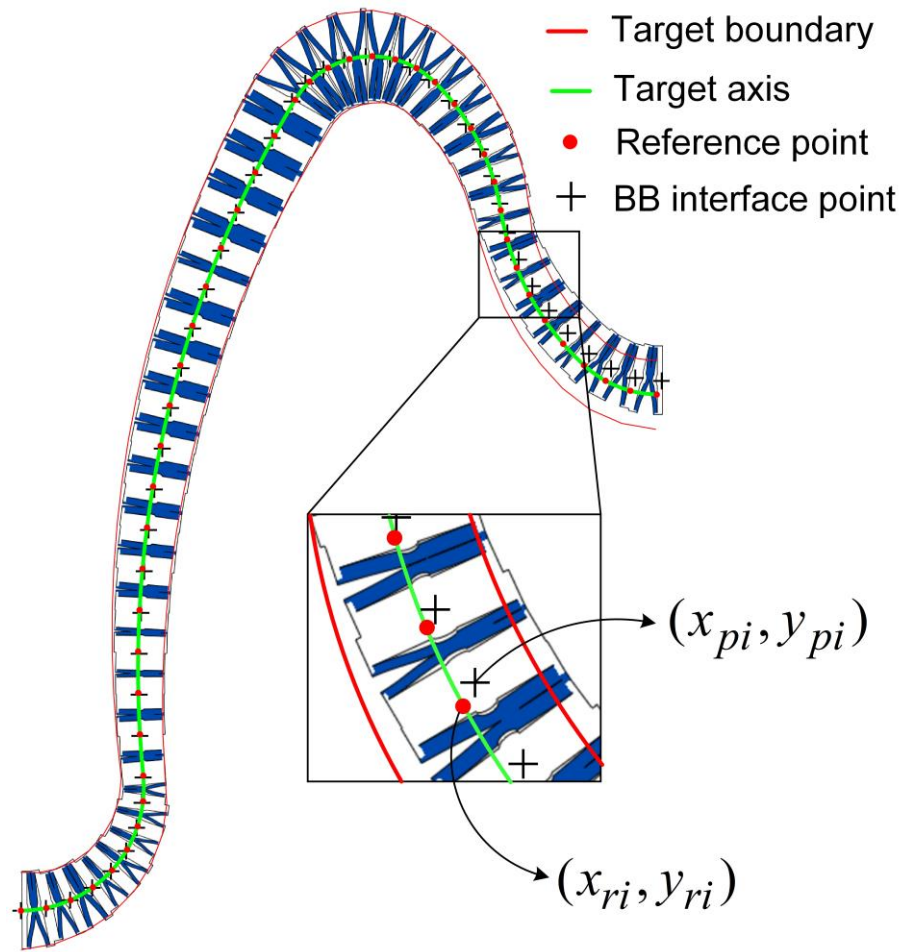
Supplementary Fig. S23: Predicted phenotype at $T = 120\,℃$ along with BB interface point (black cross), the target axis (green) and boundary (red). The precision of the match is $R^2$=0.997, a value approaching unit, the perfect match.